PHANEROZOIC SEDIMENTARY COVER HISTORY OF THE HUDSON PLATFORM: A HEURISTIC MODELING PERSPECTIVE

KALIN T. McDANNELL*,†, PAUL B. O'SULLIVAN**, KERRY GALLAGHER***, and SCOTT BOROUGHS§

*Department of Earth & Planetary Sciences, Dartmouth College, Hanover, NH 03775, United States

**GeoSep Services, 1521 Pine Cone Road, Moscow ID 83843, United States

***Géosciences Rennes, Université de Rennes 1, Rennes 35042, France

\$School of the Environment, Washington State University, Pullman WA 99164, United States

†Corresponding Author: kalin.t.mcdannell@dartmouth.edu

Understanding the long-term erosion and burial history of cratons is challenging due to the incompleteness of the rock record. Here we present a study involving laser ablation apatite fission-track dating of three Canadian Shield basement samples collected adjacent to the Ordovician nonconformity on the Hudson Platform. Compared to a conventional analysis, our samples are characterized by up to $3\times$ the number of dated grains and $> 6\times$ the number of track-length measurements. The large dataset enhances Bayesian QTQt thermal history inversions and helps define conditions for AFTINV modeling within a heuristic Frequentist framework. Modeling is guided by a 'hierarchical testing' philosophy regarding model selection, which allows us to (i) assess the Bayesian model's ability to infer plausible time-temperature paths from the data (i.e., assess sensitivity), (ii) compare the model results with the known geology, and (iii) recursively parameterize models with respect to the previous results. QTQt inversions without time-temperature constraints favor two reheating events, suggesting cooler, near-surface conditions during the late Neoproterozoic-early Paleozoic and Jurassic-early Cretaceous, consistent with major Hudson Platform unconformities. Models indicate that the exposed basement near the Hudson Bay Basin reached peak burial around 317 ± 18 Ma, likely occurring between the Famennian and Carnian stages. A second burial event occurred in the late Mesozoic

to mid-Tertiary between the Aptian and Chattian stages, with peak burial estimated at ca. 46 ± 15 Ma. The easternmost sample, near the Moose River sub-basin, may have reached peak burial conditions at 83 ± 7 Ma (within uncertainty of other models), coinciding with Cretaceous sea level rise. Thermal histories align with preserved basin geology indicating burial during the Ordovician–Devonian and late Cretaceous. However, peak burial may have occurred in the Pennsylvanian and Eocene, implying a more extensive sedimentary cover than is currently preserved in the Hudson Bay Basin. These thermal histories are broadly consistent with burial reconstructions from the Williston Basin and Slave craton to the west. The now-exposed shield was formerly covered by sedimentary rocks estimated to be $\sim 1.24 \pm 0.21$ km thick during the Paleozoic and $\sim 1.37 \pm 0.26$ km thick on average from the latest Mesozoic through the middle Cenozoic.

1 INTRODUCTION

Cratons are the ancient nuclei of continents that have remained tectonically stable since the Archean–Paleoproterozoic. These continental interiors are typically characterized by low topographic relief and Precambrian igneous and meta- morphic crystalline basement exposed at the surface. Many cratonic shields are devoid of sedimentary cover—making reconstruction of their post-orogenic geological history difficult since we often only have 'snapshots' of geological events or processes preserved in the rock record. For example, most of the Canadian interior is comprised of Precambrian basement sporadically covered only by thin early-middle Paleozoic or middle-late Mesozoic sedimentary strata (Sloss, 1963; Norris & Sanford, 1968; Norris, 1977; Telford & Long, 1986; Sanford, 1987; Norris, 1993)—leaving the details about the Phanerozoic geologic history an open question.

Apatite fission-track (AFT) dating has long been one of the primary thermochronological tools used to reconstruct this missing record and constrain the potentially complex burial and erosion patterns across the North American craton (Crowley et al., 1986; Crowley & Kuhlman, 1988; Naeser & Crowley, 1990; Crowley, 1991; Kohn et al., 1995, 2002; Osadetz et al., 2002; Lorencak et al., 2004; Kohn et al., 2005; Feinstein et al., 2009; McDannell et al., 2019b; McDannell & Keller, 2022). Typically, AFT data are

modeled within a supporting framework of geologic constraints for a given study area. More often than not these constraints are a mix of physical geology, geologic interpretations, and assumptions which entail different degrees of uncertainty (McDannell et al., 2022a). The lack of physical constraints to inform modeling is a highly discussed issue and is problematic for exposed basement terranes when trying to reconstruct time-temperature (*t*–*T*) histories (e.g., McDannell & Flowers, 2020; Green et al., 2020; Green & Duddy, 2021; McDannell & Issler, 2021). This issue is usually addressed by drawing on existing geological knowledge, though such data may at times be lacking. Extrapolations are commonly made between a sampling locality and regional geology for the purpose of modeling, but unless samples are taken directly from well-constrained locations (e.g., at or near unconformities), there is no way to determine if such assumptions are valid. The nature of imposed model assumptions may also influence the form of the inferred thermal histories, and in some cases this step may limit impartial assessment of the unknown history in terms of what features are required by the data, and those that the data are consistent with or at least do not contradict.

An outstanding problem relates then to our ability to resolve more complex thermal histories in the absence of firm external constraints. For instance, the Hudson Platform of central Canada (Sanford & Norris, 1973) is a large area of Precambrian basement lacking contiguous Phanerozoic strata—eliciting the question: Was the currently exposed basement buried in the past, and did the amount of burial vary spatially? The reflexive and more interesting assumption would be that the basement *was* buried by sedimentary cover and to simply fix the timing of regional unconformities within inversions—but this can become circular if our model simply confirms our preferred hypothesis without testing other possibilities (e.g., McDannell et al., 2022a). An alternative approach is to first examine the sensitivity and resolving power of the thermochronometric data by minimizing prior assumptions about a thermal history (e.g., Fox & Carter, 2020; Gallagher, 2021; McDannell et al., 2022a,b), and then build-in geologic information or interpretations based on previous modeling results.

We designed an experiment to address the issue of understanding the surface evolution of Precambrian shields devoid of younger sedimentary rocks. We selected three basement samples that come from areas near a nonconformity where the Paleozoic cover sequence is preserved and well characterized. Although the basement is currently exposed, we hypothesize that the nearby stratigraphic cover is an erosional remnant. Therefore, it is likely that our samples experienced burial histories similar to those of the adjacent intracratonic basins. Nevertheless, there is a possibility that our samples were never deeply buried, or that the exposed basement experienced a different history. We also collected elemental data to directly characterize the apatite composition of our samples. Our samples were collected from igneous protoliths, which means that the apatite grains in each sample are likely to have homogeneous kinetic properties, since it is more difficult to interpret and model AFT data from sedimentary rocks with variable provenance or composition (Carter & Gallagher, 2004; Powell et al., 2018; Issler et al., 2022). While uniform kinetic properties may be expected in granitoids, there are documented cases of apatite from plutonic rocks displaying intra-sample compositional variation (O'Sullivan & Parrish, 1995), which can occur from the effects of fluids and (de)hydration reactions during low-grade metamorphism (Smith & Yardley, 1999) or anatexis (Ji et al., 2025). We also measured a substantially greater number of track lengths than the standard benchmark of ~ 100 to test whether more track lengths would yield higher-resolution thermal histories.

1.1 Background: Fission-Track Thermochronology

The fission-track thermochronometer provides time and temperature information from the damage features or tracks produced by the energetic fission of 238 U within a mineral's crystal lattice (Fleischer et al., 1965). The number of spontaneous tracks (N_s) per unit area is related to the amount of U in the apatite and thus can provide an estimate of the time (i.e., apparent age) over which tracks have accumulated in the crystal. Fission tracks form continuously over time with an initial etched length of $\sim 16.5 \,\mu\text{m}$, and fade or anneal when subjected to higher temperature, resulting in a nearly equivalent reduction in track density (per area) across an etched grain surface (Gleadow & Duddy, 1981). Observations of borehole samples showed that with increasing depth, mean track length is reduced (i.e., annealed) with increasing temperature (Gleadow et al., 1986b; fig. 1). As a consequence, annealing decreases the age of the sample as each track is shortened to a degree reflecting the maximum temperature experienced during its history before being totally annealed at

approximately 100–120°C (Gleadow & Duddy, 1981; Green et al., 1986; Gleadow et al., 1986a).

Laboratory experiments have demonstrated that resistance to thermal annealing is influenced by apatite composition (e.g., Green et al., 1985). Approximating track annealing kinetics—a critical component of thermal history modeling—is achieved using the bulk chemical composition of apatite (Laslett et al., 1987; Carlson et al., 1999). The general chemical formula for apatite is A₅(XO₄)₃Z, with the A-site and X-site typically accommodating large divalent cations such as Ca²⁺ and PO₄³⁺, respectively (with P⁵⁺ as the central atom; Piccoli & Candela, 2002). The main elements that control annealing are the substitutions on the monovalent anion (Z) site, such as F⁻, Cl⁻, and OH⁻, followed by various cations that enhance track retentivity compared to common fluorapatite, such as Fe²⁺, Mg²⁺, Mn²⁺, Na⁺, REE³⁺, Si⁴⁺, and Sr²⁺ (Carlson et al., 1999; Barbarand et al., 2003a; Ravenhurst et al., 2003; Tello et al., 2006). Apatite composition is measured directly by electron microprobe or laser ablation inductively coupled plasma mass spectrometry (LA-ICP-MS)—although it is most commonly estimated indirectly by proxy using the *D_{par}* parameter (mean track etch-pit diameter parallel to the c axis; Donelick, 2005).

The temperature range of the AFT partial annealing zone (PAZ; ~120–60°C) varies as a function of annealing kinetics and the rock cooling rate (Gleadow & Duddy, 1981; Green et al., 1986; Gleadow et al., 1986a; Duddy et al., 1988). Fission-track ages can broadly inform us about the overall duration of, and sometimes timing of events in the overall thermal history. The length of a given fission track will reflect to a large degree the maximum temperature that track experienced, whereas a distribution of track lengths provides key information on the structure or complexity of the thermal history (e.g., Gleadow et al., 1986a,b). Thus models of how fission tracks anneal are essential for the accurate modeling and interpretation of track length data (Ketcham et al., 1999, 2007) and provide additional information about thermal history style that is unavailable to most other thermochronometers. Figure 1A conceptually demonstrates this for four different simplified thermal histories using a forward model, including: (i) rapid cooling followed by isothermal conditions at the Earth's surface; (ii) linear, slow cooling at a typical cratonic rate of ~0.2°C/My; (iii) slow cooling to the surface, followed by reheating to 65°C and cooling out of the PAZ; and (iv) same style as history-3 except reheating to 85°C within the

PAZ. Each of these histories produce characteristic ages and track length distributions that are diagnostic of the type of history the AFT sample experienced (fig. 1B–E). The histories in fig. 1A yield either, a unimodal (normal) distribution of long track lengths of $\sim 15 \,\mu m$ for the rapid cooling scenario (fig. 1B); a unimodal negative skew distribution for slow cooling with a mean length of $\sim 14 \,\mu m$ (fig. 1C); a unimodal broad or flattened distribution with a similar mean length as the slow cooling case (fig. 1D); and a bimodal distribution for the 85°C reheating example (fig. 1E). The predicted AFT model age for each respective path is *ca.* 570 Ma, 290 Ma, 440 Ma, and 365 Ma, and the progression from fig. 1B–E generally shows that track length distributions become broader and shorter with increased magnitude and duration of heating. From these simple demonstrations, we can see that track lengths are critical for understanding a rock's thermal history.

2 CASE STUDY: HUDSON PLATFORM, CANADIAN SHIELD

2.1 Brief Geologic Overview

The Canadian Shield is traditionally regarded as a region of prolonged tectonic and geomorphic stability, with much of its exposed Precambrian basement presumed to have remained subaerially exposed and largely unburdened by thick sedimentary cover throughout the Phanerozoic. This canonical view, however, may oversimplify the surface history since the shield may have been altogether denuded only recently during the Laurentide glaciation (e.g., Bell & Laine, 1985). Other indirect evidence suggests that craton surface evolution was much more dynamic. Many studies infer periodic burial during high sea-level excursions (e.g., Bond, 1978; White et al., 2000) and erosion during epeirogenic mantle perturbations (e.g., Ahern & Mrkvicka, 1984; Crowley & Kuhlman, 1988; Burgess et al., 1997; Flowers et al., 2012). Tectonic processes such as plate reorganization and peripheral orogenesis (e.g., Sanford et al., 1985; Crowley, 1991; Kohn et al., 2005; Ault et al., 2009; Feinstein et al., 2009) may have contributed to both cratonic burial and erosion at different times. To better understand continental interior surface evolution, three crystalline basement samples were collected from central Canada that have reliable, albeit limited geologic information to support thermal history modeling (described below).

Non-peer reviewed preprint submitted to EarthArXiv. Under review with American Journal of Science.

The Hearne Domain is part of the Churchill Province (fig. 2) and is comprised of Neoarchean granitoids, greenstones, metasedimentary and volcanic rocks, and Paleoproterozoic granites that flank reworked late Paleoproterozoic basement to the south (fig. 2; Hoffman, 1988, 1989; Weller & St-Onge, 2017), and the Paleozoic–Mesozoic Hudson Bay sedimentary basin to the east (Pinet et al., 2013). The Superior Province is the nucleus of the Canadian Shield and contains an assemblage of some of the oldest rocks on Earth, including Archean oceanic and continental terranes that collided and underwent Neoarchean metamorphism and cratonization by *ca.* 2700–2600 Ma (Percival et al., 2012). The central Canadian Shield is generally considered to have been tectonically stable since intracratonic basin formation *ca.* 1700 Ma (Fraser et al., 1970; Rainbird et al., 2007) following the Tran-Hudson Orogeny (THO; e.g., Schneider et al., 2007) and the assembly of Laurentia at *ca.* 1800 Ma (Hoffman, 1988, 1989).

Sample locations are considered within the context of regional Phanerozoic geology. The Hearne Domain sample (97-10-365) is from exposed granodiorite basement within the Seal River Fold Belt (Anderson et al., 2010; Rayner, 2010). This location is at the erosional edge of the Hudson Bay Paleozoic nonconformity at the mouth of the Seal River in northeastern Manitoba (fig. 2). The THO sample (CB99-227) was collected from a foliated biotite tonalite from Stephens Lake, ~28 km from the Paleozoic unconformity in Manitoba. Sample 12RM086 was collected from a porphyritic K-feldspar quartz monzonite in the western Superior Province "Ring of Fire" region in northern Ontario (fig. 2), ~50 km west of the present-day erosional edge of the Paleozoic unconformity in the area of McFaulds Lake (Metsaranta & Houlé, 2017). Preliminary fission-track data for this sample were first reported in McDannell et al. (2022c).

The Hudson Bay Basin is a large intracratonic basin that has preserved strata over 2500 m thick (fig. 2 and fig. 3), primarily consisting of Upper Ordovician to Upper Devonian shallow marine rocks overlain by inferred Cretaceous rocks (Norris & Sanford, 1968; Pinet et al., 2013; Lavoie et al., 2015). The Ordovician rocks in the Hudson Bay region are

Edenian to Richmondian in age (*ca.* 454–444 Ma; Nelson, 1963; Armstrong et al., 2018; Zhang & Riva, 2018), but are as old as *ca.* 475 Ma in the northerly Foxe Basin (Trettin, 1975). The onshore basal Paleozoic section of the Hudson Bay Basin is the middle Upper Ordovician Portage Chute Formation of the Bad Cache Rapids Group (Lavoie et al., 2019, for summary), which is *ca.* 453–447.5 Ma in age (Maysvillian Stage) or *ca.* 470–450 Ma in age, depending on the location and applied age model (Peters et al., 2018; Gradstein et al., 2020). Refer to McDannell & Keller (2022) and McDannell et al. (2022c) for further discussion.

Much of the later Phanerozoic sedimentary record is fragmented or completely absent. Tillement et al. (1976) first described the presence of marine Pennsylvanian rocks from pollen assemblage analysis of samples from the Narwhal O-58 well in Hudson Bay. Those findings were disputed as additional biostratigraphic work found mixed Westphalian (ca. 315–306 Ma or ICS stages Bashkirian-Kasimovian), Cretaceous, and Tertiary microfossils (Williams & Barrs, 1976). The earlier results and interpretations of Tillement et al. (1976) were instead attributed to "drilling contamination" by Williams & Barrs (1976), but those authors' conclusions remain controversial. The adjacent Moose River Basin (fig. 2) contains Upper Ordovician through Upper Devonian strata with a major unconformity overlain by minor Middle Jurassic (Bajocian-Bathonian, 170-165 Ma; Norris, 1977) and unconformable Early Cretaceous rocks (Albian-Aptian; ca. 121–100 Ma; Norris & Sanford, 1968; Norris, 1977; Telford & Long, 1986). The ca. 180-170 Ma hypabyssal facies kimberlites in the Attawapiskat area of the Moose River Basin (fig. 2) erupted subaerially through basement and thin Paleozoic cover (Kong et al., 1999; Sage, 2000; Webb et al., 2004). The INCO-Winisk #49204 borehole (fig. 2) penetrates Ordovician strata and also contains palynological evidence of possible Albian-to-Turonian (ca. 113–90 Ma) recycling and younger sediments of Miocene age unconformably overlying the Paleozoic section (Galloway et al., 2012). The regional applicability of this constraint is uncertain but there are isolated occurrences of thin Tertiary strata along the southern Hudson Bay Basin in northern Ontario and Manitoba (Lavoie et al., 2013).

The Williston Basin lies to the southwest of our samples (fig. 2) and contains thick basin fill of > 4 km deposited during the Phanerozoic (Burrus et al., 1996), beginning with the platform onlap of the Sauk sequence (Sloss, 1963; Norris & Sanford, 1968; Sanford,

1987). The basin was undergoing rapid subsidence during the Cambrian after *ca.* 488 Ma during deposition of the Deadwood Formation and the Middle Ordovician Winnipeg Formation (ca. 471–458 Ma depositional age; LeFever, 1996). A major angular unconformity exists in the basin between Mississippian and Triassic strata (*ca.* 325–220 Ma; Butcher et al., 2012) implying erosion and possible near-surface conditions for Precambrian basement across the shield during that interval.

Regionally, an episode of Paleozoic heating ranging between ~70–100 °C has been documented for Precambrian basement located to the southwest and east of the Hudson Bay Basin—attributed to epeirogenic basin formation from the decay of a lithospheric thermal anomaly (Crowley et al., 1985; Crowley & Kuhlman, 1988) or the distal effects of burial from Appalachian orogenesis, respectively (Lorencak et al., 2004; Kohn et al., 2005; Feinstein et al., 2009). This contrasts with thermal history modeling results for AFT samples from the Musselwhite gold mine in northern Ontario (fig. 2) that indicate Paleozoic-Mesozoic heating was limited (Pinet & McDannell, 2020). These spatial differences may be due to the subtle effects of paleo-arch systems across the southern shield (Sanford et al., 1985; Sanford, 1987; Sanford & Grant, 1990). These basement-controlled, physiographic elements, such as the well-known Transcontinental arch (fig. 3), were positive topographic features that conceivably influenced regional sediment dispersal and depositional patterns during the latest Precambrian (?) through the mid-Paleozoic (Sanford et al., 1985; Sanford & Grant, 1990). The distribution of older AFT ages and longer track lengths near the Severn arch (oriented NW–SE near the Musselwhite mine; figs. 2 and 3) and Transcontinental arch (Kohn et al., 2005) indicate minimal burial and support the interpretation that these areas were early Phanerozoic topographic highs.

To summarize, regional information suggests that Precambrian basement was exhumed prior to or by *ca.* 460 Ma. Of critical importance is the fact that basement may have been subaerial for 50–100 My (or more) prior to the Ordovician (e.g., McDannell & Keller, 2022). Burial of the shield occurred primarily during the Ordovician through Devonian (Patchett et al., 2004), and possibly into the Carboniferous (Tillement et al., 1976). Basement was exhumed during the late Carboniferous through the Jurassic, followed by deposition during the Cretaceous through early Tertiary, with final exhumation beginning by the early Tertiary or after approximately Oligocene-Miocene time. We present new AFT

analytical results, which are modeled to assess whether our data can yield thermal histories that are independently consistent with the accepted regional geological evolution. There is also the question of whether the currently exposed Hudson Platform basement was buried during deposition of the Hudson Bay sequence. Burial of basement in the early Paleozoic is plausible for our samples due to their proximity to the Ordovician nonconformity.

3 METHODS AND RESULTS

3.1 LA-ICP-MS Fission Track Dating

Apatite grains were double-dated by LA-ICP-MS using a Agilent 7700 inductively coupled plasma mass spectrometer at Washington State University (WSU) and the modified ζ -calibration method for fission track dating (Chew & Donelick, 2012; Cogné et al., 2020). Laser-ablation AFT (LAFT) data errors in this paper are reported as 1s unless noted otherwise and the analytical methods that are briefly described below are the same as those discussed in McDannell et al. (2019a) and McDannell et al. (2022c). One procedural difference for the data discussed herein is that the AFT samples were analyzed in two separate aliquots (dated 'blind') with a focus on collecting more track length data. For the second aliquot, lengths were only measured from grains where tracks were counted to test for possible compositional variability (e.g., Issler et al., 2022) and to facilitate direct linking of measured lengths with grain ages.

Rocks were crushed and underwent standard heavy mineral disaggregation using magnetic and heavy liquid density separation techniques. Apatite grains were mounted in epoxy, polished, and etched in 5.5 M HNO₃ for 20 s at 21°C to reveal all natural fission tracks intersecting the polished grain surface. For each age grain, grain locations were recorded, and spontaneous track densities were counted using an optical microscope with unpolarized light at 2000× magnification. Horizontal confined track lengths (precision \pm 0.20 μ m) and their angles relative to the crystallographic c-axis (precision \pm 2°) were also measured using a digitizing tablet interfaced with a computer. Single laser-ablation spots (16 μ m-diameter spot) were chosen within grain counting areas to mitigate potential

discrepancies in U measurement, for example, a mismatch between the counted area U and ablation spot U. The high track densities for our samples make U zoning on the etched grain surface detectable, and none of our samples showed evidence for strong zonation. A cylindrical laser pit was excavated to a depth of approximately $16 \mu m$, exceeding the $\sim 8 \mu m$ depth at which uranium contributes fission tracks to the etched grain surface. The depths of a representative number of pits were measured, and the 238 U/ 43 Ca ratio was calculated as the weighted mean of individual scan ratios, weighted by the depth from which the ablated material originated. Uranium concentrations were thus down-pit weighted to approximately $8 \mu m$ (half the length of a fresh track). Uranium (238 U) concentrations were determined for the track-count areas on each age grain by LA-ICP-MS, based on the weighted mean 238 U/ 43 Ca ratio from spot analysis during laser pit excavation. The 43 Ca signal was used to estimate the ablated volume, assuming stoichiometric Ca in apatite.

Fission-track ages and associated errors were calculated using the ratio of the density of natural fission tracks in the grain to the amount of 238 U present, and the modified age equation incorporating a session LA-ICP-MS ζ -calibration factor. Equations (1) and (2) for LAFT age and error calculations from Donelick (2005), respectively, are shown. The fission-track age of an individual grain, t_i , is calculated using the equation:

$$t_i = \frac{1}{\lambda_d} \ln \ln \left(1 + \lambda_d \zeta_{MS} g \frac{\rho_{s,i}}{P_i} \right) \tag{1}$$

where: λ_d is the decay constant for spontaneous fission of $^{238}\text{U} = 1.55125 \times 10^{-10} \text{ yr}^{-1}$, ζ_{MS} is the modified zeta calibration factor specific to the LA-ICP-MS method (here, $\zeta = 8.2727 \pm 0.1407$), g is a geometry factor equal to 1, accounting for etching and track registration efficiency, $\rho_{s,i}$ is the spontaneous track density measured in grain i, P_i is the $^{238}\text{U}/^{43}\text{Ca}$ ratio for apatite grain i. The symmetric uncertainty in the fission-track age, σ_i , is given by:

$$\sigma_i = \left[\left(\frac{1}{N_{S,i}} + \left(\frac{\sigma_{P_i}}{P_i} \right)^2 + \left(\frac{\sigma_{\zeta_{MS}}}{\zeta_{MS}} \right)^2 \right) \right]^{1/2} \tag{2}$$

where: $N_{s,i}$ is the number of spontaneous tracks counted in grain i, σ_{Pi} is the error of P_i , σ_{CMS} is the uncertainty in the zeta calibration factor, ζ_{MS} . Each term in the uncertainty equation contributes to the total variance in the age estimate, and the square root of their sum yields the standard uncertainty. The ζ -calibration factor was determined for each analytical session by measuring the U:Ca of the Durango apatite standard at the beginning and end of each LA-ICP-MS run. The Durango and McClure Mountain (MMhb) age standards were utilized for LAFT and U-Pb data acquisition, respectively. The AFT pooled age obtained in analytical sessions for Durango was 31.4 ± 0.8 Ma (1 SE), which is in agreement with the $^{40}\text{Ar}/^{39}\text{Ar}$ reference age of 31.44 \pm 0.18 Ma (McDowell et al., 2005). The McClure Mountain AFT pooled age was 256 ± 7 Ma (1 SE) and the weighted mean U-Pb age was 525 ± 13 Ma. All ages are in agreement with published values (see Chew & Donelick, 2012). We do not discuss the U-Pb data in this paper but the analyses are included for completeness. The U-Pb results generally support published geochronology that constrain the regional Archean-Paleoproterozoic high-temperature polymetamorphic history (Kellett et al., 2020). All analytical results are provided in tables within the Supplementary Information.

3.2 Electron Probe Microanalysis

Electron probe microanalysis (EPMA) was carried out using a JEOL JXA8500F field emission electron microprobe with an electron beam size of 5 μm operated at 15 kV (current 20 nA) to collect a single spot measurement (per grain) on the AFT mounts at the WSU GeoAnalytical Laboratory. The analyzed elements included: Ca, P, F, Cl, Na, Mg, Mn, Fe, Sr, Y, La, Ce, S, and OH estimated by difference using the same methods discussed in McDannell et al. (2019a). The second LAFT aliquots included Si and had two EPMA spots analyzed, one near the laser-ablation pit, and the other located in a different area of the grain to assess potential compositional heterogeneity (fig. 4). Figure 4 shows examples of the EPMA analyses for a few of the grains analyzed in the second aliquots. The aliquot-2 grains with two probe spots indicated compositional variation, suggesting intragrain elemental zoning is present in all the samples. Complete EPMA data are provided in the *Supplementary Information*.

The apatite stoichiometric calculations for EPMA data from Ketcham (2015) were used to calculate weight percent oxide totals (and atoms per formula unit; apfu) including OH and F-Cl oxygen-equivalent corrections. Elemental weight percent oxide totals are 98.9 \pm 1.9% for 350 analyses (including OH estimation) and suggest near endmember fluorapatite or mixed F-Cl-OH apatite with secondary trace element and REE in all three samples. The few grains with low totals < 97% are flagged in the supplemental dataset and should be used with caution for any petrogenetic interpretation (refer to discussion in Issler et al., 2022). Estimated grain average weight % oxide elements include (aliquot-2 data only): Ca = \sim 54.7%, P = \sim 41%, F = \sim 3.0%, OH = \sim 0.55%, Si = \sim 0.14%, Y = \sim 0.1%, S = \sim 0.09%, Mn = \sim 0.06%, Sr = \sim 0.05%, Na = \sim 0.05%, Ce = \sim 0.04%, Cl = \sim 0.02%, and Fe = \sim 0.02%.

The elemental data were plugged into the multivariate equation of Carlson et al. (1999) to calculate a single kinetic parameter, r_{mr0} , to approximate the annealing kinetics of the AFT data for inverse modeling. The nonlinear r_{mr0} values using the 1999 equation were also converted to linear 'effective Cl' (eCl) values (McDannell & Issler, 2021 and Issler et al., 2022 for discussion). Effective Cl of 0.0 apfu is indicative of endmember fluorapatite, whereas negative eCl values imply lower track retentivity compared to common fluorapatite and is calculated by an extrapolation of the r_{mr0} –Cl relation for r_{mr0} values > 0.84. The rearranged Ketcham et al. (1999) [from their fig. 7a] equation for calculating eCl is:

$$eCl = (ln(1 - r_{mr0}) + 1.834)/2.107$$
 (3)

3.3 Fission Track Ages, Lengths, and Elemental Chemistry

The fission-track grain ages for the three samples in this study are reported in the *Supplementary Information* and summarized in Table 1. The central ages presented in the data tables are calculated from the single-grain LAFT ages and their 1s uncertainties. Sample 97-10-365 has an AFT central age of 512 ± 20 Ma (n = 63/65, age dispersion = 26%, $P(\chi^2) = 0.0$) with grain ages spanning 300 ± 39 Ma to 926 ± 328 Ma and a conventional mean track length (MTL) of 12.01 ± 1.75 μ m and c-axis projected MTL of 13.64 ± 1.02 μ m (n = 709). The N_s counts for this sample totaled 14,511. The median r_{mr0} is 0.843 and the average eCl is -0.007 ± 0.019 apfu across all probed grains. The absolute difference

between the EPMA spot measurements for 37 grains in aliquot-2 ranged from \sim 0.0 to 0.06 apfu, with a median value of \sim 0.02 apfu—this is in general agreement with a large suite of analyses from Issler et al. (2022) that show most replicate grain eCl measurements are within \pm 0.03 apfu.

The sum of N_s counts was 12,444 for sample CB99-227 with a central age of 486 ± 23 Ma (n = 50, age dispersion = 30%, $P(\chi^2) = 0.0$) and grain ages spanning 208 ± 16 Ma to 965 ± 64 Ma. CB99-227 has a measured MTL of 11.81 ± 1.67 μ m and c-axis projected MTL of 13.54 ± 0.93 μ m (n = 656). The median r_{mr0} is 0.839 and the average eCl is 0.001 ± 0.018 apfu across all probed grains. The absolute difference between the EPMA spot measurements for 32 grains in aliquot-2 ranged from ~ 0.0 to 0.08 apfu, with a median value of ~ 0.015 apfu. Aliquot comparisons for this sample show differences in random grain sampling during analysis. Aliquot-1 contains a dominant proportion of older grains whereas aliquot-2 has a larger proportion of younger, high-U grains (implying there is a greater possibility of sampling bias in studies that report ≤ 20 grain ages).

The Superior Province sample 12RM086 is also a combined dataset, including aliquot-1 that was previously summarized and modeled (McDannell et al., 2022c; the analytical data are presented in this paper), along with new data for aliquot-2 provided in the Supplementary Information. We discuss those initial results and interpretations here. Sample 12RM086 was characterized by a central AFT age of 484 ± 24 Ma and age dispersion of 22% (n = 25). One hundred thirty track lengths were measured with a conventional (unprojected) MTL of $12.67 \pm 1.72 \mu m$. McDannell et al. (2022c) interpreted the first sample aliquot as multikinetic—tentatively exhibiting two kinetic groups with limited compositional overlap between populations using the eCl (r_{mr0}) kinetic parameter (complete population overlap using D_{par} and measured Cl only). Multikinetic interpretation of sample 12RM086 followed the methodology discussed in Issler et al. (2022) by examining age-kinetic relationships and a radial plot (Galbraith, 1990) as a guide for identifying mixture model components linked to grain chemistry. Two age components of 367 ± 17 Ma and 569 ± 16 Ma were defined during mixture modeling. After sorting grains by eCl, the central AFT ages for each kinetic population were determined to be 363 ± 14 Ma and 568 ± 21 Ma, in agreement with those recognized from mixture modeling.

A second aliquot of 12RM086 was dated separately and had many more AFT

measurements collected (i.e., sum $N_s = 6699$ and 733 track lengths). This aliquot was also analyzed by EPMA twice on each grain to assess potential elemental variation. The eCl values for both aliquots ranged between -0.063 to 0.024 apfu ($r_{mr0} = 0.859$ to 0.832; n = 125) and the absolute difference between the EPMA spot measurements for all 40 grains in aliquot-2 ranged from ~0.0 to 0.07 apfu, with a median value of ~0.02 apfu. The second aliquot has a central AFT age of 408 ± 13 Ma and a conventional MTL of 12.35 ± 1.81 μ m (n = 733)—in agreement with the results from aliquot-1, with only a minor shift in age and MTL due to greater sampling. The two aliquots were combined (total $N_s = 10,142$) with 65 grain ages spanning 292 ± 27 Ma to 758 ± 64 Ma. Combined sample 12RM086 has a central age of 433 ± 14 Ma (n = 65, age dispersion = 21%, $P(\chi^2) = 0.0$) and a measured MTL of 12.40 ± 1.80 μ m and c-axis projected MTL of 13.86 ± 1.10 μ m (n = 863).

3.4 Thermal History Modeling: QTQt and AFTINV Software

Modeling in this paper was performed using the Bayesian QTQt software (Gallagher, 2012) and the AFTINV software (Issler, 1996; Willett, 1997; Issler et al., 2022) to illustrate what thermal history features can be resolved (or not) by implementing a heuristic modeling approach. We discuss our thermal history modeling strategy using the two different inversion programs. Inverse modeling was carried out within a Bayesian modeling framework using the QTQt v. 5.8.0 software (Gallagher, 2012). We first minimized the use of constraints as time-temperature "boxes" that force the model to take a predefined path in a certain part of the history, allowing us to instead examine the ability of the model to independently infer geologically plausible t-T paths from the thermochronological data (and Bayesian general prior assumptions). To be clear, the 'unconstrained' models establish the baseline t-T sensitivity of the data and are not necessarily interpreted as the preferred thermal history. We then examined the unconstrained models and determining regions of t-T space that were well resolved and those parts that did or did not agree with the known geology. That information was then explicitly applied as a constraint, or multiple constraints, in another set of inversions to refine the thermal history. The QTQt models were also compared to results generated using AFTINV. The AFTINV models are informed by the QTQt results, yet are constructed with the more prevalent 'hypothesis test'

modeling philosophy in mind (i.e., continuous cooling vs. one peak vs. two-peak history), which is inherent to software that implements a Frequentist statistical framework (e.g., HeFTy; Ketcham, 2005). AFTINV (and similar software) explicitly requires more boundary conditions and user-specified constraints to fit the observed data and achieve model convergence. The methods and results discussed here offer a progressive approach that explores some of the ways inverse modeling can not only inform but assist in deciphering the complex surface history of cratons.

QTQt implements a reversible jump Markov Chain Monte Carlo (MCMC) algorithm that performs an adaptive exploration of the model space, incorporating prior information that defines the range and variability of parameters within the general prior (i.e., the model time-temperature domain). These priors include constraints such as maximum heating/cooling rates, kinetic [annealing] model uncertainty, and geologically informed features like the timing of unconformities. Parameters are randomly sampled and perturbed as individual forward models are iteratively constructed, yielding an ensemble of accepted *t*–*T* solutions that reproduce the observed data. Model acceptance within the MCMC framework is governed by the combined prior-likelihood-proposal ratio. Importantly, simpler thermal histories with fewer t-T points are generally favored over more complex ones when the fit to the data is comparable—thus allowing the data to play a central role in determining model complexity (rather than complexity being defined a priori; Gallagher, 2012; Vermeesch & Tian, 2014; Gallagher & Ketcham, 2018). The reversible-jump component of the MCMC algorithm statistically accounts for the trade-off between model complexity and fit quality. Consequently, if a simple history adequately reproduces the data, it will be preferred unless additional information justifies a more complex model. This approach is particularly useful for evaluating the resolving power of low-temperature thermochronometric datasets, both with and without user-defined constraints (McDannell & Issler, 2021). It is important to reiterate that modeling without consideration of indisputable geological constraints is not best practice. All model outputs are conditional upon the inputs provided, and therefore, predictions must be critically assessed in the context of thermochronological observations and geological plausibility (Gallagher, 2016).

We also carried out modeling in the AFTINV v. 6.17 software (Issler, 1996; Issler et al., 2022) that employs a model acceptance threshold based on Frequentist *p*-value statistics, similar to the commonly used HeFTy program (Ketcham, 2005). The primary difference between the QTQt and AFTINV, is that the latter model ensures all accepted paths meet or exceed a certain goodness-of-fit (GOF) level based on formal statistical hypothesis tests (see Ketcham, 2005; Vermeesch & Tian, 2014; Ketcham, 2019). AFTINV uses either a nondirected Monte Carlo (MC) scheme or a Controlled Random Search algorithm (CRS; Price, 1977; Willett, 1997), or both in combination (Issler et al., 2022; McDannell et al., 2022c), to search parameter space for plausible thermal histories—usually 300 solutions at the 0.05 and/or 0.5 significance levels (analogous to the respective green and magenta paths in HeFTy). The AFTINV software allows various history styles to be combined to create complex thermal history scenarios with multiple phases of heating and cooling using randomly selected heating and cooling rates with temperatures calculated at fixed, user-specified time nodes. Refer to McDannell et al. (2019b), McDannell & Issler (2021), and Issler et al. (2022) for other recent discussions of modeling using AFTINV.

4 DISCUSSION

4.1 LA-ICP-MS AFT Data Evaluation

We present a large quantity of AFT analytical data that is far beyond what is reported in most studies (refer to supplementary tables). The N_s counts alone for our three samples totaled over 37,000 tracks and the number of measured track lengths was 2,228. With respect to a conventional AFT sample analysis, each of our examples represents up to $\sim 10 \times 10^{-10}$ the number of typical N_s counts and more than $6-8 \times 10^{-10}$ the number of lengths typically measured. We discuss some of the nuances involved with collecting this amount of data that are pertinent to AFT statistical treatment before we discuss thermal modeling.

4.1.1 The Chi-squared test, sample size, and age precision

The typical first step in data evaluation is examining the population statistics of the AFT ages and track lengths. The χ^2 test is used to determine if the underlying grain ages in a sample belong to a single statistical population with a common true age (Galbraith, 2005).

A fission-track dataset exhibiting overdispersion beyond what is expected from random analytical uncertainties, indicates the likely presence of underlying 'geological' complexity (Kohn et al., 2024). Thus, failure of the χ^2 test does not necessarily indicate poor data quality, and data dispersion can be attributed to various factors, most notably, differential annealing response among grains (usually in sedimentary samples, but can be present in granitic rocks; O'Sullivan & Parrish, 1995), or high single-grain age precision (Vermeesch, 2017, 2019; McDannell, 2020). Depending on apatite yield, the external detector AFT method (EDM) convention is to analyze fewer grains (\leq 20), whereas LAFT analyses usually include > 20–40 grain-ages for bedrock samples. Therefore, failure of the χ^2 test is more likely for large datasets because even minor deviations from the assumed commonage model can lead to rejection by the χ^2 test (Galbraith, 2005; Kohn et al., 2024).

Even though the LAFT method and EDM produce statistically indistinguishable results (Seiler et al., 2023), higher age precision has been reported for granitic rocks analyzed using LA-ICP-MS in some studies (e.g., Ketcham et al., 2018). A more recent systematic comparison of AFT methods demonstrated similar precision for old and young rock samples (thermal histories of varying complexity) when a similar laboratory age standard calibration system was used (Seiler et al., 2023). In that study, however, samples of basement rocks with complex thermal histories failed the χ^2 test when analyzed using both the EDM and LAFT. Common features of those samples were a higher number of analyzed grains and high track counts. At face value, our combined AFT data aliquots exceed typical analytical sample sizes and are characterized by precise ages, making failure of the χ^2 test more likely. Our samples fail the χ^2 test and exhibit moderate-to-high age dispersion of 20–30% yet were conservatively interpreted as overdispersed single populations—we discuss further the support and rationale for this interpretation in more detail below.

4.1.2 Spontaneous track density and relative error

Precambrian samples often exhibit high track densities, usually because they have remained at low temperatures for extended periods of time, allowing a significant accumulation of tracks. The number of spontaneous tracks accounts for most of the AFT analytical uncertainty (Vermeesch, 2017, 2019). Precambrian rocks often yield highly precise AFT ages due to elevated spontaneous track counts; however, this precision can

sometimes lead to χ^2 test failure. Precision related to N_s is obvious when examining relative uncertainties for track counts between hypothetical apatites with N_s . Our samples are characterized by single-grain age uncertainties of ~5–10% due to high track counts for most grains. This observation also implies a potential FT community analytical bias (Donelick, 2005), whether conscious or unconscious, towards grains with lower spontaneous track counts ($N_s \le 100$). Explicit motivations may include a desire for samples to pass the χ^2 test, while implicit ones could involve an analyst's preference for easier-to-count grains or a lack of confidence in measuring grains with high track densities accurately (O'Sullivan, 2018; McDannell, 2020, for discussion).

4.1.3 Apatite composition and mixture modeling

Across our samples, apatite composition is fairly uniform within a narrow range of eCl and the total age dispersion remains similar when grain aliquots are combined, which in our experience with LAFT data, typically implies a single underlying, but overdispersed, age population (e.g., McDannell et al., 2019a; McDannell, 2020). A different challenge arises if there is a spread in true ages within a sample that instead represent a mixture (Galbraith & Green, 1990). In finite mixture modeling of AFT data, each age component is assumed to have a fixed (normal) dispersion governed by Poisson counting statistics (Galbraith & Laslett, 1993), however, the assumption of equal dispersion across components may not always be valid. For instance, grains subjected to different thermal histories or characterized by uranium zoning may show varying degrees of dispersion that are experimentally sourced and not statistical in origin. The precise estimate of the AFT central age is based on a log-likelihood algorithm, which uses grain-count data as weights to account for the variable precision of the grains (Galbraith & Laslett, 1993). While the central age model accommodates such variability by allowing dispersion to be a free parameter, mixture models constrain this, which may limit their interpretive flexibility when dealing with heterogeneous datasets.

Age dispersion in cratonic basement rocks may result from slow cooling and differential annealing effects from compositional heterogeneity (Kohn et al., 2024, their fig. 4), though these effects are often subtle due to the nature of cratonic surface histories. Such a process could also hypothetically produce a continuous distribution of ages rather than

the discrete components typically assumed (Vermeesch, 2019). A finite-mixture estimator (Galbraith & Green, 1990) is theoretically capable of resolving an unlimited number of age components; however, in practice, the number of components that can be reliably estimated is constrained by finite sample size. Moreover, from a geological perspective, resolving many components is impractical, as it may lead to overinterpretation of random noise or minor age variations that lack physical significance. Mixture modeling (Galbraith & Green, 1990; Galbraith & Laslett, 1993) using the DensityPlotter v. 8.4 software (Vermeesch, 2012) indicates multiple age components (> 3–5) best explain our samples. This is primarily due to the large sample size, which includes many highly precise grain ages, making it difficult to determine whether apparent age components reflect real geological signals or are simply mathematical artifacts resulting from fitting discrete components to what may be continuous age distributions (e.g., Härtel et al., 2024).

Figure 5A, D, G show radial plots of single-grain ages and their precisions (Galbraith, 1990), with more precise analyses being further from the origin. The results of mixture modeling are shown (dashed lines) along with plots of eCl versus AFT age for only the grains in aliquot-2. Two components were specified so that we could consider whether dispersion is related to apatite compositional heterogeneity. We focused on aliquot-2 because we only have replicate EPMA analyses for those data. To further investigate single-grain age dispersion, we examined the eCl parameter (equation 3) derived from the two EPMA spots to determine if intragrain compositional variation could be linked to the model age components. The eCl values calculated from the EPMA data collected near the laser ablation pit (spot A) display a near continuum of single-grain ages that correlate with apatite composition or indicate complete mixture component overlap for each sample (fig. 5B, E, H). Using only the calculated eCl from spot-A the two mixture components for each sample are not supported, suggesting grain ages are perhaps better represented by a continuous distribution, or alternatively, more components. However, the addition of > 2 components is not supported by the kinetic data (there are no trends when considering measured Cl or the D_{par} parameter).

Discrete components become more evident if both EPMA spots are considered in the context of whether each single-grain age falls into the more or less retentive kinetic component from mixture modeling, that is, by utilizing the minimum or maximum eCl

value for each replicate EPMA analysis (fig. 5C, F, I). This is best observed in sample 97-10-365 where the eCl calculated from EPMA spot-A near the ablation pit shows complete kinetic overlap (fig. 5B), whereas when the minimum or maximum eCl value is considered in relation to the mixture model peaks, there is better separation into discrete kinetic groups (fig. 5C). An approximate continuum of ages or no clear relationship between eCl and age remains for samples CB99-227 and 12RM086 (fig. 5F–I). As expected for granitic protoliths, we conclude that overall our samples have fairly homogeneous kinetics. Figure 5 shows that the variation in the grain ages is mostly independent of the eCl kinetic parameter and rules out apatite compositional heterogeneity as the *primary* source of dispersion.

We note, however, that an important implication of the observed relationship between age and kinetic parameter is that an r_{mr0} value obtained from a single EPMA spot may not be representative if there is intragrain compositional variability. This suggests that it is plausible for multikinetic AFT sub-populations to be expressed in cratonic basement samples due to subtle variations in apatite composition and therefore annealing susceptibility. One reason kinetic-based components may be poorly resolved is because the compositional variance is small—at or beyond the resolution of the current r_{mr0} calibration(s) (Carlson et al., 1999; Ketcham et al., 1999, 2007). A similar resolution limit for kinetic component discrimination is apparent for D_{par} (Issler et al., 2022). However, a complicating, if not obscurant factor is that track annealing behavior (and thus r_{mr0}) is poorly constrained beyond common fluorapatite (eCl of ~ 0.0 to ~ 0.05 apfu; Issler et al., 2022), therefore the total degree of separation between apparent kinetic groups explained by the r_{mr0} parameter may be underestimated. Additional annealing kinetic characterization and re-calibration of the r_{mr0} relationship would be required to test this hypothesis (e.g., Donelick et al., 2023).

4.1.4 Daughter-Parent (Age-U) relationships

In addition to the typical examination of single-grain ages with respect to a kinetic parameter like D_{par} or r_{mr0} , we also looked at the relationship between AFT ages and uranium content. Our AFT samples display a negative date-U trend (fig. 6), which has been interpreted as non-thermal 'enhanced annealing' from the effects of α -particle radiation

(Hendriks & Redfield, 2005; McDannell et al., 2019a). According to the radiation-enhanced annealing conceptual model, increased uranium content accelerates annealing due to atomic-scale partial recrystallization, resulting in a systematic pattern of low-U grains with older ages and high-U grains with younger ages. Enhanced annealing has been confirmed by laboratory experiments on apatite (e.g., Carpéna & Lacout, 2010; Li et al., 2017, 2021). Alpha-damage has a negligible effect on fission-track annealing in young samples (Zeng et al., 2025), but experiments on apatite from old cratonic rocks have not been performed¹.

Plots of U concentration versus AFT age provide a diagnostic for identifying possible trends between radiation damage and apparent age dispersion. However, Härtel et al. (2022) found that apparent correlations between AFT age and U are also possibly 'spurious' when there is a linear daughter-parent (D-P; i.e., age-U) relationship. The D-P plot distinguishes systems with proportional D-P relationships, which yield uniform ages, from those with non-linear trends indicative of variable daughter retention (either enhanced or diminished). Thus, radiation damage can cause non-linear deviations from the expected D-P relationship. An overdispersed, linear D-P trend offset from the origin plausibly indicates a spurious relationship.

As discussed by Härtel et al. (2022), where t is age, and the correlation $(r_{t,U})$ between the ratio $(t \approx D/P)$ and its denominator $(U \approx P)$ is approximated by the Chayes (1949) equation:

$$r_{t,U} \approx \frac{r_{DP}v_D - v_P}{\sqrt{v_P^2 - 2r_{DP}v_Dv_P + v_D^2}}$$
 (4)

Non-peer reviewed preprint submitted to EarthArXiv. Under review with American Journal of Science.

_

¹ One unresolved issue is that the present amount of net radiation damage may not be indicative of how radiation damage influenced track retentivity throughout the sample's full thermal history

where, r_{DP} is the Pearson correlation coefficient of D and P, and $v_D = \sigma_D/\mu_D$ and $v_P = \sigma_P/\mu_P$ (standard deviations and means) are the coefficients of variation for D and P, respectively. Figure 6 shows plots of U/Ca and AFT age (panels A, C, E) and D-P plots for our samples using the approach of Härtel et al. (2022). Robust regressions (Huber, 1973) were applied to our D-P plots using a piecewise loss function that downweights the influence of outliers and stabilizes fits in the presence of non-Gaussian or heavy-tailed errors (e.g., Sun et al., 2020). A statistically significant negative linear trend exists between our single-grain ages and U/Ca (fig. 6B, D, F). Spontaneous track count variability is evident for our LAFT samples, each also characterized by a non-zero positive intercept and increased dispersion at high U/Ca ratios. This suggests to first-order that observed age-U trends are dominated by statistical scatter rather than radiation-damage effects, consistent with a spurious correlation.

A factor to consider in this context is LAFT U measurement. Scatter at higher values on our D-P plots may reflect U/Ca measurement noise or some degree of non-uniform U distribution. While calculated LAFT ages remain accurate (Seiler et al., 2023), single-spot U measurements, as implemented for the samples herein, can sometimes cause age overdispersion and produce a negative correlation between individual grain ages and uranium—a relationship that has been partially attributed to U zonation within the grain (Cogné & Gallagher, 2021). The estimated dispersion for our samples is more than twice the expected dispersion for Poisson-variation alone (table 1), which is ~10% for our samples. One of the experimental factors that contributes the most non-Poisson variation to an AFT analysis is U inhomogeneity (Green, 1981). The key objective is to estimate the average ²³⁸U concentration within the area or volume defined by the counted spontaneous tracks in the grain. The accuracy of this estimate may be constrained more by the spatial variability in U distribution than by the analytical precision. We did not document strong areal or down-pit U zonation, since this could be avoided through optical examination of the spontaneous track density in individual grains or by filtering any high-U 'spikes' from down-hole measurement data, however, we cannot rule zonation out entirely. Ultimately, multiple sources of dispersion are likely for our LAFT samples (leading to χ^2 test failure), including, the large number of single-grain analyses; dating old apatites with high spontaneous track counts (and thus high internal age precision); use of a single, small laser spot for determining U content; and minor differences in annealing susceptibility (i.e., AFT age) due to apatite compositional heterogeneity.

4.2 Thermal History Model Setup

To reconstruct the time-temperature histories recorded by the AFT data, we applied inverse thermal modeling using the QTQt and AFTINV programs under a shared set of geologically informed constraints. QTQt model runs were setup with the same general prior for the thermal history: 300 ± 300 Ma and 70 ± 70 °C, a modern surface temperature of 2.5 ± 2.5°C, and a maximum allowed heating/cooling rate of 3°C/My. Rate limits were imposed to prevent extreme temperature fluctuations and the acceptance of t-T paths that are unlikely for this geologic setting (the allowance of higher rates during tests did not change the form of the thermal histories). The upper model limit was not extended beyond 600 Ma because the data do not contain information relevant to the older history due to partial thermal resetting in the Phanerozoic. The multikinetic annealing model of Ketcham et al. (1999) was used with the r_{mr0} kinetic parameter and track lengths were modeled including c-axis angle projection. Apatite composition was allowed to vary within uncertainty for the AFT data and the initial track length (l_0) was calculated based on composition. Models were run for a total of 700,000 iterations, with an initial burn-in of 200,000 iterations. The 500,000 MCMC iterations retained after burn-in were used to approximate the posterior probability distribution of t–T paths.

AFTINV models were setup similar to the QTQt models. The initial boundary conditions involve randomized selection of thermal minima within user-specified time intervals, and the initial bounds were specified to require a single thermal minimum ($\leq 30^{\circ}$ C) in the Ordovician and a second thermal minimum in the middle–late Mesozoic (two randomly selected thermal peaks are also required to be $\geq 30^{\circ}$ C). Maximum rates were reduced in AFTINV to 2° C/My because trial models generally exhibited rates on the order of $\leq 0.5^{\circ}$ C/My. Furthermore, the low degree of thermal annealing experienced by our samples and the 700 My total model time make high rates prohibitive for efficiently searching t-T space. Note that the total model time domain between QTQt and AFTINV inversions are different; this is mostly due to the fact that a larger general prior in QTQt favors simpler models if data sensitivity is limited, that is, if samples are partially reset,

whereas this matters less in a more structured AFTINV model setup with fixed time steps (5-My time steps from 700–0 Ma) and more explicit assumptions.

We implemented a MC search in AFTINV at the 0.05 level to find 300 suitable t-Tsolutions that fit the AFT ages and track lengths at 2s and then used the CRS algorithm to update and refine the 0.05 solution pool to the 0.5 statistical fit level (also 300 solutions). The CRS algorithm excels at finding multiple solution modes that fit the data (if they exist), which can be valuable for evaluating model trade-offs between data/model fit, heatingcooling rates, heating (annealing) magnitude, and minima/maxima timing. The model fits to the observed AFT age and track length distribution are calculated using the same methodology as Ketcham (2005). We mainly focus on the set of 300 CRS solutions at the 0.5 level but present the minimum objective function solution as the best model representing the entire pool. The minimum objective function (best fit) solution is defined in AFTINV as either the t-T path with the lowest combined objective function GOF for AFT age and the track length distribution, or the lowest maximum objective function for either the age or track length distribution (latter approach is used in HeFTy)—our preferred model was the one that provided the best fit to the robust track lengths, therefore the t-Tpath that satisfied that criterion is highlighted and discussed. We justify focus on the bestfit path because the CRS algorithm optimizes the solution pool, thus, overall, the solutions tend to be similar in style and structure with modest differences attributed to heating/cooling rates and locations of the thermal minima and maxima for individual paths.

4.3 QTQt Inversion Results

4.3.1 Models without constraints to test sensitivity

We examined the ability of the AFT data to resolve the shield thermal history and QTQt model results are shown in fig. 7 as heat maps of t–T path density, where brighter colors are higher relative posterior probability, that is to say, the relative frequency of the MCMC algorithm generating an accepted path through that region of t–T space. The density of paths (i.e., higher relative probability) is proportional to the likelihood and is shown as the path density normalized to unity (0–1). A maximum value of 1 is equal to the upper 95^{th}

percentile of path density. Subtle changes in the (log) likelihood value are more due to the transdimensional aspect of QTQt, that is, the iterative addition (birth) or subtraction (death) of t–T points (Gallagher, 2012).

Regions of high path density in the model ensemble represent portions of *t*–*T* space that are more frequently visited by accepted models, and therefore approximate where the 'true' thermal history is more likely to have passed. To be clear, individual paths that pass through these [high path density] regions are not inherently more probable than other accepted paths, because each accepted MCMC path is an equally valid sample from the posterior distribution. The density reflects the frequency with which similar paths are accepted, not the relative likelihood of any single path. This concept is closely related to the marginal posterior probability, which in Bayesian terms describes the probability distribution of a single parameter (e.g., temperature at a given time) while integrating over all others. In QTQt, the marginal posterior probability at a specific time reflects the distribution of temperatures sampled across all accepted models, independent of temperatures at other times. This provides a useful visualization of uncertainty and model support at individual time steps, without assuming a fixed relationship across the entire thermal history.

QTQt plots show the entire accepted t–T path distribution and individual representative paths, including the Maximum Likelihood (best fitting model shown as red curve; usually the greatest number of t–T points), Maximum Posterior (green curve), which is the thermal history that has the maximum posterior probability, and is usually the simplest (fewest t–T points). The posterior probability combines the likelihoods and prior probabilities for each model, attempting to balance fitting the data with model complexity. The Maximum Mode solution (gray curve) is constructed at a 1-My interval by running along the peak of the marginal distribution, while the Expected model is the average of the marginal distribution shown with the \pm 95% credible interval (black curves). The Maximum Mode and Expected models are not true solutions but instead summarize the accepted pool of histories. Refer to Gallagher & Ketcham (2020) for more details on individual QTQt models.

We initially focus on the entire accepted distribution of paths, particularly the 'unconstrained' models shown in fig. 7A, D, and G. The unconstrained models do not include t-T constraints as prior information and here they assess the overall t-T sensitivity of the data. These examples reflect the ability of the AFT data to resolve the thermal history

with the necessary level of complexity to adequately explain the data. Note that this does not mean that the true thermal history isn't more complex, but rather, any additional complexity (that does not compromise fitting the data) is not actually required by the data and so needs to be justified independently. The optimal Max. Likelihood model solutions indicate two distinct heating events. The timing of these events is poorly resolved, a result of the low magnitude of total annealing observed in the samples, compounded by the simplicity of the accepted thermal histories. The Max. Posterior model generally exhibits less complexity and maintains an acceptable fit to the data, characterized by nearly monotonic cooling, though its fit is suboptimal compared to the Max. Likelihood path. Monotonic cooling is unrealistic for this setting because we have independent geologic information and prior thermochronological studies that suggest a more complex history (for summary, Kohn & Gleadow, 2019). The regional geology and the best-fit Max. Likelihood t-T solutions demonstrate that two discrete thermal peaks are more likely for the central Canadian Shield.

The unconstrained QTQt models reveal complex thermal histories that are broadly consistent with regional geology, even without imposing external constraints. These results illustrate that, even without the application of prior constraints, QTQt inversions supported by a large track-length dataset can yield robust insights into complex thermal histories. This finding highlights the importance of track-length data as an independent t-T constraint, especially for detecting episodes of reheating. We acknowledge that geological constraints are often necessary for t-T model refinement and to ensure accurate interpretation, especially over long timescales where uncertainties in geologic context can be nontrivial. The inclusion of irrefutable model constraints is an additional practical step to guide the inversion toward geologically reasonable outcomes, but the unconstrained results serve as a baseline to assess how much information is truly data-driven (as opposed to models being driven by interpretive assumptions).

4.3.2 Applied geologic constraints

Geologic constraints were incrementally applied to subsequent models (fig. 7B, C, E, F, H, I). The geologic information being evaluated includes two distinct times in the past that we can reasonably assume basement was at near-surface conditions (15 \pm 15 °C) based on the

regional information discussed previously and the unconstrained model results. The models imply heating occurred in the late Paleozoic and was preceded by cooler temperatures, which are constrained by the deposition of Ordovician carbonates near the AFT sample localities. The presence of thin Jurassic strata in the Moose River Basin (Norris, 1977), the ca. 180–170 Ma Ma kimberlite emplacement ages (Sage, 2000), and the general t-T model trends of cooler temperatures between 200-100 Ma collectively reinforce that basement was again exhumed by the Middle Jurassic. This information was sequentially added to other models as constraint boxes at: (i) 450 ± 10 Ma and (ii) 170 ± 10 Ma. The addition of Ordovician and Jurassic constraint boxes refined the accepted t-T solutions but the constraints were not strictly necessary, since the 'unconstrained' models reproduce the two heating events. The constraints were added to ensure the inversions honor the wellestablished regional heating-cooling episodes. Many practitioners emphasize that geological constraints are essential for producing reliable thermal histories. While such constraints can help guide models toward plausible solutions, our results show that with sufficient and high-quality data, unconstrained models can still recover major thermal events accurately.

Model path behavior is further discussed with respect to the final models with all applied constraints to establish the general features of the thermal histories (fig. 7C, F, I). The balance between data/model fit and path complexity for the Max. Likelihood and Max. Posterior models were considered for each AFT sample to determine simple history style behaviors. The best-fit Max. Likelihood model paths for samples 97-10-365, CB99-227, and 12RM086 suggest maximum Paleozoic heating to ~67 °C at 247 Ma, ~66 °C at 259 Ma, and ~82 °C at 272 Ma, respectively. The Max. Posterior path for each sample exhibits maximum heating to ~71 °C at 264 Ma, ~66 °C at 284 Ma, and ~75 °C at 267 Ma, respectively. The early Cenozoic Max. Likelihood peak shows heating to ~40 °C at 16 Ma, ~54 °C at 16 Ma, and ~45 °C at 21 Ma, for each sample respectively. The Cenozoic Max. Posterior peak shows heating to ~49 °C at 20 Ma, ~53 °C at 16 Ma, and ~47 °C at 29 Ma, respectively. The fits between the observed and predicted AFT age and track length distribution for all of the accepted paths are shown for each example (fig. 8). The accepted AFT central ages are typically at the margin of acceptability, which may be due to the lack of a high-temperature constraint to guide the inversion, or the high number of track lengths

have more influence on the model.

The Max. Mode model is examined here to as a generalized metric for determining the timing of maximum heating, since this model summarizes the accepted history pool using the peak of the marginal distribution, i.e., the region of highest path density (the Expected model is biased to lower temperatures due to smoothing and is often a poor fit to the data). The ad hoc conditional t-T criteria we applied reference the times when the modal temperature passed above/below ~50 °C and above/below ~35 °C for each respective thermal peak. Sample 97-10-365 displays maximum heating between ca. 336-223 Ma, whereas CB99-227 maximum heating occurs somewhat earlier between ca. 360-239 Ma, and sample 12RM086 shows maximum heating between ca. 356–239 Ma. The timing of the second reheating peak was estimated for sample 97-10-365 to be between ca. 100–17 Ma, whereas sample CB99-227 was similarly between ca. 94–12 Ma, and the peak for sample 12RM086 was between ca. 93–29 Ma. The upper 95% credible interval maximum temperature for each peak of each for the respective samples was 76 °C from 272–270 Ma and 57 °C at 25 Ma (97-10-365); 79 °C at 255 Ma and 62 °C at 26–24 Ma (CB99-227); 75 °C at 270–265 Ma and a diffuse maximum peak of ~48 °C between 95–30 Ma (12RM086). These trends suggest Paleozoic-early Mesozoic heating was of broadly similar timing and magnitude, but perhaps greater nearer to the Moose River Basin, whereas the late thermal peak was consistently early Miocene (latest Oligocene?, but as early as Cretaceous) and similar in magnitude across the Hudson Platform.

4.3.3 Conditional probabilities

Examining conditional probabilities is a practical way to assess model correlations and provides an additional test of model non-uniqueness within a Bayesian framework (e.g., Fox & Carter, 2020). The parameters (time and temperature) of the inverse problem are highly correlated—any change in temperature at one point in time can be compensated by an opposing change in temperature at another point in time (Willett, 1997)—thus (marginal) probabilities are dependent on all aspects of a proposed thermal history. A key question is whether some accepted paths in the posterior distribution of the 'unconstrained' QTQt models exhibit distinct thermal history characteristics, and if so, whether any of these

t—T paths independently align with local geological evidence. The intent of this analysis is not merely to reproduce results from the 'constrained' inversions, but to demonstrate how 'unconstrained' models can still reflect geologically plausible features, even in the absence of imposed t—T constraints. This provides a way to assess the resolving power of the data and to explore the sensitivity of the posterior distribution of accepted paths.

The concept of relative probability serves as a useful visualization tool for evaluating the likelihood that the true thermal history passes through a specific region of t–T space. This can occur either through a set of histories sharing similar t–T trends or by structurally different paths that converge or overlap within the same region of t–T space. In models without imposed constraints, the posterior distribution may include paths with a varying number of t–T points and overlapping paths can create the impression that certain features of the thermal history are more probable, however, such features may be reproduced by a subset of histories and/or be obscured by other solutions. This comparison is important given criticisms that geologically implausible t–T paths may be accepted in 'unconstrained' Bayesian t–T models (see discussions of Green et al., 2020; Flowers et al., 2022; McDannell et al., 2022a). By inspecting the conditional probabilities of accepted t–T paths, we can better assess which features are supported by the available data, thereby improving confidence in any further interpretations.

We show an example of applying conditional probability tests (fig. 9) to the 'unconstrained' QTQt models for each AFT sample in fig. 7 (panels A, D, and G). This can be considered a retroactive or *a posteriori* probability 'filtering' of the entire accepted thermal history pool by retaining only the paths that, in this case, are at near-surface temperatures (0–30 °C) at both 450 Ma and 170 Ma (discarding all other paths). These conditional models exhibit the same thermal history features as those in fig. 7C, F, and I with model constraints—providing greater confidence in our geologic interpretations (discussed below).

4.4 AFTINV Inversion Results

The QTQt results exhibit general t-T trends that are useful for determining the surface history of the Hudson Platform. We utilized all observations from our collective QTQt

results and experiments, along with regional geology, to infer a history style that involves initial random cooling followed by two random heating-cooling cycles. The primary goal of AFTINV modeling was to compare model results generated with similar boundary conditions as QTQt but with a different statistical approach for thermal history acceptance. Since our samples are far from preserved Mesozoic rocks and there are more temporal and spatial uncertainties related to the late Paleozoic-Mesozoic Hudson Platform surface evolution, we investigated different thermal minima scenarios within the Paleozoic and Mesozoic intervals in AFTINV (i.e., timing based on QTQt model results and regional geology). This is a useful exercise because cratonic nonconformities can be potentially misleading when it comes to inverse modeling. Unconformities are commonly features that elide multiple periods of erosion and sedimentation—yet we typically have information constraining only the upper age limit of the depositional event that terminated the unconformity. Therefore, our constraint for basement being near the surface at 450 Ma or 170 Ma may represent a fraction of a much longer period of time when the Precambrian basement was near the surface. The Ordovician nonconformity also does not preclude earlier basement exposure. The nearby presence of the Cambrian (ca. 505 Ma) Deadwood Fm. in the Williston Basin (e.g., Burrus et al., 1996) and the ca. 530 Ma Mt. Simon Sandstone in the Michigan Basin (e.g., Catacosinos et al., 1990) imply regional basement exposure and localized shallow burial and erosion prior to the Ordovician.

We evaluated further the thermal minima timing in the Paleozoic and Mesozoic to allow the model to query between 470–450 Ma and 200–120 Ma, which is generally based on the Hudson Platform geology and the QTQt results. Sample 12RM086 required slightly different boundary conditions to achieve timely model convergence. A maximum of 5 °C/My cooling was allowed for the initial pre-450 Ma history (justified by QTQt results), due to the younger central age and less retentive average kinetics than the other two samples. In AFTINV the only requirement for the thermal minimum is that a single, randomly chosen 5 My time step is \leq 30 °C within each search interval, however this does not prevent other (contiguous) steps from being at similarly low temperatures in the model (i.e., an approximate thermal minimum prior to or after those times).

4.4.1 Sample 97-10-365

The AFTINV results yielded temperatures for the first thermal peak between $71-77^{\circ}$ C, with a weighted mean temperature of 75 ± 1 °C. The timing of the peak is between 250 Ma and 355 Ma, with a weighted mean time of 313 ± 16 Ma. The second thermal peak reached temperatures between 51-64 °C, with a weighted mean temperature of 58 ± 2 °C. The timing of the second peak is between 30 Ma and 90 Ma, with a weighted mean of 44 ± 16 Ma. The values given here refer to the solutions at 0.5 significance level (table 2). It is also important to keep in mind that the time step used in AFTINV was 5 My, therefore we lack temporal resolution below that value for individual times (i.e., minima or maxima).

4.4.2 Sample CB99-227

The AFTINV results yielded temperatures for the first thermal peak between 72–82 °C, with a weighted mean temperature of 75 ± 1 °C. The timing of the peak is between 235 Ma and 370 Ma, with a weighted mean time of 322 ± 23 Ma. The second thermal peak reached temperatures between 57–69 °C, with a weighted mean temperature of 62 ± 2 C. The timing of the second peak is between 30 Ma and 75 Ma, with a weighted mean of 47 ± 14 Ma.

4.4.3 Sample 12RM086

The AFTINV results yielded temperatures for the first thermal peak between 69–77 °C, with a weighted mean temperature of 72 ± 1 °C. The timing of the peak is between 255 Ma and 345 Ma, with a weighted mean time of 316 ± 14 Ma. The second thermal peak reached temperatures between 46-57 °C, with a weighted mean temperature of 53 ± 2 °C. The timing of the second peak is between 25 Ma and 115 Ma, with a weighted mean of 83 ± 7 Ma. We note that a similar two-peak AFTINV thermal history for sample 12RM086 (aliquot-1) was previously modeled as multikinetic with two age populations (McDannell et al., 2022c). A thermal maximum of 75 ± 2 °C was found in the Devonian (400 ± 26 Ma), followed by a second reheating event with a maximum temperature of 55 ± 3 °C at 76 ± 15 Ma. That model is similar to the one shown in figure 10, except the timing of the thermal peaks and temperatures are slightly offset, due to an enforced surface temperature minimum of 15 °C and the different annealing requirements for the grains treated as two ca. 585 Ma and ca. 370 Ma kinetic populations. For the model published in McDannell et al. (2022c), the

aliquot-1 EPMA measurements for the calculated eCl values were skewed negative, with the majority in the younger population (based on the data available at the time). This shift to lower retentivity (higher r_{mr0}) caused greater thermal resetting for the same heating magnitude, resulting in the recovery of a more precise timing for Paleozoic reheating.

4.5 Burial and Erosion History Interpretations

Similar Phanerozoic thermal histories are recovered for all of the samples in QTQt and the models independently corroborate the reasonably well-known cratonic surface history by requiring two reheating events that we interpret as sedimentary burial (fig. 7). Our thermal history models are nearly identical to other AFT thermochronology studies across the southern shield near the Hudson Bay and Williston basins (e.g., Crowley & Kuhlman, 1988; Crowley, 1991; Kohn et al., 1995; Osadetz et al., 2002; Feinstein et al., 2009). It is worth noting that the same priors were used for the three samples (that are in close proximity to one another) with slightly different data properties (i.e., ages, apatite chemistry, number of track lengths, etc.), so the similarity in the model results demonstrates that a similar history can satisfy all of the data. The thermal histories suggest poorly resolved surface conditions in the late Precambrian to early Paleozoic (fig. 7) and indirectly require periods at lower temperatures in the middle Mesozoic. The pre-450 Ma history suggests that the AFT data can be explained by some combination of cooling from temperatures near 100 °C or by residence at low temperatures and thermal resetting. A nearby Hudson Platform sample locality (see fig. 2) reinforces this notion (McDannell & Keller, 2022). In McDannell & Keller (2022), a QTQt model integrated zircon (U-Th)/He, AFT, and apatite (U-Th)/He thermochronometers to reconstruct a thermal history characterized by rapid cooling during the Cryogenian, followed by sustained low-temperature conditions (< 50 °C) preceding Paleozoic reheating. Their results were interpreted to reflect near-surface residence of the basement between ca. 635–475 Ma.

The QTQt inverse models best resolve a broad thermal peak between approximately latest Devonian to Triassic (*ca.* 360 to 240 Ma) for all samples that is consistent for all *t*– *T* simulations (fig. 7; albeit more resolved in panels C and F). The timing of maximum temperature is poorly constrained due to the low degree of thermal annealing within the

PAZ for these apatites and reflects the correlation between time and temperature, that is, if the model is allowed to adjust both, it can trade a longer duration for a lower temperature, or vice versa, to fit the same data. Step-wise addition of the Ordovician and Jurassic constraint boxes (fig. 7B–C and E–F) refine the overall history results and the requirement of two heating events by the AFT data suggest maximum heating to ~65–75 °C occurred in the late Paleozoic, which would equate to more than a kilometer of burial—in broad agreement with the regionally preserved intracratonic basin strata.

Maximum burial heating occurred sometime between the late Devonian and early-middle Triassic, with a second event in the late Cretaceous to early Miocene across the Hudson Bay region. The AFTINV results provide a refinement of these burial estimates (table 2; figs. 10 and 11). The earliest peak burial times are consistent with the age of the preserved upper Devonian section (Pinet et al., 2013; Lavoie et al., 2015; Armstrong et al., 2018), whereas the existence of Carboniferous (e.g., Tillement et al., 1976) and Permo-Triassic strata that were potentially deposited (and subsequently eroded) cannot be ruled out. The Michigan and Williston basins contain a few hundred meters of Pennsylvanian and Jurassic strata (Sloss, 1963; Catacosinos et al., 1990; Burrus et al., 1996; Burgess, 2019)—implying a common Paleozoic history for interior North America (e.g., Beaumont et al., 1987; Sanford, 1987; Burgess et al., 1997; Patchett et al., 2004). These models further support the idea that the Hudson Bay sedimentary succession is an erosional remnant (e.g., Pinet et al., 2013; McDannell et al., 2022c) and that the Hudson Bay and Williston basins were intermittently connected (e.g., Sanford, 1987; Norris, 1993).

The extent of Carboniferous burial across the central Canadian Shield, as well as the presence of rocks from this period in the Hudson Bay Basin, remains debated. Possible explanations for these features in our inversions are that: (i) Pennsylvanian strata are preserved in the Hudson Bay Basin and the findings of Tillement et al. (1976) are correct, or (ii) thin Carboniferous rocks were deposited, but were then eroded outside of the main Hudson Bay depocenter as a result of lower preservation potential near the basin margins (due to less accommodation space than other intracratonic basins), or (iii) Carboniferous strata were not deposited in the Hudson Bay Basin. The similarity between the thermal histories of our samples and those from Williston basin (Osadetz et al., 2002) suggest to us that the first two explanations are the most likely.

The cooling trend observed in our models from the late Carboniferous through the Jurassic coincides with the assembly of the supercontinent Pangaea, initiated by the collision of Laurussia and Gondwana around 320 Ma (Domeier & Torsvik, 2014). This also corresponds with the predicted timing of dynamic mantle uplift beneath Laurentian North America (Cao et al., 2019). The erosion associated with continental uplift, marked by unconformity formation (Sloss, 1963), was potentially influenced in part by global sealevel fall (Haq & Schutter, 2008) during the Late Paleozoic Ice Age that began around 335 Ma and lasted until about 260 Ma (Montañez & Poulsen, 2013). Sediment preservation rates during that time were among the lowest observed in the past 700 million years (Bell & Laine, 1985; Peters, 2006).

The subsequent Mesozoic-Cenozoic history is characterized by inferred burial, primarily during high Cretaceous sea level and flooding of the continent (e.g., White et al., 2000; Müller et al., 2008), followed by erosion until present day. The final cooling event begins as late as Oligocene-Miocene time; the White River Group (< 38 Ma in age) in the Williston Basin provides indirect geological support for this, as it records the last regional burial event during the Paleogene, which was followed by Miocene erosion (Kohn et al., 1995; Burrus et al., 1996; Osadetz et al., 2002). While speculative, it is possible that some of the latest model cooling could be attributed to climatic cooling since the timing approximately aligns with climate change and the growth of the Antarctic ice sheet, including ephemeral northern hemisphere Oligocene-Miocene continental glaciation (Eldrett et al., 2007; DeConto et al., 2008; Hyeong et al., 2014; Tripati & Darby, 2018).

To estimate past sedimentary thicknesses, we applied a mean paleosurface temperature of 25 ± 5 °C for the late Paleozoic and late Mesozoic based on a global Phanerozoic temperature reconstruction (Judd et al., 2024). The published thermal history for the nearby Pinawa Underground Research Laboratory (URL) borehole in SW Manitoba (Feinstein et al., 2009) was used to estimate the paleogeothermal gradient for the Paleozoic (40-50 °C/km) and Mesozoic (20–25 °C/km). Values for surface temperature (T_s), geothermal gradient (T_g) , and the thermal maximum (T_b) from each t-T model were used to solve the equation $(T_b - T_s)/T_g$. We converted temperature to depth by taking 10,000 random samples normal distributions for each variable Julia using (https://github.com/OpenThermochronology/JuliaThermoTools). A geothermal gradient

of 40 ± 5 °C/km was specified for the Paleozoic, whereas the late Mesozoic geotherm was set to 24 ± 2 °C/km. The mean peak temperatures for each AFTINV model at the 0.5 significance level in table 2 indicate average burial depths of $\sim 1.27 \pm 0.22$ km (97-10-365) and CB99-227), and $\sim 1.19 \pm 0.20$ km (12RM086) in the Paleozoic. If a typical continental geothermal gradient of 24 ± 2 °C/km is instead assumed for the Paleozoic, then the average burial depth is $\sim 2.06 \pm 0.27$ km. We favor the former estimate, as the global average geothermal gradient for intracratonic basins is approximately ~40 °C/km and areas with sedimentary cover of ~1.0–1.5 km typically exhibit geothermal gradients that are at least 5–10 °C/km higher than the continental crust average of 25 °C/km (Kolawole & Evenick, 2023). The late Mesozoic-early Tertiary thermal peaks translate to burial of $\sim 1.39 \pm 0.26$ km, $\sim 1.55 \pm 0.26$ km, and $\sim 1.17 \pm 0.25$ km for each respective sample. The mean thicknesses of eroded Phanerozoic strata are 1.24 ± 0.21 km and 1.37 ± 0.26 km for those respective time periods. In the Williston Basin, independent erosion estimates derived from preserved well stratigraphy and geohistory modeling show remarkable agreement: ~1.1 km of rock was removed after 300 Ma, followed by an additional ~1.2 km during the midto-late Tertiary (Kohn et al., 1995; Burrus et al., 1996).

4.6 Track Length Data Acquisition in the Context of Deep-Time Thermochronology

Due to the large amount of track data collected in this study we take the opportunity to discuss a few points regarding applied deep-time AFT thermochronology, specifically the importance of track lengths for inverse modeling. We emphasize that this concern is particularly relevant in cases where guiding geological constraints are absent, or where few assumptions are made *a priori* about thermal history.

The principle source of uncertainty in fission-track length data is the discrete number of finite lengths collected rather than measurement error (Willett, 1997). Inadequate characterization of length distributions may affect our ability to recover thermal history information. While this is not conceptually novel (e.g., Ketcham et al., 2009)— what constitutes a robust track length data set and if those data can independently support geologic observations is underexplored in the published literature. The convention has been

for analysts to measure a minimum of \sim 50–100 track lengths to obtain a representative distribution and a stable mean length for use in t–T modeling (Rahn & Seward, 2000; Barbarand et al., 2003b). While the optimal number of data to collect depends on the geological problem, 100 tracks is generally considered sufficient for statistical rigor and analytical economy (Donelick, 2005). For instance, if a volcanic rock is rapidly cooled and subsequently undisturbed, it will generally be characterized by a narrow unimodal (> 14 μ m) track-length distribution (e.g., Gleadow et al., 1986b; our fig. 1). In this case, measuring 100 track lengths is adequate to fully characterize the thermal history. An implicit analytical assumption is that at some finite number of tracks, there are diminishing returns regarding the information contained in, and retrievable from, AFT data. In principle, this is dependent upon the complexity of the thermal history (i.e., the amount of annealing experienced by a sample) and the accuracy of annealing kinetic calibrations.

In detail, many different thermal histories can satisfy a given track length distribution. However, even if the distribution looks similar between an example with many tracks and fewer tracks, the possibility to resolve multiple heating-cooling events in a history is reduced in the latter case. While the mean track length is a useful summary statistic, it is the width and shape of the track length distribution that are critical for modeling (Crowley, 1985; Gleadow et al., 1986b). The tails of the length distribution need to be well determined, namely, any shorter lengths that provide key temperature information must be included, which will typically require more measurements because short tracks have a lower probability of being observed and measured accurately (Laslett et al., 1982). The caxis angle projection of track lengths also plays a role by reducing length dispersion (Donelick et al., 1999), thereby taking advantage of the extra information provided by the annealing dependence on track orientation (Ketcham et al., 2009; Ketcham, 2019). If the distribution shape is well characterized then the thermal model can better deconvolve the mixed length components generated by different heating-cooling cycles. As noted by Ketcham et al. (2009) in their study of reproducibility between t-T inversions modeled using AFT data from different workshop volunteers: "Differences among inversions that persisted could be traced to differential sampling of long- and short-track populations among analysts." We therefore consider how the number of confined track lengths affects our ability to reconstruct the thermal history in QTQt and examine whether a typical AFT analysis with 50–100 track lengths contains enough information for deep-time thermal history inversion without making numerous model assumptions.

4.7 Track Length Distribution Resampling

Our models clearly show that our AFT samples have enough track lengths to indicate two thermal events without requiring t–T constraint boxes (fig. 7A, D, G). The inferred complexity of a thermal history (fig. 1) can be partially related to the number of track lengths that are collected by the analyst and how well those lengths define the real distribution (e.g., Barbarand et al., 2003b). To further explore this, we took the entire length datasets for two examples and randomly downsampled them using a Monte Carlo method, retaining $\sim 50\%$ and $\sim 10\%$ of the tracks in the original length distributions while maintaining a stable mean length within uncertainty (fig. 12). This was done to determine how well we can resolve the two thermal peaks (e.g., figs. 7A and D) with a reduced number of length measurements and simulates what a real AFT analysis would be like if fewer track lengths were measured.

Each resampled distribution was modeled in QTQt, while keeping the AFT age information fixed to assess how resampling of the total number of track lengths affected t-T resolution. The results shown in figure 13 indicate that there is an inadequate number of track lengths (≤ 100 lengths) to definitively resolve a complex two-peak thermal history involving moderate annealing without applying interpretation-based constraints. This was discussed conceptually as a intuitive result in McDannell & Issler (2021) and McDannell et al. (2022c). The thermal histories become increasingly simplified, exhibiting less t-Tstructure, and the resolution of the two thermal peaks progressively diminishes as the number of track lengths decreases to approximately 300-350 (fig. 13B-E), ultimately disappearing when fewer than 100 tracks are available (fig. 13C-F). Having fewer track lengths (and no other independent constraints) enables simpler histories to adequately fit the AFT data. This explains why some published QTQt models, especially those without imposed constraints or with limited additional thermochronometer data, display simple, monotonic cooling histories (e.g., Jess et al., 2019; Green et al., 2020). Similarly, the effect of reduced t-T sensitivity suggests that, in cases with fewer thermochronometers (track lengths being the most important for AFT), the data contain less resolving power and would

be less likely to 'reject' incorrect or improperly positioned constraint boxes (this is especially true for constraints placed at low temperatures where thermochronometers lack any sensitivity). In other words, models with more thermochronometric data necessarily impose stricter requirements on the fit between predictions and observations. These results suggest that in models with numerous t-T constraint boxes and limited resolving power, a wide range of t-T path proposals may be accepted. This observation raises questions about the extent to which t-T 'exploration boxes' serve as rigorous 'hypothesis tests' (e.g., Flowers & Peak, 2025).

One could argue that measuring more track lengths assumes that our annealing kinetic models are well determined, even though such models remain imperfect. However, we contend that measuring more track lengths in this work resulted in thermal histories that independently agreed with the well characterized geology of the Hudson Platform. This suggests that collection of > 500 track lengths does not result in overfitting the data and the modern AFT kinetic annealing model(s) in use (Ketcham et al., 1999, 2007) are reasonably well calibrated and remain the best empirically constrained of the available thermochronometric methods. The results of our modeling emphasize that the accepted norm of collecting ≤ 100 track lengths is possibly too low for many deep-time applications with complicated thermal histories. On the other hand, if a sample has undergone more recent total annealing and resetting, the measurement of additional track lengths will provide minimal t-T information (in proportion to the total amount of geologic time being reconstructed with the timing of resetting). Each problem is unique, and analyses should be tailored to optimize the amount of information available for modeling since a standardized approach may not yield sufficient data to clearly resolve significant thermal events. Since fission tracks are created at an approximately steady rate, we can estimate the number of track lengths needed to resolve a t-T path of a specific duration. The oldest tracks for our samples are about 600 Ma in age, and we report ~650–850 track lengths per sample, which is a sampling rate of 1.1 to 1.4 tracks/My. Thus, given our experience, a minimum of one measured track per million years of time is a reasonable analytical target for deep-time applications to ensure robust time-temperature control within an inversion.

5 CONCLUSIONS

Studies of cratons have shown that they are often characterized by histories involving periodic kilometer-scale sed- imentary burial. Due to the near absence of physical geologic constraints, detailed and objective thermal history reconstruction is often difficult. Apatite fission-track dating is uniquely powerful among thermochronometers because it provides two independent yet complementary constraints on thermal history: cooling ages that record the timing of thermal events, and confined track lengths that capture the magnitude and duration of heating—making it especially effective for deciphering complex burial and exhumation events. We discussed different strategies for inverse modeling applied to new apatite fission-track data from the central Canadian Shield for rocks bounding the Paleozoic nonconformity that included many more confined track-length measurements than a conventional analysis. Inversions of AFT data from three crystalline basement samples yielded results that are consistent with the regional shield geology without necessarily requiring the imposition of many model assumptions in the form of time-temperature 'exploration boxes'. Consideration of known geologic constraints with different inversion approaches allowed an assessment of the impact of data quantity/quality and constraints relative to models that did not apply a presupposed interpretive geological model. This study demonstrates that even in the absence of prior constraints, complex thermal histories can be effectively interpreted through unconstrained QTQt inversions when supported by a highly robust dataset. The broader adoption of recursive or hierarchical testing approaches to modeling, particularly in cases where geological constraints are limited, represents a valuable approach for improving thermal history reconstruction. Inverse thermal histories for Hudson Platform AFT data suggest peak sedimentary burial occurred during two periods with average burial estimates of $\sim 1.0-1.5$ in the late Paleozoic and $\sim 1.1-1.6$ km in the latest Mesozoic through early Cenozoic. These estimates imply at least ~2-3 km of total erosion over the past 500 million years for currently exposed shield locations with a negligible contribution to the erosional budget from the crystalline basement. Our results give credence to the view that the Canadian Shield is a regenerative geomorphic feature that has undergone repeated exposure throughout the Phanerozoic.

AUTHOR CONTRIBUTIONS

CRediT author statement. *K. McDannell*: Conceptualization, Investigation, Methodology, Formal Analysis/Modeling, Visualization, Funding Acquisition, Writing - Original Draft; *P. O'Sullivan*: Formal Analysis, Methodology, Resources; *K. Gallagher*: Validation; *S. Boroughs*: Formal Analysis, Methodology, Resources

ACKNOWLEDGMENTS

The Government of Canada Geo-mapping for Energy and Minerals Program (GEM-2) supported K.T.M. at the Geological Survey of Canada, Calgary from 2017–2020 during data collection. Thanks to Michel Plouffé (GSC Ottawa) for GEM program coordination and Nicolas Pinet (GSC Québec) and Christian Böhm (Manitoba Geological Survey) for correspondence and providing rock samples for analysis. We thank reviewers Marissa Tremblay and Cody Colleps for comments and chief editor Mark Brandon for detailed feedback and conversations that improved the manuscript. We are grateful to Tomoko Korenaga for her patience. Brenhin Keller is thanked for assistance with Julia code.

SUPPLEMENTARY DATA

Data tables for AFT ages, track lengths, apatite U-Pb, and electron microprobe data are available from the Open Science Framework (OSF) repository: https://osf.io/73u8j/

REFERENCES

- Ahern, J. L., & Mrkvicka, S. R., 1984, A mechanical and thermal model for the evolution of the Williston Basin, Tectonics, v. 3, n. 1, p. 79–102, https://doi.org/10.1029/TC003i001p00079.
- Anderson, S., Böhm, C., & Syme, E., 2010, Far North Geomapping Initiative: bedrock geological investigations in the Seal River region, northeastern Manitoba (parts of NTS 54L, M, 64I, P), In Report of Activities 2010, p. 6–22. Manitoba Innovation, Energy and Mines, Manitoba Geological Survey.
- Armstrong, D. K., Nicolas, M. P. B., Hahn, K. E., & Lavoie, D., 2018, Stratigraphic synthesis of the Hudson Platform in Manitoba, On-tario, and Nunavut: Ordovician-Silurian, Tech. rep., Geological Survey of Canada, Open File 8378, https://doi.org/10.4095/308418.
- Ault, A. K., Flowers, R. M., & Bowring, S. A., 2009, Phanerozoic burial and unroofing history of the western Slave craton and Wopmay orogen from apatite (U-Th)/He thermochronometry, Earth and Planetary Science Letters, v. 284, n. 1-2, p. 1–11, https://doi.org/10.1016/j.epsl.2009.02.035.
- Barbarand, J., Carter, A., Wood, I., & Hurford, T., 2003a, Compositional and structural control of fission-track annealing in apatite, Chemical Geology, v. 198, n. 1-2, p. 107–137, https://doi.org/10.1016/S0009-2541(02)00424-2.
- Barbarand, J., Hurford, T., & Carter, A., 2003b, Variation in apatite fission-track length measurement: Implications for thermal history modelling, Chemical Geology, v. 198, n. 1-2, p. 77–106, https://doi.org/10.1016/S0009-2541(02)00423-0.
- Beaumont, C., Quinlan, G. M., & Hamilton, J., 1987, The Alleghanian orogeny and its relationship to the evolution of the eastern interior, North America, In C. Beaumont, & A. Tankard (Eds.) Sedimentary Basins and Basin-Forming Mechanisms Memoir 12, p. 425–445. Canadian Society of Petroleum Geologists, Memoir 12.
- Bell, M., & Laine, E. P., 1985, Erosion of the Laurentide region of North America by glacial and glaciofluvial processes, Quaternary Research, v. 23, n. 2, p. 154–174,

- https://doi.org/10.1016/0033-5894(85)90026-2.
- Bond, G., 1978, Speculations on real sea-level changes and vertical motions of continents at selected times in the Cretaceous and Tertiary Periods, Geology, v. 6, n. 4, p. 247–250, https://doi.org/10.1130/0091-7613(1978)6<247:SORSCA>2.0.CO;2.
- Burgess, P. M., 2019, Phanerozoic evolution of the sedimentary cover of the north american craton, In The Sedimentary Basins of the United States and Canada, p. 39–75. Elsevier, 2nd ed., https://doi.org/10.1016/B978-0-444-63895-3.00002-4.
- Burgess, P. M., Gurnis, M., & Moresi, L., 1997, Formation of sequences in the cratonic interior of North America by interaction between mantle, eustatic, and stratigraphic processes, Geological Society of America Bulletin, v. 109, n. 12, p. 1515–1535, https://doi.org/10.1130/0016-7606(1997)109<1515:FOSITC>2.3.CO;2.
- Burrus, J., Osadetz, K., Wolf, S., Doligez, B., Visser, K., & Dearborn, D., 1996, A two-dimensional regional basin model of Williston Basin hydrocarbon systems, AAPG Bulletin, v. 80, n. 2, p. 265–291, https://doi.org/10.1306/64ed87aa-1724-11d7-8645000102c1865d.
- Butcher, G. S., Kendall, A. C., Boyce, A. J., Millar, I. L., Andrews, J. E., & Dennis, P. F., 2012, Age determination of the Lower Watrous red-beds of the Williston Basin, Saskatchewan, Canada, Bulletin of Canadian Petroleum Geology, v. 60, n. 4, p. 227–238, https://doi.org/10.2113/gscpgbull.60.4.227.
- Cao, W., Flament, N., Zahirovic, S., Williams, S., & Müller, R. D., 2019, The interplay of dynamic to-pography and eustasy on continental flooding in the late Paleozoic, Tectonophysics, v. 761, p. 108–121, https://doi.org/https://doi.org/10.1016/j.tecto.2019.04.018.
- Carlson, W. D., Donelick, R. A., & Ketcham, R. A., 1999, Variability of apatite fission-track annealing kinetics: I. Experimental results, American Mineralogist, v. 84, n. 9, p. 1213–1223, https://doi.org/10.2138/am-1999-0901.
- Carpéna, J., & Lacout, J.-L., 2010, Thermal annealing of fission tracks in synthetic apatites, Nuclear Instruments and Methods in Physics Research Section B: Beam Interactions with Materials and Atoms, v. 268, n. 19, p. 3191–3194,

- https://doi.org/10.1016/j.nimb.2010.05.085.
- Carter, A., & Gallagher, K., 2004, Characterizing the significance of provenance on the inference of thermal history models from apatite fission-track data A synthetic data study, Special Paper of the Geological Society of America, v. 378, n. 1, p. 7–23, https://doi.org/10.1130/0-8137-2378-7.7.
- Catacosinos, P. A., Daniels Jr., P. A., & Harrison III, W. B., 1990, Structure, Stratigraphy, and Petroleum Geology of the Michigan Basin, In M. W. Leighton, D. R. Kolata, D. F. Oltz, & J. J. Eidel (Eds.) Interior Cratonic Basins, v. 51, p. 561–601. American Association of Petroleum Geologists, https://doi.org/10.1306/M51530C31.
- Chayes, F., 1949, On Ratio Correlation in Petrography, The Journal of Geology, v. 57, n. 3, p. 239–254, https://doi.org/10.1086/625606.
- Chew, D. M., & Donelick, R. A., 2012, Combined apatite fission track and U-Pb dating by LA-ICP-MS and its application in apatite provenance analysis, In P. Sylvester (Ed.) Quantitative mineralogy and microanalysis of sediments and sedimentary rocks, v. 42, p. 219–248. Mineralogical Association of Canada.
- Cogné, N., Chew, D. M., Donelick, R. A., & Ansberque, C., 2020, LA-ICP-MS apatite fission track dating: A practical zeta-based approach, Chemical Geology, v. 531, p. 119302, https://doi.org/10.1016/j.chemgeo.2019.119302.
- Cogné, N., & Gallagher, K., 2021, Some comments on the effect of uranium zonation on fission track dating by LA-ICP-MS, Chemical Geology, v. 573, p. 120226, https://doi.org/10.1016/j.chemgeo.2021.120226.
- Crowley, K. D., 1985, Thermal significance of fission-track length distributions, Nuclear Tracks and Radiation Measurements (1982), v. 10, n. 3, p. 311–322, https://doi.org/10.1016/0735-245X(85)90120-6.
- Crowley, K. D., 1991, Thermal history of Michigan Basin and Southern Canadian Shield from apatite fission track analysis, Journal of Geophysical Research, v. 96, n. B1, p. 697–711, https://doi.org/10.1029/90JB02174.
- Crowley, K. D., Ahern, J. L., & Naeser, C. W., 1985, Origin and epeirogenic history of the Williston Basin: Evidence from fission- track analysis of apatite, Geology, v. 13, n. 9, p.

- 620, https://doi.org/10.1130/0091-7613(1985)13<620:OAEHOT>2.0.CO;2.
- Crowley, K. D., & Kuhlman, S. L., 1988, Apatite thermochronometry of Western Canadian Shield: Implications for origin of the Williston Basin, Geophysical Research Letters, v. 15, n. 3, p. 221–224, https://doi.org/10.1029/GL015i003p00221.
- Crowley, K. D., Naeser, C. W., & Babel, C. A., 1986, Tectonic significance of precambrian apatite fission-track ages from the midcontinent United States, Earth and Planetary Science Letters, v. 79, n. 3-4, p. 329–336, https://doi.org/10.1016/0012-821X(86)90189-5.
- DeConto, R. M., Pollard, D., Wilson, P. A., Pälike, H., Lear, C. H., & Pagani, M., 2008, Thresholds for Cenozoic bipolar glaciation, Nature, v. 455, n. 7213, p. 652–656, https://doi.org/10.1038/nature07337.
- Domeier, M., & Torsvik, T. H., 2014, Plate tectonics in the late Paleozoic, Di xue qian yuan., v. 5, n. 3, p. 303–350, https://doi.org/10.1016/j.gsf.2014.01.002.
- Donelick, A. J., Donelick, R. A., & Soares, C. J., 2023, Machine Learning-based AFT Annealing Parameter rmr0 from c-axis- projected Reduced Mean Length of Partially Annealed 252 Cf-derived FTs and LA-ICP-MS-derived Chemical Composition Data.
- Donelick, R. A., 2005, Apatite Fission-Track Analysis, Reviews in Mineralogy and Geochemistry, v. 58, n. 1, p. 49–94, https://doi.org/10.2138/rmg.2005.58.3.
- Donelick, R. A., Ketcham, R. A., & Carlson, W. D., 1999, Variability of apatite fission-track annealing kinetics; II, Crystallographic orientation effects, American Mineralogist, v. 84, n. 9, p. 1224–1234, https://doi.org/10.2138/am-1999-0902.
- Duddy, I. R., Green, P. F., & Laslett, G. M., 1988, Thermal annealing of fission tracks in apatite 3. Variable temperature behaviour, Chemical Geology: Isotope Geoscience Section, v. 73, n. 1, p. 25–38, https://doi.org/10.1016/0168-9622(88)90019-X.
- Eldrett, J. S., Harding, I. C., Wilson, P. A., Butler, E., & Roberts, A. P., 2007, Continental ice in Greenland during the Eocene and Oligocene, Nature, v. 446, n. 7132, p. 176–179, https://doi.org/10.1038/nature05591.
- Feinstein, S., Kohn, B., Osadetz, K., Everitt, R., & O'Sullivan, P., 2009, Variable Phanerozoic thermal history in the Southern Canadian Shield: Evidence from an apatite
- Non-peer reviewed preprint submitted to EarthArXiv. Under review with American Journal of Science.

- fission track profile at the Underground Research Laboratory (URL), Manitoba, Tectonophysics, v. 475, n. 1, p. 190–199, https://doi.org/10.1016/j.tecto.2009.01.016.
- Fleischer, R. L., Price, P. B., & Walker, R. M., 1965, Effects of temperature, pressure, and ionization of the formation and stability of fission tracks in minerals and glasses, Journal of Geophysical Research, v. 70, n. 6, p. 1497–1502, https://doi.org/10.1029/jz070i006p01497.
- Flowers, R., & Peak, B. A., 2025, Context matters: Modeling thermochronologic data in geologic frameworks using the Great Unconformity as a case study, Earth and Planetary Science Letters, v. 650, p. 119061, https://doi.org/10.1016/j.epsl.2024.119061.
- Flowers, R. M., Ault, A. K., Kelley, S. A., Zhang, N., & Zhong, S., 2012, Epeirogeny or eustasy? Paleozoic-Mesozoic vertical motion of the North American continental interior from thermochronometry and implications for mantle dynamics, Earth and Planetary Science Letters, v. 317, p. 436–445, https://doi.org/10.1016/j.epsl.2011.11.015.
- Flowers, R. M., Ketcham, R. A., Macdonald, F. A., Siddoway, C. S., & Havranek, R. E., 2022, Existing thermochronologic data do not constrain Snowball glacial erosion below the Great Unconformities, Proceedings of the National Academy of Sciences, v. 119, n. 38, p. e2208451119, https://doi.org/10.1073/pnas.2208451119.
- Fox, M., & Carter, A., 2020, Heated Topics in Thermochronology and Paths towards Resolution, Geosciences, v. 10, n. 9, p. 375, https://doi.org/10.3390/geosciences10090375.
- Fraser, J. A., Donaldson, J. A., Fahrig, W. F., & Tremblay, L. P., 1970, Helikian basins and geosynclines of the northwestern Canadian Shield, In A. J. Baer (Ed.) Symposium on basins and geosynclines of the Canadian Shield, v. 70, p. 213–238. Ottawa, Ontario: Geological Survey of Canada, Paper 70-40.
- Galbraith, R., & Green, P., 1990, Estimating the component ages in a finite mixture, International Journal of Radiation Applications and Instrumentation. Part D. Nuclear Tracks and Radiation Measurements, v. 17, n. 3, p. 197–206, https://doi.org/10.1016/1359-0189(90)90035-V.
- Galbraith, R. F., 1990, The radial plot: Graphical assessment of spread in ages, International

- Journal of Radiation Applications and Instrumentation. Part D. Nuclear Tracks and Radiation Measurements, v. 17, n. 3, p. 207–214, https://doi.org/10.1016/1359-0189(90)90036-W.
- Galbraith, R. F., 2005, Statistics for Fission Track Analysis, New York, NY: Chapman and Hall/CRC, https://doi.org/10.1201/9781420034929.
- Galbraith, R. F., & Laslett, G. M., 1993, Statistical models for mixed fission track ages, International Journal of Radiation Applications and Instrumentation. Part, v. 21, n. 4, p. 459–470, https://doi.org/10.1016/1359-0189(93)90185-C.
- Gallagher, K., 2012, Transdimensional inverse thermal history modeling for quantitative thermochronology, Journal of Geophysical Research: Solid Earth, v. 117, n. B2, https://doi.org/10.1029/2011JB008825.
- Gallagher, K., 2016, Comment on 'A reporting protocol for thermochronologic modeling illustrated with data from the Grand Canyon' by Flowers, Farley and Ketcham, Earth and Planetary Science Letters, v. 441, p. 211–212, https://doi.org/10.1016/j.epsl.2016.02.021.
- Gallagher, K., 2021, Comment on "Discussion: Extracting thermal history from low temperature thermochronology/A comment on the recent exchanges between Vermeesch and Tian and Gallagher and Ketcham", by Paul Green and Ian Duddy, Earth Science Reviews, https://doi.org/10.1016/j, Earth-Science Reviews, v. 216, p. 103549, https://doi.org/10.1016/j.earscirev.2021.103549.
- Gallagher, K., & Ketcham, R. A., 2018, Comment on "Thermal history modelling: HeFTy vs. QTQt" by Ver- meesch and Tian, Earth-Science Reviews (2014), 139, 279–290, Earth-Science Reviews, v. 176, p. 387–394, https://doi.org/10.1016/j.earscirev.2017.11.001.
- Gallagher, K., & Ketcham, R. A., 2020, Comment on the reply to the Comment on "Thermal history modelling: HeFTy vs. QTQt" by Vermeesch and Tian, Earth-Science Reviews (2014), 139, 279–290, Earth-Science Reviews, v. 203, p. 102878, https://doi.org/10.1016/j.earscirev.2019.102878.
- Galloway, J. M., Armstrong, D., & Lavoie, D., 2012, Palynology of the INCO Winisk #49204 core (54°18'30"N, 87°02'30"W, NTS 43L/6), Ontario, Geological Survey of

- Canada, Open File 7065, v., p. 1–51, https://doi.org/10.4095/290985.
- Gleadow, A. J., & Duddy, I. R., 1981, A natural long-term track annealing experiment for apatite, Nuclear Tracks, v. 5, n. 1-2, p. 169–174, https://doi.org/10.1016/0191-278X(81)90039-1.
- Gleadow, A. J., Duddy, I. R., Green, P. F., & Hegarty, K. A., 1986a, Fission track lengths in the apatite annealing zone and the interpretation of mixed ages, Earth and Planetary Science Letters, v. 78, n. 2-3, p. 245–254, https://doi.org/10.1016/0012-821X(86)90065-8.
- Gleadow, A. J. W., Duddy, I. R., Green, P. F., & Lovering, J. F., 1986b, Confined fission track lengths in apatite: a diagnostic tool for thermal history analysis, Contributions to Mineralogy and Petrology, v. 94, n. 4, p. 405–415, https://doi.org/10.1007/BF00376334.
- Gradstein, F. M., Ogg, J. G., Schmitz, M. D., & Ogg, G. M. (Eds.), 2020, Geologic Time Scale 2020, Elsevier, https://doi.org/10.1016/c2020-1-02369-3.
- Green, P., & Duddy, I., 2021, Discussion: Extracting thermal history from low temperature thermochronology. A comment on recent exchanges between Vermeesch and Tian and Gallagher and Ketcham, Earth-Science Reviews, v. 216, p. 103197, https://doi.org/10.1016/j.earscirev.2020.103197.
- Green, P., Duddy, I., Gleadow, A., Tingate, P., & Laslett, G., 1985, Fission-track annealing in apatite: Track length measure- ments and the form of the Arrhenius plot, Nuclear Tracks and Radiation Measurements (1982), v. 10, n. 3, p. 323–328, https://doi.org/10.1016/0735-245X(85)90121-8.
- Green, P., Duddy, I., Gleadow, A., Tingate, P., & Laslett, G., 1986, Thermal annealing of fission tracks in apatite, Chemical Geology: Isotope Geoscience section, v. 59, n. C, p. 237–253, https://doi.org/10.1016/0168-9622(86)90074-6.
- Green, P. F., 1981, A new look at statistics in fission-track dating, Nuclear tracks, v. 5, n. 1-2, p. 77–86, https://doi.org/10.1016/0191-278X(81)90029-9.
- Green, P. F., Japsen, P., Bonow, J. M., Chalmers, J. A., & Duddy, I. R., 2020, Thermal history solutions from thermochronol- ogy must be governed by geological relationships: A comment on Jess et al. (2019), Geomorphology, v. 360, p. 106848,

- https://doi.org/10.1016/j.geomorph.2019.106848.
- Haq, B. U., & Schutter, S. R., 2008, A Chronology of Paleozoic Sea-Level Changes, Science, v. 322, n. 5898, p. 64–68, https://doi.org/10.1126/science.1161648.
- Härtel, B., Jonckheere, R., Krause, J., & Ratschbacher, L., 2022, Spurious age-eU associations in thermochronological data, Earth and Planetary Science Letters, v. 599, p. 117870, https://doi.org/10.1016/j.epsl.2022.117870.
- Härtel, B., Vermeesch, P., Enkelmann, E., & Glorie, S., 2024, Ghost age components in detrital thermochronology, Chemical Geology, v. 670, p. 122406, https://doi.org/10.1016/j.chemgeo.2024.122406.
- Hendriks, B. W., & Redfield, T. F., 2005, Apatite fission track and (U-Th)/He data from Fennoscandia: An example of underestimation of fission track annealing in apatite, Earth and Planetary Science Letters, v. 236, n. 1-2, p. 443–458, https://doi.org/10.1016/j.epsl.2005.05.027.
- Hoffman, P. F., 1988, United Plates of America, The Birth of a Craton: Early Proterozoic Assembly and Growth of Laurentia, Annual Review of Earth and Planetary Sciences, v. 16, n. 1, p. 543–603, https://doi.org/10.1146/annurev.ea.16.050188.002551.
- Hoffman, P. F., 1989, Precambrian geology and tectonic history of North America, In A. W. Bally, & A. R. Palmer (Eds.) The Geology of North America—An Overview, v. A, chap. 16, p. 447–512. Geological Society of America, https://doi.org/10.1130/DNAG-GNA-A.447.
- Huber, P. J., 1973, Robust regression: asymptotics, conjectures and Monte Carlo, The Annals of Statistics, v. 1, p. 799–821, https://doi.org/10.1214/aos/1176342503.
- Hyeong, K., Lee, J., Seo, I., Lee, M. J., Yoo, C. M., & Khim, B. K., 2014, Southward shift of the Intertropical Conver- gence Zone due to Northern Hemisphere cooling at the Oligocene-Miocene boundary, Geology, v. 42, n. 8, p. 667–670, https://doi.org/10.1130/G35664.1.
- Issler, D. R., 1996, An inverse model for extracting thermal histories from apatite fission track data: instructions and software for the Windows 95 environment, Tech. rep., Geological Survey of Canada, Open File Report 2325, https://doi.org/10.4095/208313.

- Issler, D. R., McDannell, K. T., O'Sullivan, P. B., & Lane, L. S., 2022, Simulating sedimentary burial cycles Part 2: Elemental- based multikinetic apatite fission-track interpretation and modelling techniques illustrated using examples from northern Yukon, Geochronology, v. 4, n. 1, p. 373–397, https://doi.org/10.5194/gchron-4-373-2022.
- Jess, S., Stephenson, R., Roberts, D. H., & Brown, R., 2019, Differential erosion of a Mesozoic rift flank: Es- tablishing the source of topography across Karrat, central West Greenland, Geomorphology, v. 334, p. 138–150, https://doi.org/10.1016/j.geomorph.2019.02.026.
- Ji, M., Gao, X.-Y., Tu, C., & Chen, X.-J., 2025, Apatite composition and phase equilibrium modelling unravel F and Cl behavior during crustal anatexis in the Himalayan orogen, Chemical Geology, v., p. 122978, https://doi.org/10.1016/j.chemgeo.2025.122978.
- Judd, E. J., Tierney, J. E., Lunt, D. J., Montañez, I. P., Huber, B. T., Wing, S. L., & Valdes,
 P. J., 2024, A 485-million-year history of Earth 's surface temperature, Science, v. 385,
 n. 6715, p. eadk3705, https://doi.org/10.1126/science.adk3705.
- Kellett, D. A., Pehrsson, S., Skipton, D. R., Regis, D., Camacho, A., Schneider, D. A., & Berman, R., 2020, Thermochronological history of the Northern Canadian Shield, Precambrian Research, v. 342, https://doi.org/10.1016/j.precamres.2020.105703.
- Ketcham, R. A., 2005, Forward and Inverse Modeling of Low-Temperature Thermochronometry Data, Reviews in Mineralogy and Geochemistry, v. 58, n. 1, p. 275–314, https://doi.org/10.2138/rmg.2005.58.11.
- Ketcham, R. A., 2015, Technical Note: Calculation of stoichiometry from EMP data for apatite and other phases with mixing on monovalent anion sites, American Mineralogist, v. 100, n. 7, p. 1620–1623, https://doi.org/10.2138/am-2015-5171.
- Ketcham, R. A., 2019, Fission-Track Annealing: From Geologic Observations to Thermal History Modeling, In M. G. Malusá, & P. G. Fitzgerald (Eds.) Fission-Track Thermochronology and its Application to Geology, chap. 3, p. 49–75. Springer, Cham., https://doi.org/10.1007/978-3-319-89421-8 3.
- Ketcham, R. A., Carter, A., Donelick, R. A., Barbarand, J., & Hurford, A. J., 2007, Improved modeling of fission-track annealing in apatite, American Mineralogist, v. 92, n. 5-6, p. 799–810, https://doi.org/10.2138/am.2007.2281.

- Ketcham, R. A., Donelick, R. A., Balestrieri, M. L., & Zattin, M., 2009, Reproducibility of apatite fission-track length data and thermal history reconstruction, Earth and Planetary Science Letters, v. 284, n. 3-4, p. 504–515, https://doi.org/10.1016/j.epsl.2009.05.015.
- Ketcham, R. A., Donelick, R. A., & Carlson, W. D., 1999, Variability of apatite fission-track annealing kinetics: III. Extrapolation to geological time scales, American Mineralogist, v. 84, n. 9, p. 1235–1255, https://doi.org/10.2138/am-1999-0903.
- Ketcham, R. A., van der Beek, P., Barbarand, J., Bernet, M., & Gautheron, C., 2018, Reproducibility of Thermal History Reconstruction From Apatite Fission-Track and (U-Th)/He Data, Geochemistry, Geophysics, Geosystems, v. 19, n. 8, p. 2411–2436, https://doi.org/10.1029/2018GC007555.
- Kohn, B., & Gleadow, A., 2019, Application of Low-Temperature Thermochronology to Craton Evolution, In M. G. Malusá, &
 - P. G. Fitzgerald (Eds.) Fission-Track Thermochronology and its Application to Geology, chap. 21, p. 373–393. Springer, Cham., https://doi.org/10.1007/978-3-319-89421-8_21.
- Kohn, B. P., Gleadow, A. J., Brown, R. W., Gallagher, K., O'Sullivan, P. B., & Foster, D. A., 2002, Shaping the Australian crust over the last 300 million years: Insights from fission track thermotectonic imaging and denudation studies of key terranes, Australian Journal of Earth Sciences, v. 49, n. 4, p. 697–717, https://doi.org/10.1046/j.1440-0952.2002.00942.x.
- Kohn, B. P., Gleadow, A. J. W., Brown, R. W., Gallagher, K., Lorencak, M., & Noble, W. P., 2005, Visualizing thermotectonic and denudation histories using apatite fission track thermochronology, In P. W. Reiners, & T. A. Ehlers (Eds.) Reviews in Mineralogy and Geochemistry, v. 58, p. 527–565. Mineralogical Society of America and Geochemical Society, Washington, DC, United States (USA), https://doi.org/10.2138/rmg.2005.58.20.
- Kohn, B. P., Ketcham, R. A., Vermeesch, P., Boone, S. C., Hasebe, N., Chew, D., Bernet, M., Chung, L., Danišík, M., Gleadow,
 - A. J. W., & Sobel, E. R., 2024, Interpreting and reporting fission-track chronological data, GSA Bulletin, v. 136, n. 9-10, p. 3891–3920, https://doi.org/10.1130/B37245.1.
- Kohn, B. P., Osadetz, K. G., & Bezys, R. K., 1995, Apatite fission-track dating of two crater structures in the Canadian Williston Basin, Bulletin of Canadian Petroleum

- Geology, v. 43, n. 1, p. 54–64, https://doi.org/10.35767/gscpgbull.43.1.054.
- Kolawole, F., & Evenick, J. C., 2023, Global distribution of geothermal gradients in sedimentary basins, Geoscience Frontiers, v. 14,
 - n. 6, p. 101685, https://doi.org/10.1016/j.gsf.2023.101685.
- Kong, J. M., Boucher, D. R., & Smith, B. H. S., 1999, Exploration and geology of the Attawapiskat kimberlites, James Bay lowland, northern Ontario, Canada, In J. J. Gurney, J. L. Gurney, M. D. Pascoe, & S. H. Richardson (Eds.) 7th International Kimberlite Conference, p. 452–467. Cape Town, South Africa.
- Laslett, G. M., Green, P. F., Duddy, I. R., & Gleadow, A. J., 1987, Thermal annealing of fission tracks in apatite 2. A quantitative analysis, Chemical Geology: Isotope Geoscience Section, v. 65, n. 1, p. 1–13, https://doi.org/10.1016/0168-9622(87)90057-1.
- Laslett, G. M., Kendall, W. S., Gleadow, A. J., & Duddy, I. R., 1982, Bias in measurement of fission-track length distributions, Nuclear Tracks and Radiation Measurements (1982), v. 6, n. 2-3, p. 79–85, https://doi.org/10.1016/0735-245X(82)90031-X.
- Lavoie, D., Pinet, N., Dietrich, J., & Chen, Z., 2015, The Paleozoic Hudson Bay Basin in northern Canada: New insights into hydro- carbon potential of a frontier intracratonic Basin, AAPG Bulletin, v. 99, n. 5, p. 859–888, https://doi.org/10.1306/12161414060.
- Lavoie, D., Pinet, N., Dietrich, J., Zhang, S., Hu, K., Asselin, E., Chen, Z., Bertrand, R., Galloway, J., Decker, V., Budkewitsch, P., Armstrong, D., Nicolas, M., Reyes, J., Kohn, B. P., Duchesne, M., J, Brake, V., Keating, P., Craven, J., & Roberts, B., 2013, Geological framework, basin evolution, hydrocarbon system data and conceptual hydrocarbon plays for the Hudson Bay and Foxe basins, Canadian Arctic, Tech. rep., Geological Survey of Canada, https://doi.org/10.4095/293119.
- Lavoie, D., Pinet, N., Zhang, S., Reyes, J., Jiang, C., Ardakani, O., H, Savard, M. M., Dhillon, R. S., Chen, Z., Dietrich, J. R., Hu,
 - K., Craven, J., A, Roberts, B., Duchesne, M. J., Brake, V. I., Huot-Vézina, G., Galloway, J., M, McCracken, A. D., Asselin, E., Decker, V., Beauchemin, M., Nicolas, M. P. B., Armstrong, D. K., & Hahn, K. E., 2019, Hudson Bay, Hudson Strait, Moose River, and Foxe basins: synthesis of the research activities under the Geomapping for Energy and

- Minerals (GEM) programs 2008-2018, Tech. rep., Geological Survey of Canada, Open File 8507, https://doi.org/10.4095/314653.
- LeFever, R. D., 1996, Sedimentology and Stratigraphy of the Deadwood-Winnipeg Interval (Cambro-Ordovician), Williston Basin, In M. Longman, & M. Sonnenfeld (Eds.) Paleozoic Systems of the Rocky Mountain Region, p. 11–28. Rocky Mountain Section, Society for Sedimentary Geology.
- Li, W., Cheng, Y., Feng, L., Niu, J., Liu, Y., Skuratov, V. A., Zdorovets, M. V., Boatner, L. A., & Ewing, R. C., 2021, Alpha-decay induced shortening of fission tracks simulated by in situ ion irradiation, Geochimica et Cosmochimica Acta, v. 299, p. 1–14, https://doi.org/10.1016/j.gca.2021.01.022.
- Li, W., Shen, Y., Zhou, Y., Nan, S., Chen, C.-H., & Ewing, R. C., 2017, In situ TEM observation of alpha-particle induced annealing of radiation damage in Durango apatite, Scientific reports, v. 7, n. 1, p. 14108, https://doi.org/10.1038/s41598-017-14379-9.
- Lorencak, M., Kohn, B., Osadetz, K., & Gleadow, A., 2004, Combined apatite fission track and (U–Th)/He thermochronometry in a slowly cooled terrane: results from a 3440-m-deep drill hole in the southern Canadian Shield, Earth and Planetary Science Letters, v. 227, n. 1-2, p. 87–104, https://doi.org/10.1016/j.epsl.2004.08.015.
- McDannell, K. T., 2020, Notes on statistical age dispersion in fission-track datasets: the chi-square test, annealing variability, and analytical considerations, EarthArXiv, v., p. 1–4, https://doi.org/10.31223/OSF.IO/UJ4HX.
- McDannell, K. T., & Flowers, R. M., 2020, Vestiges of the ancient: Deep-time noble gas thermochronology, Elements, v. 16, n. 5, p. 325–330, https://doi.org/10.2138/GSELEMENTS.16.5.325.
- McDannell, K. T., & Issler, D. R., 2021, Simulating sedimentary burial cycles Part 1: Investigating the role of apatite fission track annealing kinetics using synthetic data, Geochronology, v. 3, n. 1, p. 321–335, https://doi.org/10.5194/gchron-3-321-2021.
- McDannell, K. T., Issler, D. R., & O'Sullivan, P. B., 2019a, Radiation-enhanced fission track annealing revisited and consequences for apatite thermochronometry, Geochimica et Cosmochimica Acta, v. 252, p. 213–239, https://doi.org/10.1016/j.gca.2019.03.006.

- McDannell, K. T., & Keller, C. B., 2022, Cryogenian glacial erosion of the central Canadian Shield: The "late" Great Unconformity on thin ice, Geology, v. 50, n. 12, p. 1336–1340, https://doi.org/10.1130/G50315.1.
- McDannell, K. T., Keller, C. B., Guenthner, W. R., Zeitler, P. K., & Shuster, D. L., 2022a, Reply to Flowers et al.: Existing thermochronologic data constrain Snowball glacial erosion below the Great Unconformity, Proceedings of the National Academy of Sciences, v. 119, n. 38, p. e2209946119, https://doi.org/10.1073/pnas.2209946119.
- McDannell, K. T., Keller, C. B., Guenthner, W. R., Zeitler, P. K., & Shuster, D. L., 2022b, Thermochronologic constraints on the origin of the Great Unconformity, Proceedings of the National Academy of Sciences, v. 119, n. 5, p. e2118682119, https://doi.org/10.1073/pnas.2118682119.
- McDannell, K. T., Pinet, N., & Issler, D. R., 2022c, Exhuming the Canadian Shield: preliminary interpretations from low-temperature thermochronology and significance for the sedimentary succession of the Hudson Bay Basin, In D. Lavoie, & K. Dewing (Eds.) Sedimentary basins of northern Canada: contributions to a 1000 Ma geological journey and insight on resource potential, chap. 10, p. 287–322. Natural Resources Canada, https://doi.org/10.4095/326100.
- McDannell, K. T., Schneider, D. A., Zeitler, P. K., O'Sullivan, P. B., & Issler, D. R., 2019b, Reconstructing deep-time histories from integrated thermochronology: An example from southern Baffin Island, Canada, Terra Nova, v. 31, n. 3, p. 189–204, https://doi.org/10.1111/ter.12386.
- McDowell, F. W., McIntosh, W. C., & Farley, K. A., 2005, A precise 40Ar-39Ar reference age for the Durango apatite (U-Th)/He and fission-track dating standard, Chemical Geology, v. 214, n. 3-4, p. 249–263, https://doi.org/10.1016/j.chemgeo.2004.10.002.
- Metsaranta, R. T., & Houlé, M. G., 2017, Precambrian geology, McFaulds Lake area, "Ring of Fire" region, Ontario, central sheet, Geological Survey of Canada, Open File 8201, scale 1:100,000, v. P.3805, https://doi.org/10.4095/299711.
- Montañez, I. P., & Poulsen, C. J., 2013, The Late Paleozoic Ice Age: An Evolving Paradigm, Annual review of earth and planetary sciences, v. 41, n. 1, p. 629–656,

- https://doi.org/10.1146/annurev.earth.031208.100118.
- Müller, R. D., Sdrolias, M., Gaina, C., Steinberger, B., & Heine, C., 2008, Long-Term Sea-Level Fluctuations Driven by Ocean Basin Dynamics, Science, v. 319, n. 5868, p. 1357–1362, https://doi.org/10.1126/science.1151540.
- Naeser, C. W., & Crowley, K. D., 1990, Fission-track dating of apatite from deep borehole ATK-1 at Atikokan, Ontario, In Z. E. Peterman, & D. C. Kamineni (Eds.) Isotopic studies of the Eye-Dashwa Lakes Pluton and the long-term integrity of whole-rock and mineral systems, p. 57–64. Pinawa, Manitoba: Atomic Energy of Canada Limited.
- Nelson, S. J., 1963, Ordovician paleontology of the northern Hudson Bay lowland, Memoir of the Geological Society of America, v. 90, n. 1, p. 1–145, https://doi.org/10.1130/MEM90-p1.
- Norris, A., 1993, Hudson Platform Geology, In D. Stott, & J. Aitken (Eds.) Sedimentary Cover of the Craton in Canada, p. 653–700. The Geological Society of America, https://doi.org/10.1130/dnag-gna-d1.653.
- Norris, A. W., & Sanford, B. V., 1968, Paleozoic and Mesozoic Geology of the Hudson Bay Lowlands, Tech. rep., Geological Survey of Canada, Paper no. 68-53, Ottawa, Ontario, https://doi.org/10.4095/119794.
- Norris, G., 1977, Palynofloral evidence for terrestrial Middle Jurassic in the Moose River Basin, Ontario, Canadian Journal of Earth Sciences, v. 14, n. 2, p. 153–158, https://doi.org/10.1139/e77-018.
- Osadetz, K., Kohn, B., Feinstein, S., & O'Sullivan, P., 2002, Thermal history of Canadian Williston basin from apatite fission-track thermochronology—implications for petroleum systems and geodynamic history, Tectonophysics, v. 349, n. 1-4, p. 221–249, https://doi.org/10.1016/S0040-1951(02)00055-0.
- O'Sullivan, P., 2018, Statistical evaluation (and manipulation) of fission-track single-grain age data: an analyst's "unbiased" perspective, In 16th International Conference on Thermochronology, p. 1. Palais Salfeldt, Quedlinburg, Germany: Thermo2018.
- O'Sullivan, P. B., & Parrish, R. R., 1995, The importance of apatite composition and single-grain ages when interpreting fission track data from plutonic rocks: a case study from the

- Coast Ranges, British Columbia, Earth and Planetary Science Letters, v. 132, n. 1-4, p. 213–224, https://doi.org/10.1016/0012-821X(95)00058-K.
- Patchett, P. J., Embry, A. F., Ross, G. M., Beauchamp, B., Harrison, J. C., Mayr, U., Isachsen, C. E., Rosenberg, E. J., & Spence,
 - G. O., 2004, Sedimentary cover of the Canadian shield through mesozoic time reflected by Nd isotopic and geochemical results for the Sverdrup Basin, Arctic Canada, Journal of Geology, v. 112, n. 1, p. 39–57, https://doi.org/10.1086/379691.
- Percival, J. A., Skulski, T., Sanborn-Barrie, M., Stott, G. M., Leclair, A. D., Corkery, M. T., & Boily, M., 2012, Geology and Tectonic Evolution of the Superior Province, Canada, In J. A. Percival, F. A. Cook, & R. M. Clowes (Eds.) Tectonic Styles in Canada: The LITHOPROBE Perspective, v. 49, p. 321–378. Geological Association of Canada, Special Paper.
- Peters, S. E., 2006, Macrostratigraphy of North America, Journal of Geology, v. 114, n. 4, p. 391–412, https://doi.org/10.1086/504176.
- Peters, S. E., Husson, J. M., & Czaplewski, J., 2018, Macrostrat: A Platform for Geological Data Integration and Deep-Time Earth Crust Research, Geochemistry, Geophysics, Geosystems, v. 19, n. 4, p. 1393–1409, https://doi.org/10.1029/2018GC007467.
- Piccoli, P. M., & Candela, P. A., 2002, Apatite in igneous systems, Reviews in Mineralogy and Geochemistry, v. 48, n. 1, p. 255–292, https://doi.org/10.2138/rmg.2002.48.6.
- Pinet, N., Lavoie, D., Dietrich, J., Hu, K., & Keating, P., 2013, Architecture and subsidence history of the intracratonic Hudson Bay Basin, northern Canada, Earth-Science Reviews, v. 125, p. 1–23, https://doi.org/10.1016/j.earscirev.2013.05.010.
- Pinet, N., & McDannell, K. T., 2020, The ups and downs of the Canadian Shield: 3 additional apatite fission-track analyses from the Musselwhite, Roberto, Meadowbank and Raglan mines, Ontario, Quebec, and Nunavut, Geological Survey of Canada, Open File Report 8706, v., p. 1–51, https://doi.org/10.4095/321845.
- Powell, J. W., Schneider, D. A., & Issler, D. R., 2018, Application of multi-kinetic apatite fission track and (U-Th)/He thermochronol- ogy to source rock thermal history: a case

- study from the Mackenzie Plain, NWT, Canada, Basin Research, v. 30, p. 497–512, https://doi.org/10.1111/bre.12233.
- Price, W. L., 1977, A controlled random search procedure for global optimisation, The Computer Journal, v. 20, n. 4, p. 367–370, https://doi.org/10.1093/comjnl/20.4.367.
- Rahn, M., & Seward, D., 2000, How many track lengths do we need?, On Track, v. 10, p. 14–17.
- Rainbird, R. H., Stern, R. A., Rayner, N., & Jefferson, C. W., 2007, Age, provenance, and regional correlation of the Athabasca Group, Saskatchewan and Alberta, constrained by igneous and detrital zircon geochronology, Bulletin of the Geological Survey of Canada, v. 588, p. 193–209, https://doi.org/10.4095/223761.
- Ravenhurst, C. E., Roden-Tice, M. K., & Miller, D. S., 2003, Thermal annealing of fission tracks in fluorapatite, chlorapatite, manganoanapatite, and Durango apatite: Experimental results, Canadian Journal of Earth Sciences, v. 40, n. 7, p. 995–1007, https://doi.org/10.1139/e03-032.
- Rayner, N., 2010, Far North Geomapping Initiative: new U-Pb geochronological results from the Seal River region, northeastern Manitoba (parts of NTS 54L, M, 64I, P), In Report of Activities 2010, p. 23–35. Manitoba Innovation, Energy and Mines, Manitoba Geological Survey.
- Sage, R. P., 2000, Kimberlites of the Attawapiskat area, James Bay Lowlands, northern Ontario, Ontario Geological Survey, Open File Report, v. 6019, p. 1–341.
- Sanford, B., 1987, Paleozoic Geology of the Hudson Platform, In C. Beaumont, & A. Tankard (Eds.) Sedimentary Basins and Basin-Forming Mechanisms, v. Memoir 12, p. 483–505. Canadian Society of Petroleum Geologists.
- Sanford, B. V., & Grant, A. C., 1990, New findings relating to the stratigraphy and structure of the Hudson Platform, In Current Re- search Part D, Interior Plains and Arctic Canada, v. 90-1D, p. 17–30. Geological Survey of Canada, https://doi.org/10.4095/131335.
- Sanford, B. V., & Norris, A. W., 1973, The Hudson Platform, Canadian Society of Petroleum Geology Special Publications, v. Future Pet, p. 387–409.
- Sanford, B. V., Thompson, F. J., & McFall, G. H., 1985, Plate tectonics-a possible

- controlling mechanism in the devel- opment of hydrocarbon traps in southwestern Ontario., Bulletin of Canadian Petroleum Geology, v. 33, n. 1, p. 52–71, https://doi.org/10.35767/gscpgbull.33.1.052.
- Schneider, D. A., Heizler, M. T., Bickford, M. E., Wortman, G. L., Condie, K. C., & Perilli, S., 2007, Timing constraints of orogeny to cratonization: Thermochronology of the Paleoproterozoic Trans-Hudson orogen, Manitoba and Saskatchewan, Canada, Precambrian Research, v. 153, p. 65–95, https://doi.org/10.1016/j.precamres.2006.11.007.
- Seiler, C., Boone, S. C., Kohn, B. P., & Gleadow, A. J., 2023, A grain-by-grain comparison of apatite fission-track analysis by LA- ICP-MS and the External Detector Method, Chemical Geology, v. 635, p. 121623, https://doi.org/10.1016/j.chemgeo.2023.121623.
- Sloss, L. L., 1963, Sequences in the cratonic interior of North America, Geological Society of America Bulletin, v. 74, n. 2, p. 93–114, https://doi.org/10.1130/0016-7606(1963)74[93:SITCIO]2.0.CO;2.
- Smith, M. P., & Yardley, B. W., 1999, Fluid evolution during metamorphism of the Otago Schist, New Zealand: (II) Influence of detrital apatite on fluid salinity, Journal of Metamorphic Geology, v. 17, n. 2, p. 187–193, https://doi.org/10.1046/j.1525-1314.1999.00190.x.
- Sun, Q., Zhou, W.-X., & Fan, J., 2020, Adaptive Huber Regression, Journal of the American Statistical Association, v. 115, n. 529, p. 254–265, https://doi.org/10.1080/01621459.2018.1543124.
- Telford, P. G., & Long, D. G., 1986, Mesozoic Geology of the Hudson Platform, In Elsevier Oceanography Series, v. 44, chap. 3, p. 43–54. Elsevier, https://doi.org/10.1016/S0422-9894(08)70896-1.
- Tello, C. A., Palissari, R., Hadler, J. C., Iunes, P. J., Guedes, S., Curvo, E. A., & Paulo, S. R., 2006, Annealing experiments on induced fission tracks in apatite: Measurements of horizontal-confined track lengths and track densities in basal sections and randomly oriented grains, American Mineralogist, v. 91, n. 2-3, p. 252–260, https://doi.org/10.2138/am.2006.1269.

- Tillement, B. A., Peniguel, G., & Guillemin, J. P., 1976, Marine Pennsylvanian Rocks in Hudson Bay, Bulletin of Canadian Petroleum Geology, v. 24, n. 3, p. 418–439, https://doi.org/10.35767/gscpgbull.24.3.418.
- Trettin, H., 1975, Investigations of Lower Paleozoic geology, Foxe Basin, northeastern Melville Peninsula, and parts of northwestern and central Baffin Island, Geological Survey of Canada Bulletin, v. 251, p. 1–171.
- Tripati, A., & Darby, D., 2018, Evidence for ephemeral middle Eocene to early Oligocene Greenland glacial ice and pan-Arctic sea ice, Nature Communications, v. 9, p. 1038, https://doi.org/10.1038/s41467-018-03180-5.
- Vermeesch, P., 2012, On the visualisation of detrital age distributions, Chemical Geology, v. 312-313, p. 190–194, https://doi.org/10.1016/j.chemgeo.2012.04.021.
- Vermeesch, P., 2017, Statistics for LA-ICP-MS based fission track dating, Chemical Geology, v. 456, p. 19–27, https://doi.org/10.1016/j.chemgeo.2017.03.002.
- Vermeesch, P., 2018, IsoplotR: A free and open toolbox for geochronology, Geoscience Frontiers, v. 9, n. 5, p. 1479–1493, https://doi.org/10.1016/j.gsf.2018.04.001.
- Vermeesch, P., 2019, Statistics for Fission-Track Thermochronology, In M. G. Malusa, & P. Fitzgerald (Eds.) Fission-Track Thermochronology and its Application to Geology, chap. 6, p. 109–122. New York: Springer International Publishing, 1 ed., https://doi.org/10.1007/978-3-319-89421-8_6.
- Vermeesch, P., & Tian, Y., 2014, Thermal history modelling: HeFTy vs. QTQt, Earth-Science Reviews, v. 139, p. 279–290, https://doi.org/10.1016/j.earscirev.2014.09.010.
- Webb, K. J., Scott Smith, B. H., Paul, J. L., & Hetman, C. M., 2004, Geology of the Victor Kimberlite, Attawapiskat, Northern Ontario, Canada: cross-cutting and nested craters, Lithos, v. 76, n. 1-4, p. 29–50, https://doi.org/10.1016/j.lithos.2004.03.050.
- Weller, O. M., & St-Onge, M. R., 2017, Record of modern-style plate tectonics in the Palaeoproterozoic Trans-Hudson orogen, Nature Geoscience, v. 10, n. 4, p. 305–311, https://doi.org/10.1038/ngeo2904.
- Wheeler, J. O., Hoffman, P., Card, K. D., Davidson, A., Sanford, B. V., Okulitch, A. V., & Roest, W. R., 1996, Geological map of Canada, "A" Series Map 1860A, v. 3 sheets,

- p. scale 1:5,000,000, https://doi.org/10.4095/208175.
- White, T. S., Witzke, B. J., & Ludvigson, G. A., 2000, Evidence for an Albian Hudson arm connection between the Cretaceous Western Interior Seaway of North America and the Labrador Sea, Geological Society of America Bulletin, v. 112, n. 9, p. 1342–1355, https://doi.org/10.1130/0016-7606(2000)112<1342:EFAAHA>2.0.CO;2.
- Willett, S. D., 1997, Inverse modeling of annealing of fission tracks in apatite 1: A controlled random search method, American Journal of Science, v. 297, n. 10, p. 939–969, https://doi.org/10.2475/ajs.297.10.939.
- Williams, G., & Barrs, M., 1976, Palynological analysis of the interval 1130–1260 feet from Aquitaine et al., Narwhal O-58, Hudson Bay, Paleontological Report EPGS-PAL, v. 11-77GLW, p. 1–4.
- Zeng, X., Pastore, G., Shen, C., Resentini, A., Fu, H., Yang, C., Buret, Y., Vermeesch, P., & Malusà, M. G., 2025, Raman mapping reveals alpha radiation damage zonation and its annealing in Durango apatite, Earth and Planetary Science Letters, v. 671, p. 119636, https://doi.org/10.1016/J.EPSL.2025.119636.
- Zhang, S., & Riva, J. F., 2018, The stratigraphic position and the age of the Ordovician organic-rich intervals in the northern Hudson Bay, Hudson Strait, and Foxe basins—evidence from graptolites, Canadian Journal of Earth Sciences, v. 55, n. 8, p. 897–904, https://doi.org/10.1139/cjes-2017-0266.

Figure Captions

Fig. 1. A) Hypothetical thermal history scenarios and the corresponding c-axis projected track length distributions produced from each t-T path. Rapid cooling (blue dotted line), slow cooling (yellow long dash line), minor PAZ reheating (gray short dash line), and greater PAZ reheating (red solid line). B) unimodal long track lengths correspond to rapid cooling and subsequent stasis. C) unimodal right skew track length distribution typical of simple, slow cooling. D) unimodal track length distribution that has been shortened and broadened due to reheating to 65° C. E) bimodal track length distribution due to a history involving greater reheating to 85° C.

Fig. 2. Simplified geologic map of the central Canadian Shield near Hudson Bay, modified from Wheeler et al. (1996). New AFT sample locations are yellow points across the Hudson Platform. Light blue points (near sample 97-10-365) are multi-chronometer samples published in McDannell & Keller (2022). Precambrian rocks are undifferentiated except for those rocks of the *ca.* 2.0–1.8 Ga Trans-Hudson Orogen (THO). The *ca.* 1.7 Ga Athabasca Basin lies to the west of Hudson Bay. The Hudson Bay Basin Paleozoic section outcrops (blue) along the THO and the western Superior Province. Green diamond is the approximate location of the *ca.* 170 Ma Attawapiskat kimberlite field. MW denotes the location of the Musselwhite gold mine, those AFT data discussed in Pinet & McDannell (2020). INCO is the borehole discussed in Galloway et al. (2012); refer to the text for discussion. Inset map provides global reference.

Fig. 3. Geological cross-section across Hudson Bay Basin, modified from Norris (1993) and McDannell et al. (2022c). The Phanerozoic geology is simplified and grouped according to sequences in Sloss (1963). Red lines are intra-basin faults. Gray area in the inset outlines Paleozoic and younger rocks (refer to Pinet et al., 2013) and major regionally interpreted arch structures are shown as dashed blue lines (e.g., Sanford & Grant, 1990): Bell arch (BA); Cape Henrietta Maria arch or Transcontinental arch (CHMA); Fraserdale arch (FA); Keewatin arch (KA); Severn arch (SA; trending NW-SE). The dark red line A—A' in the cross-section extends from Southampton Island to the Moose River Basin and the points along the line correspond to drilled hydrocarbon exploration wells in the Hudson Bay Basin. The Comeault #1 well in Manitoba is the closest to our northerly samples that penetrates over 550 m of Silurian through Ordovician rocks and Precambrian basement at 616 m depth (third red point down from the north in the inset and the blue dot on the cross-section; Armstrong et al., 2018; Lavoie et al., 2019).

Fig. 4. Electron backscatter images of EPMA single-spot analyses for representative aliquot-2 apatite grains from the fission-track mounts. Intra-grain compositional heterogeneity is present but minor. Spot analyses were 5 μ m in diameter. Spot-A was

analyzed near the laser ablation spot and spot-B was randomly collected in another location. On average the eCl percent variation between spots is 100-150%. (A) The eCl values for sample 97-10-365 grain-age-10 (a2-10) are 0.008 apfu (spot A; $r_{mr0}=0.838$; equivalent $Dpar=1.78~\mu\text{m}$) and 0.000 apfu (spot B; $r_{mr0}=0.840$; e $Dpar=1.75~\mu\text{m}$). (B) The eCl values for sample CB99-227 grain-age-2 (a2-2) are 0.018 apfu (spot A; $r_{mr0}=0.834$; e $Dpar=1.81~\mu\text{m}$) and 0.025 apfu (spot B; $r_{mr0}=0.832$; e $Dpar=1.83~\mu\text{m}$). Spot-B is near the grain edge where there is a narrow band (10–15 μ m) of modest U zoning that is visible due to the lower spontaneous track density compared to the grain interior. (C) The eCl values for sample 12RM086 grain-age-1 (a2-1) are 0.006 apfu (spot A; $r_{mr0}=0.838$; e $Dpar=1.77~\mu\text{m}$) and 0.014 apfu (spot B; $r_{mr0}=0.835$; e $Dpar=1.80~\mu\text{m}$). The r_{mr0} values were calculated using the Carlson et al. (1999) equation.

Fig. 5. Radial plots and mixture modeling of AFT grain ages plotted with respect to kinetic parameter, effective Cl. Mixture model age peaks are represented by dashed lines and points are colored by eCl. Percentages are the proportion of grains in each mixture model peak age group. (A) Radial plot of AFT ages for sample 97-10-365 aliquot-2 grains. (B) Plot of AFT age with respect to eCl for EPMA spot-A (collected near the laser ablation spot) for 97-10-365. Data points are colored with respect to interpretations from the mixture modeling. Circles are colored according to younger population-1 data and squares correspond to older population-2 data. (C) Same plot as in panel B except both replicate EPMA analyses are considered (spots A and B) for each grain age. The minimum or maximum of the two EPMA spots was assigned based on the kinetic population that the age falls into (i.e., if in younger peak population-1, the minimum eCl value is assigned, and vice versa). Panels D–F descriptions are the same as above but are for sample CB99-227. Panels G–I are for sample 12RM086. Note: white points lack probe data.

Fig. 6. Fission-track correlations for single grains from samples 97-10-365 (A, B), CB99-227 (C, D), and 12RM086 (E, F) using the approach of Härtel et al. (2022) (equation 4). (A, C, E): AFT age versus U/Ca ratio. (B, D, F): Daughter-Parent (D-P) plots of N_S counts versus U/Ca shown with correlation coefficients (r), significance (p), and line equation.

Statistically significant correlation when p value is < 0.05. Robust linear regression using Huber loss minimization, which reduces the influence of outliers while preserving sensitivity to underlying linear trends. Uncertainties on the intercepts were estimated by nonparametric bootstrapping (n = 1000). All D-P plots show excess scatter and positive offset y-intercepts reported as \pm 1s. A Julia script for these calculations is available upon request.

Fig. 7. QT®t time-temperature models shown as path density heat maps resolved to a pixel size of 1 My and 1°C. Relative probability is proportional to path density, where brighter colors (or higher saturation) indicate more thermal histories pass through that region. Path density is approximately proportional to likelihood and the color scale is normalized path density (minimum value of 0 is equal to no paths, and a maximum value of 1 is equal to the upper 95th percentile of path density). (A–C) model results for sample 97-10-365. (D–F) model results for sample CB99-227. (G-I) model results for sample 12RM086. Geologic constraint boxes (white) represent Ordovician and Jurassic unconformities discussed in earlier sections. A notable result is that the general features of a two-peak thermal history are visible in the unconstrained models. The robust track length datasets are better explained by two heating events and the t-T solutions independently support the regional geologic record. The other models show step-wise addition of geologic constraints and further refinement of the solutions. QTQt general prior: 300 ± 300 Ma and 70 ± 70 °C, a modern surface temperature of 2.5 ± 2.5 °C, and a maximum allowed heating/cooling rate of 3 °C/My. Each panel shows 500,000 models accepted post burn-in (200,000 iteration burn-in). ML = Max. Likelihood model; MP = Max. Posterior model; MM = Max. Mode model; EX = Expected model. QTQt plotting script is available https://github.com/OpenThermochronology/QTQtPlot

Fig. 8. The QTQt model predictions compared to the observed central AFT ages and MTLs for each model shown in fig. 7. Each distribution represents the predictions from all 500,000 accepted posterior solutions. Gray lines are the mean and uncertainty for either age (2s) or MTL (1s).

Fig. 9. Conditional probabilities for the 'unconstrained' QTQt models from figure 7. Histories were filtered by imposing time- temperature conditions *a posteriori* (black dashed lines), such that only those histories that met the specified conditions—that the AFT samples cooled to near-surface temperatures (0–30°C) at 450 Ma and 170 Ma—were retained. All other QTQt model run options are the same as those discussed previously. Note that these are not new models, but are those shown in fig. 7; panels A, D, and G, respectively.

Fig. 10. AFTINV inverse model results for the Hudson Platform samples. Panels A, D, and G show ≥ 300 acceptable random Monte Carlo solutions ≥ 0.05 significance level (light gray t-T paths). Some 0.5 significance level solutions were randomly found during the initial Monte Carlo search (dark gray paths) and were retained in the 0.05 solution pool. The 0.05 random MC solution set for each AFT sample was then updated by the CRS algorithm to the 0.5 significance level. Panels B, E, and H show 300 acceptable solutions at the 0.5 significance level (dark gray t-T paths) obtained using the CRS algorithm. The exponential mean (exp mean; blue line) solution and the best-fit minimum objective function (min obj fn; green line) solution are also shown for the MC and CRS paths. Panels C, F, and I show the better 0.5 level fits to the track length distributions as a gray envelope for all solutions and the best fit and mean are highlighted in green and blue. The 0.5 level goodness-of-fit values for the track lengths are 0.98, 0.88, and 0.93 for samples 97-10-365, CB99-227, and 12RM086, respectively. Refer to table 2 for tabulated information on the GOFs for AFT age and length for each model. Figure 11 summarizes the thermal peak timing and magnitude for the 0.05 and 0.5 fit levels. Note that the time and magnitude of heating between the QTQt and AFTINV results are similar, yet the QTQt results more closely resemble the 0.05 solution set from AFTINV.

Fig. 11. Thermal episode summary for the AFTINV inverse thermal history models exhibiting two thermal peaks. Dotted line shows the minimum-maximum time range at the 0.05 significance level for each thermal peak for each sample. Thick transparent line represents the minimum-maximum time range at the 0.5 significance level. The vertical bar and opaque heavy lines show the mean \pm 2s time for each thermal peak at the 0.5 level.

Refer to table 2 for tabulated information.

Fig. 12. Conventional unprojected track length distributions for two AFT samples as histograms with 1 μ m bins. Track lengths are displayed as they were originally measured but were modeled using their corresponding c-axis angles. (A) all 709 track lengths combined from both sample aliquots of 97-10-365 with a conventional mean track length of 12.01 \pm 1.75 μ m and c-axis projected mean length of 13.63 \pm 1.02 μ m. (B) random 50% downsampling or resampling of the total number of lengths in panel A. (C) random 10% resampling of the total lengths in panel A. (D–F) Sample CB99-227; the same as panels A–C with a conventional mean track length of 11.81 \pm 1.67 μ m and c-axis projected mean length of 13.53 \pm 0.94 μ m. All resampled distributions in panels B–C and E–F are similar in form to the ones in A and D, respectively. MTL = mean track length.

Fig. 13. QTQt time-temperature simulations shown as path density heat maps. Panels A and D are the 'unconstrained' models without t–T constraint boxes shown in fig. 7. Models in the other panels are shown with a different color ramp to distinguish from those models. (A) model results for the total 97-10-365 length dataset (B) model results for the 50% (n = 364) randomly resampled track lengths and (C) 10% (n = 69) resampled tracks for sample 97-10-365. (D) model results for the total CB99-227 length data set. (E) model results for the 50% (n = 330) randomly resampled track lengths and (C) 10% (n = 67) resampled tracks for sample CB99-227. The two-peak history is not well resolved below \sim 250–300 track lengths (note: longer inversion burn-in may potentially help resolve the two thermal peaks (vs. more linear history) in panels B and E). The models in panels B, C, E, and F use the QTQt option to explicitly penalize more complex paths with equivalent likelihood (i.e., more complex models are rejected if the LL is similar to a simpler t–T path).

APPENDIX

Table 3. Apatite fission-track data for sample 97-10-365, Hearne Domain (lon/lat: -94.84072244, 59.0724352)

Part		1401	e 5. Apa					-10-50	<i>J</i> 5, 110		Oman	1 (1011/1	iai 5-	1.04072	.244, 39		<u> </u>	
1916-16 2778-07 9.88-03 8.66-07 7.46E-14 9.26 3.28 2.09 1.09 0.00 0.30 0.840 0.001	N_s		²³⁸ U/ ⁴³ Ca	1s	$P_i\Omega_i$	$\sigma P_i^2 \Omega_i^2$	AFT age†		D_{par}	F⋆						U-Pb‡	2s	aliquot
23 25 16 26 27 27 27 28 28 28 28 28		(cm ²)					(Ma)	(Ma)	(µm)	(apfu)	(apfu)	(apfu)	1999	(apfu)	(apfu)	age (Ma)	(Ma)	grain
23 25 16 26 27 27 27 28 28 28 28 28	97	2.91E-05	2.77E-02	9.38E-03	8.06E-07	7.46E-14	926	328	2.09	1.69	0.00	0.30	0.840	0.001	_	_	_	a1-1
1406 2,58E-06 1,49E-0 1,00E-06 1,0EE-06 1,0	73		3.01E-02					98	1.96	1.55	0.00	0.45	0.843	-0.007	_	-	_	a1-2
162 3.88E-0.5 7.08E-0.1 4.9F-0.1 2.75E-0.5 3.04E-1.4 470 48 1.83 1.52 0.00 0.47 0.48 0.008 - - - - 1.55 0.00 0.47 0.48 0.008 - - - 1.55 0.00 0.47 0.48 0.008 - - - 1.55 0.00 0.41 0.48 0.008 - - 1.55 0.00 0.41 0.48 0.008 - - 1.55 0.00 0.41 0.48 0.008 - - 1.55 0.00 0.41 0.48 0.008 - 1.55 0.00 0.41 0.48 0.008 - - 1.55 0.00 0.41 0.48 0.008 0	80		4.14E-02	3.23E-03	1.21E-06	8.83E-15	527	72	1.99	1.58	0.01	0.42	0.842	-0.005	_	_	_	a1-3
1	426	5.82E-05	1.49E-01	9.66E-03	8.65E-06	3.17E-13			1.71		0.01	0.40	0.838	0.005	-	_	-	a1-4
94 94 95 95 95 97 97 97 97 97															-	_	_	a1-5
44 245E-05 4 73E-02 145E-05 4 73E-02 145E-05 24E-05										1.59	0.00	0.41	0.840	0.002	_	2155	471	
126 3.46E-05 3.4										. –					-	-	-	
59 194E\circ\circ\circ\circ\circ\circ\circ\cir															-	-	-	
264 3.11E-05 1.85E-01 4.20E-03 5.73E-06 1.70E-14 370 25 1.97 1.62 0.11 0.31 0.814 0.071 - 2400 299 al.1 149 3.40E-05 3.04E-02 7.02E-04 1.04E-06 5.70E-15 10.5 115 43 1.75 1.02 0.01 0.37 0.842 - 0.005 - 2321 413 al.1 149 3.40E-05 3.04E-02 7.02E-04 1.04E-06 5.70E-15 10.87 1.02 1.02 1.02 1.02 1.02 1.02 1.02 1.02															-			
194 34.0F.05 34.0F.02 10.0F.05 2.00F.06 5.70F.16 10.0F.05 34.0F.05 30.0F.02 7.0F.06 5.70F.16 10.0F.05 34.0F.05 30.0F.02 7.0F.06 5.70F.16 10.0F.05 34.0F.05 34.0F																		
149 3.40E-05 3.60E-07 2.60E-06 1.00E-06 2.60E-16 1.00E-07 2.40E-16 3.40E-07 3.4																		
14																		
104 2.91E-05 5.28E-02 1.25E-03 1.82E-06 1.79E-15 466 47 1.93 1.65 0.00 0.05 0.845 0.014 - 2.885 402 4.11E-18 2.43E-05 5.28E-02 1.39E-03 1.29E-06 1.14E-15 715 70 2.04 1.60 0.00 0.04 0.844 -0.012 - 2.646 498 4.11E-15 1.05 0.															_			
124 3.88E-05 5.28E-02 1.20E-03 2.05E-06 2.17E-15 482 455 1.88 1.73 0.00 0.26 0.844 -0.012 - 2.646 0.984 a-1.71 0.00 3.466 a-1.71 0.00 3.466 a-1.71 0.00 0.26 0.844 -0.012 - 2.464 0.984 a-1.71 0.00 3.466 a-1.71 0.00 0.24 0.848 0.0017 - 2.464 0.0018 0.00															_			
181 2.43E-05 5.3EE-02 1.39E-08 1.29E-06 1.14E-15 715 70 2.04 1.60 0.00 0.40 0.844 0.012 - 2.0464 498 al-17 1.01 3.40E-05 3.65E-02 9.96E-04 1.34E-06 1.14E-15 595 62 1.82 1.62 0.01 0.37 0.846 0.017 - 2.256 460 al-17 1.01 3.40E-05 3.89E-02 1.40E-03 8.38E-07 3.60E-05 3.89E-02 1.40E-03 8.38E-07 3.60E-15 8.30E-05 3.89E-02 1.40E-03 8.38E-07 3.60E-15 8.30E-05 3.20E-05 3.20E-															_			
103 345E05 3,95E02 1,00E-03 8,86E-07 6,00E-16 595 595 50E 1,82 1,62 5,00 0,37 0,846 0,017 - 2107 477 al-18 54 2,91E-05 3,95E-02 1,44E-03 1,13E-05 1,75E-15 382 54 1,65 1,69 0,00 0,31 0,847 0,002 - 2256 460 al-18 50E															_			
101 3.40E.05 3.95E.02 9.96E.04 1.34E.06 1.14E.15 595 62 1.82 1.62 0.01 0.38 0.841 0.002 - 2.256 406 al-15 54 2.91E.05 3.89E.02 1.46E.05 3.89E.02 1.46E.05 3.89E.02 1.46E.05 3.89E.02 1.46E.05 3.89E.02 1.46E.05 8.83E.07 1.66E.15 8.90 96 2.14 1.65 0.01 0.35 0.840 0.000 - 2 - 3.12 3.45 4.37E.03 3.99E.03 6.08E.06 2.20E.14 455 28 2.03 1.76 0.00 0.24 0.848 0.023 - 2 - 3.12 3.45 4.37E.03 3.99E.03 6.08E.06 2.20E.14 455 28 2.03 1.76 0.00 0.24 0.848 0.003 - 2 - 3.12 3.45 4.37E.03 3.99E.03 4.89E.05 3.58E.05 3.58E.															_			a1-18
97 2.91E-05 3.03E-02 1.40E-03 8.38E-07 1.66E-15 8.90 96 2.14 1.65 0.01 0.35 0.840 0.000 al-2- 345 4.37E-05 1.39E-01 3.39E-03 6.06E-06 2.02E-14 455 28 2.03 1.76 0.00 0.24 0.848 0.023 al-2- 345 4.37E-05 1.39E-01 3.39E-03 1.70E-06 3.45E-15 558 48 1.75 1.57 0.00 0.43 0.844 0.010 al-2- 96 3.40E-05 5.00E-02 1.73E-03 1.70E-06 3.45E-15 558 48 1.75 1.57 0.00 0.43 0.844 0.010 al-2- 97 3.88E-05 5.00E-01 4.86E-03 2.02E-14 404 27 1.99 2.238 328 a2- 472 5.82E-05 7.83E-02 2.54E-03 4.56E-06 2.79E-14 804 47 1.86 1.55 0.00 0.45 0.83 0.006 0.006 2.205 518 a2- 473 5.82E-05 5.20E-02 9.38E-06 2.79E-14 804 47 1.86 1.55 0.00 0.45 0.83 0.006 0.006 2.205 518 a2- 474 5.82E-05 5.20E-02 9.38E-04 4.56E-06 2.79E-14 804 47 1.86 1.55 0.00 0.45 0.83 0.006 0.006 0.205 518 a2- 475 5.82E-05 5.80E-02 1.10E-03 3.00E-06 2.79E-14 804 48 1.75 1.57 0.00 0.45 0.83 0.006 0.006 0.006 0.205 518 a2- 486 5.82E-05 5.80E-02 1.10E-03 3.00E-06 2.79E-14 804 48 1.75 1.57 0.00 0.45 0.83 0.006 0.006 0.006 0.205 518 a2- 487 5.82E-05 5.80E-02 1.10E-03 3.00E-06 4.80E-15 779 49 1.79 1.52 0.01 0.471 0.441 0.000	101										0.01				_		460	a1-19
Section Sect		2.91E-05	3.89E-02	1.44E-03	1.13E-06	1.75E-15	382	54	1.65	1.69	0.00	0.31	0.847	-0.021	-	2497	596	a1-20
44 37EC 33BEC 33BEC 33BEC 32BEC 34BEC 52BE 48 1.75 1.75 0.00 0.24 0.848 -0.023 -	97		3.03E-02	1.40E-03	8.83E-07	1.66E-15			2.14		0.01	0.35	0.840	0.000	-	_	-	a1-21
64 485E-05 506E-02 1.49E-03 2.35E-06 5.25E-15 558 48 1.75 1.57 0.00 0.43 0.844 -0.010 2471 593 al-2- 293 3.88E-05 5.05E-01 4.43E-03 5.82E-06 5.29E-14 404 27 1.99 2.238 3.28 al-2- 2472 5.82E-05 7.85E-05		2.33E-05	2.66E-02		6.19E-07	8.73E-16									-	_	_	a1-22
99 3,40E.05 5,10E.02 1,73E.03 1,70E.06 3,45E.15 450 49 2.03 2471 593 a1.22 93 3,88E.05 1,50E.04 4,43E.03 5,82E.06 2,95E.14 404 27 1,99 238 8,328 a2.1 472 5,82E.05 7,83E.02 2,54E.03 4,56E.06 2,19E.14 508 44 7 1,86 1,55 0,00 0,45 0,838 0,006 0,006 205 518 a2.24 46 5,82E.05 1,20E.01 2,23E.02 9,33E.04 3,04E.06 2,95E.15 779 49 1,79 1,52 0,01 0,471 0,001 0,001 0,001 2,938 384 a2.4 25,82E.05 5,86E.02 1,15E.03 3,14E.06 4,84E.15 531 38 1,70 1,65 0,01 0,471 0,001 0,001 0,000 2,938 384 a2.4 274 2,91E.05 1,64E.01 3,12E.03 4,77E.06 8,24E.15 438 30 2,06 1,51 0,01 0,48 0,839 0,003 0,028 2,42 376 a2.6 274 2,91E.05 1,64E.01 3,12E.03 4,77E.06 8,24E.15 458 30 2,06 1,51 0,01 0,48 0,839 0,003 0,028 2,42 376 a2.6 274 4,64 8,5E.05 1,80E.01 2,99E.03 8,73E.06 2,10E.14 409 2,2 1,53 1,71 0,00 0,28 0,850 - 0,002 0,172 2,49 a2.8 255 4,85E.05 7,85E.02 1,42E.03 1,63E.06 2,33E.15 579 57 1,60 1,62 0,02 0,37 0,842 0,006 0,004 2,134 307 a2.9 255 4,85E.05 3,81E.02 1,42E.03 1,63E.06 2,15E.15 562 38 1,72 1,66 0,01 0,33 0,83R 0,008 0,000 2,075 297 a2.1 216 2,91E.05 1,59E.05 1,59E.05 3,08E.06 4,78E.16 2,58E.15 557 7 2,02 1,155 0,01 0,04 0,339 0,003 0,002 2,176 312 a2.1 216 2,91E.05 1,59E.05 1,59E.05 3,08E.06 4,72E.15 555 41 1,54 1,79 0,01 0,20 0,848 0,002 0,000 2,007 2,004 2,00															_	-	_	a1-23
293 3.88E-05 7.83F-02 4.48E-03 5.82E-06 2.95E-14 404 27 1.99 - <td></td> <td>0.43</td> <td>0.844</td> <td></td> <td>-</td> <td></td> <td></td> <td>a1-24</td>												0.43	0.844		-			a1-24
5.82E-05										-		-	-	-	-			
446 5.82E-05 5.22E-05 5.22E-05 5.23E-04 9.33E-04 0.40E-06 2.95E-15 779 49 1.79 1.52 0.01 0.471 0.841 0.002 0.000 2193 383 a2.3 4.5 8.5 8.5 8.5 8.5 8.5 8.5 8.5 8.5 8.5 8												0.45			- 0.006			
304 5.82E-05 5.82E-05 5.82E-06 5.82E-05 5.86E-05 2.96E-05 4.86E-05 2.86E-05 4.86E-05 2.86E-05 5.86E-03 5.86E-05 3.88E-05 7.84E-00 2.28E-15 5.57 7.20C-01 1.55C-03 3.88E-05 7.84E-00 2.28E-15 5.57 7.20C-01 1.55C-03 3.88E-05 7.84E-00 2.28E-15 5.57 7.20C-01 <td></td> <td></td> <td></td> <td></td> <td></td> <td></td> <td></td> <td></td> <td></td> <td>1.55</td> <td>0.00</td> <td>0.45</td> <td>0.838</td> <td>0.006</td> <td>0.006</td> <td></td> <td></td> <td></td>										1.55	0.00	0.45	0.838	0.006	0.006			
228 5.82E-05 5.86E-02 1.15E-03 3.41E-06 4.48E-15 531 38 1.70 1.65 0.01 0.35 0.841 -0.001 -0.001 20.88 252 2.24 23F-0 2.24 23F-0 3.25 0.01 0.48 0.39 0.00 0.028 2.24 376 2.2-1 2.35 2.2-1 2.35 2.2-1 2.35 2.2-1 2.35 2.1 1.00 0.38 0.03 0.002 1.02 2.2-1 2.2-2 3.6 3.0 2.2-2 1.03 1.0 0.00 0.28 0.85 - 4.029 2.172 2.49 2.8 3.0 2.0 0.00										1.52	0.01	0.471	0.941	0.002	0.000			
274 29 E-05 164E-01 31,E2-03 4,77E-06 8,24E-15 458 30 2,06 1,51 0,01 0,48 0,48 0,002 0,008 224 2376 2,26 2,32 1,61 1,68 0,00 0,31 0,48 0,002 0,009 0,009 0,009 0,009 2,009 0,009																		
137 3.88E-05 1.88E-05 1.88E-03 3.08E-06 3.76E-15 362 32 1.61 1.68 0.00 0.31 0.848 -0.025 -0.029 1724 305 a2-7																		
446 485E-05 180E-01 299E-03 8.73E-06 2.10E-14 409 22 1.53 1.71 0.00 0.28 0.850 0.029 2172 249 a2.85 1.85 0.00 0.																		
119 3.40E-05 4.78E-02 1.42E-03 1.63E-06 2.33E-15 579 57 1.60 1.62 0.02 0.37 0.842 -0.006 -0.004 2.134 307 a.2-9 3.2-14 3.88E-05 3.81E-02 4.88E-05 3.81E-02 9.23E-04 1.48E-06 1.28E-15 557 57 2.02 1.55 0.01 0.44 0.835 0.015 -0.021 1949 356 a.2-15 1.55 0.01 0.45 0.00 0.49 0.839 0.003 -0.002 1.004 0.015 0.005														_				
255 4,85E-05 7,41E-02 1,48E-03 3,59E-06 5,15E-15 562 38 1,72 1,66 0,01 0,33 0,837 0,008 0,000 0,007 2075 297 2,211 5,82E-05 1,82E-01 3,68E-03 1,06E-05 4,59E-14 387 2,0 1,70 1,69 0,01 0,30 0,848 0,023 0,018 2,292 319 3,215 3,215 3,315 3,32E-05 1,24E-05 6,69E-14 452 21 1,88 1,51 0,00 0,49 0,839 0,003 0,002 2,176 312 3,215														-0.006				a2-9
518 5.82E-05 1.82E-01 3.58E-03 1.06E-05 4.59E-14 387 20 1.70 1.69 0.01 0.30 0.848 -0.023 0.018 2292 319 a2-12 216 2.91E-05 1.06E-01 2.36E-03 3.08E-06 4.72E-15 555 41 1.54 1.79 0.01 0.20 0.844 -0.010 0.014 2236 447 a2-14 0.015								38	1.72		0.01	0.33			0.000	2075	297	a2-10
699 7.7TE-05 1.59E-01 3.33E-03 1.24E-05 6.69E-14 452 21 1.88 1.51 0.00 0.49 0.839 0.003 -0.002 2176 312 a2-12 c16 2.91E-05 1.06E-01 2.36E-03 3.08E-06 4.72E-15 555 41 1.54 1.79 0.01 0.20 0.844 -0.010 0.014 2236 447 a2-14 c16 3.88E-05 4.24E-02 9.62E-04 1.65E-06 1.39E-15 300 39 1.72 1.71 0.00 0.28 0.848 -0.024 -0.017 2126 646 a2-12 c10 4.85E-05 7.83E-02 1.72E-03 3.80E-06 6.06E-15 442 33 1.79 1.52 0.00 0.48 0.837 0.011 -0.012 1427 347 a2-14 c16 3.88E-05 1.34E-01 2.54E-03 1.01E-05 5.35E-14 359 20 1.60 1.52 0.01 0.48 0.837 0.011 -0.012 1427 347 a2-14 c17 0.00 0.28 0.848 0.0024 -0.021 1674 273 a2-17 1.00 0.00 0.28 0.848 0.007 0.001 1.00	104				1.48E-06						0.01					1949		a2-11
216 2.91E-05 1.06E-01 2.36E-03 3.08E-06 4.72E-15 5.555 41 1.54 1.79 0.01 0.20 0.844 -0.010 0.014 2236 447 a2-14 a2-15																		a2-12
61 3.88E-05 4.24E-02 9.62E-04 1.65E-06 1.39E-15 300 39 1.72 1.71 0.00 0.28 0.848 -0.024 -0.017 2126 646 a2-15																		a2-13
210																		a2-14
485 4.85E-05																		
248 3.49E.05 1.34E.01 2.54E.03 3.68E.06 7.86E.15 424 29 1.70 1.57 0.01 0.42 0.843 -0.007 -0.024 1527 275 a2-18 155 4.37E.05 8.41E.02 1.68E.03 3.68E.06 5.39E.15 340 29 1.56 1.58 0.01 0.41 0.842 -0.005 0.001 1852 381 a2-19 160 3.80E.05 1.51E.01 2.46E.03 4.39E.06 5.12E-15 488 31 1.77 1.63 0.07 0.30 0.828 0.035 -0.027 1759 219 a2-28 146 3.88E.05 1.32E.01 3.36E.03 1.92E.06 3.71E.15 601 54 1.93 1.56 0.01 0.43 0.842 -0.006 -0.022 1863 541 a2-29 144 5.82E.05 1.32E.01 3.36E.03 7.68E.06 3.82E.14 491 27 1.57 1.56 0.00 0.43 0.839 0.004 -0.017 2123 504 a2-29 141 3.40E.05 4.14E.02 1.58E.03 1.41E.06 2.89E.15 780 73 1.51 1.59 0.00 0.41 0.838 0.006 -0.039 2213 743 a2-29 144 1.340E.05 4.14E.02 1.58E.03 1.41E.06 2.89E.15 780 73 1.51 1.59 0.00 0.41 0.838 0.006 -0.039 2213 743 a2-29 144 1.340E.05 1.32E.01 4.09E.03 8.83E.06 3.83E.14 491 27 1.53 1.68 0.00 0.32 0.850 -0.028 0.021 1521 518 a2-29 1.32E.01 4.09E.03 8.83E.06 3.89E.14 497 21 1.61 1.71 0.01 0.29 0.828 0.035 -0.026 2079 261 a2-29 1.32E.03 1.32E.03 1.32E.03 2.77E.06 1.05E.14 407 21 1.61 1.79 0.01 0.29 0.828 0.035 0.002 0.000 2157 331 a2-20 1.32E.03 1.32E.03 1.03E.03																		
155																		
252 2.91E.05 1.51E.01 2.46E.03 4.99E.06 5.12E.15 458 31 1.77 1.63 0.07 0.30 0.828 0.035 -0.027 1759 219 a2.24 146 3.88E.05 4.94E.02 1.57E.03 1.92E.06 3.71E.15 601 54 1.93 1.56 0.01 0.43 0.842 -0.006 -0.021 1863 541 a2-2 141 3.40E.05 4.14E.02 1.58E.03 1.41E.06 2.89E.15 780 73 1.51 1.59 0.00 0.41 0.838 0.006 -0.039 2213 743 a2-2 236 7.77E.05 3.56E.02 1.32E.03 2.77E.06 1.05E.14 670 51 1.53 1.68 0.00 0.32 0.850 -0.028 -0.021 1521 518 a2-2 256 5.58E.05 1.82E.01 4.09E.03 8.83E.05 7.51E.14 407 21 1.61 1.79 0.01 0.20 0.851																1027		
146 3.88E.05 4.94E.02 1.57E.03 1.92E.06 3.71E.15 601 54 1.93 1.56 0.01 0.43 0.842 -0.006 -0.022 1863 541 a2-2. 474 5.82E.05 1.32E-01 3.56E.06 3.82E.14 491 27 1.57 1.56 0.00 0.43 0.839 0.004 -0.017 2123 504 a2-22 236 7.77E.05 3.56E.02 1.32E.03 2.77E.06 1.05E.14 670 51 1.53 1.68 0.00 0.32 0.850 -0.028 -0.021 1521 518 a2-2 390 4.85E.05 1.82E-01 4.09E-03 8.83E-06 3.93E-14 356 21 1.61 1.71 0.01 0.29 0.828 0.035 -0.026 2079 261 a2-22 3576 5.82E-05 5.31E-02 1.52E-03 3.09E-06 7.83E-15 546 42 1.81 1.50 0.01 0.50 0.839 0.00																		
474 5.82E-05 1.32E-01 3.36E-03 7.68E-06 3.82E-14 491 27 1.57 1.56 0.00 0.43 0.839 0.004 -0.017 2123 504 a2-22 141 3.40E-05 4.14E-02 1.58E-03 1.41E-06 2.89E-15 780 73 1.51 1.59 0.00 0.41 0.838 0.006 -0.028 -0.021 1521 518 a2-22 390 4.85E-05 1.82E-01 4.09E-03 8.83E-06 3.93E-14 356 21 1.61 1.71 0.01 0.29 0.828 0.035 -0.026 2079 261 a2-25 576 5.82E-05 1.95E-01 4.71E-03 1.13E-05 7.51E-14 407 21 1.61 1.71 0.01 0.29 0.828 0.035 -0.026 2.729 261 a2-25 553 46 42 1.81 1.50 0.01 0.20 0.851 -0.032 0.000 2157 331 a2-24 166																		
141 3.40E.05 4.14E.02 1.58E.03 1.41E.06 2.89E.15 780 73 1.51 1.59 0.00 0.41 0.838 0.006 -0.039 2213 743 a2.22 390 4.85E.05 1.82E.01 4.09E.03 8.83E.06 3.93E.14 356 21 1.61 1.71 0.01 0.29 0.828 0.035 -0.026 2079 261 a2-22 576 5.82E.05 1.95E.01 4.71E.03 1.13E.05 7.51E.14 407 21 1.61 1.79 0.01 0.20 0.851 -0.032 0.000 2157 331 a2-27 166 5.82E.05 5.31E-02 1.52E-03 3.09E-06 7.83E-15 546 42 1.81 1.50 0.01 0.50 0.839 0.000 2121 566 a2-22 496 4.85E-05 2.08E-01 6.17E-03 1.01E-05 8.95E-14 394 22 1.65 1.57 0.01 0.42 0.843 -0.0																		
236 7,77E-05 3,56E-02 1,32E-03 2,77E-06 1,05E-14 670 51 1,53 1,68 0,00 0,32 0,850 -0,028 -0,021 1521 518 a2-2-2 390 4,85E-05 1,82E-01 4,09E-03 8,83E-06 3,93E-14 356 21 1,61 1,77 0,01 0,29 0,828 0,035 -0,026 2079 261 a2-2: 576 5,82E-05 1,95E-01 4,71E-03 1,13E-05 7,51E-14 407 21 1,61 1,79 0,01 0,20 0,851 -0,032 0,000 2157 331 a2-2: 166 5,82E-05 5,31E-02 1,52E-03 3,09E-06 7,83E-15 546 42 1,81 1,50 0,01 0,50 0,839 0,004 0,000 22,383 632 a2-2.2 166 5,82E-05 4,07E-02 1,02E-03 2,37E-06 3,52E-15 555 46 1,63 1,58 0,01 0,42 <t></t>																		
390																		a2-24
576 5.82E-05 1.95E-01 4.71E-03 1.13E-05 7.51E-14 407 21 1.61 1.79 0.01 0.20 0.851 -0.032 0.000 2157 331 a2-24 166 5.82E-05 5.31E-02 1.52E-03 3.09E-06 7.83E-15 546 42 1.81 1.50 0.01 0.50 0.839 0.004 0.000 2283 632 a2-27 166 5.82E-05 4.07E-02 1.02E-03 2.37E-06 3.52E-15 555 46 1.63 1.58 0.01 0.41 0.842 -0.006 -0.007 2121 566 a2-21 496 4.85E-05 2.08E-01 6.17E-03 1.01E-05 8.95E-14 394 22 1.68 1.57 0.01 0.42 0.843 -0.009 -0.025 1828 331 a2-25 1.15E-01 3.42E-03 6.55E-06 2.75E-14 461 28 1.90 1.76 0.00 0.24 0.852 -0.036 -0.019 1468																		a2-25
213 5.82E-0.5 5.31E-0.2 1.52E-0.3 3.09E-0.6 7.83E-1.5 546 42 1.81 1.50 0.01 0.50 0.839 0.004 0.000 2383 632 a2.2° 1.66 5.82E-0.5 4.07E-0.2 1.02E-0.3 2.37E-0.6 3.52E-1.5 555 46 1.63 1.58 0.01 0.41 0.842 -0.006 -0.007 2121 566 a2.2° 1.02E-0.3 1.01E-0.5 8.95E-1.4 394 22 1.65 1.57 0.01 0.42 0.843 -0.009 -0.025 1828 331 a2.2° 1.02E-0.3 1.01E-0.5 4.53E-0.2 1.16E-0.3 1.98E-0.6 2.57E-1.5 602 52 1.68 1.52 0.00 0.47 0.831 0.027 0.006 2199 551 a2.3° 1.02E-0.3 1.03E-0.5 1.35E-0.1 3.42E-0.3 6.55E-0.6 2.75E-1.4 461 28 1.90 1.76 0.00 0.24 0.852 -0.036 -0.019 1.468 268 a2-3° 1.26 3.88E-0.5 5.49E-0.2 2.02E-0.3 2.13E-0.6 6.14E-1.5 472 4.6 1.57 1.75 0.00 0.25 0.851 0.034 0.015 2.164 6.59 a2.3° 1.35E-0.5 1.15E-0.1 2.45E-0.3 2.13E-0.6 6.14E-1.5 472 4.6 1.57 1.75 0.00 0.25 0.851 0.034 0.015 2.164 6.59 a2.3° 1.35E-0.5 1.15E-0.1 2.45E-0.3 3.70E-0.6 8.58E-1.5 754 4.6 1.67 1.59 0.01 0.43 0.836 0.013 0.008 2311 397 a2-3° 1.35E-0.5 1.25E-0.5 1.25E-0.3 4.18E-0.6 7.40E-1.5 371 28 1.66 1.66 0.00 0.34 0.8410.002 1.763 395 a2-3° 1.35E-0.5 1.33E-0.1 2.53E-0.3 4.18E-0.6 7.40E-1.5 371 28 1.66 1.66 0.00 0.34 0.842 0.006 0.009 2042 4.17 a2-3° 1.35E-0.5 1.35E-0.1 3.15E-0.3 1.62E-0.6 1.40E-1.5 666 6.0 1.50 1.60 0.01 0.39 0.835 0.014 0.003 2.268 558 a2-3° 1.35E-0.5 1.45E-0.1 3.15E-0.3 1.5E-0.5 1.6E-0.6 1.49E-1.4 473 30 1.60 1.78 0.00 0.22 0.848 0.023 0.016 1.867 2.69 a2-3° 1.866 3.11E-0.5 4.56E-0.2 9.85E-0.4 1.42E-0.6 9.38E-1.6 483 54 1.54 1.77 0.01 0.23 0.847 0.023 0.016 1.867 2.69 a2-3° 1.866 3.11E-0.5 4.56E-0.2 9.85E-0.4 1.42E-0.6 9.38E-1.6 483 54 1.54 1.77 0.01 0.23 0.847 0.024 0.008 0.031 1.470 0.21 3.23 0.008 1.40E-1.5 3.20E-1.4 3.86 2.3 1.56 1.69 0.00 0.31 0.849 0.008 0.031 1.470 0.21 3.24 4.24 1.24 1.24 1.24 1.25 0.00 0.00 0.34 0.842 0.004 0.004 0.003 1.40E-1.5 1.40E-0.0 1.25 0.45E-0.1 1.9E-0.3 1.97E-0.6 1.64E-1.5 411 42 1.71 1.62 0.01 0.37 0.86 0.013 0.004 0.004 0.001	576	5.82E-05	1.95E-01	4.71E-03	1.13E-05	7.51E-14	407	21	1.61	1.79	0.01	0.20	0.851	-0.032	0.000	2157	331	a2-26
496																2383		a2-27
151 4.37E-05 4.53E-02 1.16E-03 1.98E-06 2.57E-15 602 52 1.68 1.52 0.00 0.47 0.831 0.027 0.006 2199 551 a2-30 378 4.85E-05 1.35E-01 3.42E-03 6.55E-06 2.75E-14 461 28 1.90 1.76 0.00 0.24 0.852 -0.036 -0.019 1468 268 a2-31 126 3.88E-05 5.49E-02 2.02E-03 2.13E-06 6.14E-15 472 46 1.57 1.75 0.00 0.25 0.851 -0.034 -0.015 2164 659 a2-32 420 4.85E-05 1.15E-01 2.45E-03 5.58E-06 1.41E-14 595 33 1.67 1.57 0.01 0.43 0.836 0.013 0.008 2311 397 a2-32 358 4.85E-05 7.63E-02 1.91E-03 3.70E-06 8.58E-15 754 46 1.67 1.59 0.01 0.40 0.8		5.82E-05																a2-28
378 4,85E-05 1,35E-01 3,42E-03 6,55E-06 2,75E-14 461 28 1,90 1,76 0,00 0,24 0,852 -0,036 -0,019 1468 268 a2.31 126 3,88E-05 5,49E-02 2,02E-03 2,13E-06 6,14E-15 472 46 1,57 1,57 0,00 0,25 0,851 -0,034 -0,015 2164 659 a2-3 358 4,85E-05 7,63E-02 1,91E-03 3,70E-06 8,58E-15 754 46 1,67 1,59 0,01 0,43 0,836 0,013 0,008 2311 397 a2-3 358 4,85E-05 7,63E-02 1,91E-03 3,70E-06 8,58E-15 754 46 1,67 1,59 0,01 0,40 0,841 - -0,002 1763 395 a2-3 193 3,40E-05 1,52B-01 2,53E-03 4,18E-06 7,40E-15 371 28 1,66 1,66 0,00 0,34 0,842 <td></td> <td>a2-29</td>																		a2-29
126 3.88E-05 5.49E-02 2.02E-03 2.13E-06 6.14E-15 472 46 1.57 1.75 0.00 0.25 0.851 -0.034 -0.015 2164 659 a2-33 420 4.85E-05 1.15E-01 2.45E-03 5.58E-06 1.41E-14 595 33 1.67 1.57 0.01 0.43 0.836 0.013 0.008 2311 397 a2-33 358 4.85E-05 7.63E-02 1.91E-03 3.70E-06 8.58E-15 754 46 1.67 1.59 0.01 0.40 0.841 - -0.002 1763 395 a2-33 193 3.40E-05 1.23E-01 2.53E-03 4.18E-06 7.40E-15 371 28 1.66 1.66 0.00 0.34 0.842 -0.006 -0.009 2042 417 a2-33 306 3.88E-05 1.33E-01 3.15E-03 5.16E-06 1.49E-14 473 30 1.60 1.78 0.00 0.22 0.848<																		a2-30
420 4.85E-05 1.15E-01 2.45E-03 5.58E-06 1.41E-14 595 33 1.67 1.57 0.01 0.43 0.836 0.013 0.008 2311 397 a2-3: 358 4.85E-05 7.63E-02 1.91E-03 3.70E-06 8.58E-15 754 46 1.67 1.59 0.01 0.40 0.841 0.002 1.763 395 a2-3: 193 3.40E-05 1.23E-01 2.53E-03 4.18E-06 7.40E-15 371 28 1.66 1.66 0.00 0.34 0.842 -0.006 -0.009 2042 417 a2-3: 137 3.40E-05 4.75E-02 1.10E-03 1.62E-06 1.40E-15 666 60 1.50 1.60 0.01 0.39 0.835 0.014 0.003 2268 558 a2-3: 306 3.88E-05 1.33E-01 3.15E-03 5.16E-06 1.49E-14 473 30 1.60 1.78 0.00 0.22 0.848 -0.023 -0.016 1867 269 a2-3: 338 4.85E-05 1.45E-01 2.34E-03 7.03E-06 1.29E-14 386 23 1.56 1.69 0.00 0.31 0.849 -0.028 -0.031 1470 213 a2-3: 101 3.40E-05 5.79E-02 1.19E-03 1.97E-06 1.64E-15 411 42 1.71 1.62 0.01 0.37 0.836 0.013 -0.021 2304 469 a2-40 4511 2.65E-03																		a2-31
358 4,85E-05 7,63E-02 1,91E-03 3,70E-06 8,58E-15 754 46 1,67 1,59 0,01 0,40 0,841 - -0,002 1763 395 a2,34 193 3,40E-05 1,23E-01 2,55E-03 4,18E-06 7,40E-15 371 28 1,66 1,60 0,00 0,34 0,842 -0,006 -0,009 2042 417 a2-3: 306 3,8E-05 1,33E-01 3,15E-03 5,16E-06 1,49E-14 473 30 1,60 1,78 0,00 0,22 0,848 -0,023 -0,016 1867 269 a2-3: 86 3,11E-05 4,56E-02 9,85E-04 1,42E-06 9,38E-16 483 54 1,54 1,77 0,01 0,23 0,847 -0,021 -0,006 2386 515 a2-3 338 4,85E-05 1,43E-03 0,38E-16 483 54 1,54 1,77 0,01 0,23 0,847 -0,021 -0,006																		
193 3.40E-05 1.23E-01 2.53E-03 4.18E-06 7.40E-15 371 28 1.66 1.66 0.00 0.34 0.842 -0.006 -0.009 2042 417 a2-3: 137 3.40E-05 4.75E-02 1.10E-03 1.62E-06 1.40E-15 666 60 1.50 1.60 0.01 0.39 0.835 0.014 0.003 2268 558 a2-3 306 3.88E-05 1.33E-01 3.15E-03 5.16E-06 1.49E-14 473 30 1.60 1.78 0.00 0.22 0.848 -0.023 -0.016 1867 269 a2-3 86 3.11E-05 4.56E-02 9.85E-04 1.42E-06 9.38E-16 483 54 1.54 1.77 0.01 0.23 0.847 -0.021 -0.006 2386 515 a2-3 338 4.85E-05 1.45E-01 2.34E-03 7.03E-06 1.29E-14 386 23 1.56 1.69 0.00 0.31 0.849																		
137 3.40E-05 4.75E-02 1.10E-03 1.62E-06 1.40E-15 666 60 1.50 1.60 0.01 0.39 0.835 0.014 0.003 2268 558 a2-36 306 3.88E-05 1.33E-01 3.15E-03 5.16E-06 1.49E-14 473 30 1.60 1.78 0.00 0.22 0.848 -0.023 -0.016 1867 269 a2-37 86 3.11E-05 4.56E-02 9.85E-04 1.42E-06 9.38E-16 483 54 1.54 1.77 0.01 0.23 0.847 -0.021 -0.006 2386 515 a2-37 338 4.85E-05 1.45E-01 2.34E-03 7.03E-06 1.29E-14 386 23 1.56 1.69 0.00 0.31 0.849 -0.028 -0.031 1470 213 a2-37 101 3.40E-05 5.79E-02 1.19E-03 1.97E-06 1.64E-15 411 42 1.71 1.62 0.01 0.37 0.																		
306 3.88E-05 1.33E-01 3.15E-03 5.16E-06 1.49E-14 473 30 1.60 1.78 0.00 0.22 0.848 -0.023 -0.016 1867 269 a2-37 86 3.11E-05 4.56E-02 9.85E-04 1.42E-06 9.38E-16 483 54 1.54 1.79 0.01 0.23 0.847 -0.021 -0.06 2386 515 a2-38 338 4.85E-05 1.45E-01 2.34E-03 7.03E-06 1.29E-14 386 23 1.56 1.69 0.00 0.31 0.849 -0.028 -0.031 1470 213 a2-31 101 3.40E-05 5.79E-02 1.19E-03 1.97E-06 1.64E-15 411 42 1.71 1.62 0.01 0.37 0.836 0.013 -0.021 2304 469 a2-40 14511 2.65E-03 2.45E-04 2.45E-12 512 20 1.77 1.63 0.01 0.36 0.842 -0.04 -0.010																		
86 3.11E-05 4.56E-02 9.85E-04 1.42E-06 9.38E-16 483 54 1.54 1.77 0.01 0.23 0.847 -0.021 -0.006 2386 515 a2-36 338 4.85E-05 1.45E-01 2.34E-03 7.03E-06 1.29E-14 386 23 1.56 1.69 0.00 0.31 0.849 -0.028 -0.031 1470 213 a2-36 101 3.40E-05 5.79E-02 1.19E-03 1.97E-06 1.64E-15 411 42 1.71 1.62 0.01 0.37 0.836 0.013 -0.021 2304 469 a2-40 14511 2.65E-03 2.45E-04 2.45E-12 512 20 1.77 1.63 0.01 0.36 0.842 -0.004 -0.010																		
338 4.85E-05 1.45E-01 2.34E-03 7.03E-06 1.29E-14 386 23 1.56 1.69 0.00 0.31 0.849 -0.028 -0.031 1470 213 a2-39 101 3.40E-05 5.79E-02 1.19E-03 1.97E-06 1.64E-15 411 42 1.71 1.62 0.01 0.37 0.836 0.013 -0.021 2304 469 a2-40 14511 2.65E-03 2.45E-04 2.45E-12 512 20 1.77 1.63 0.01 0.36 0.842 -0.004 -0.010																		
101 3.40E-05 5.79E-02 1.19E-03 1.97E-06 1.64E-15 411 42 1.71 1.62 0.01 0.37 0.836 0.013 -0.021 2304 469 a2-40 14511 2.65E-03 2.45E-04 2.45E-12 512 20 1.77 1.63 0.01 0.36 0.842 -0.004 -0.010																		a2-39
14511 2.65E-03 2.45E-04 2.45E-12 512 20 1.77 1.63 0.01 0.36 0.842 -0.004 -0.010																		a2-40
	14311	4.03E-03					312	20	1.//	1.05	0.01	0.30	0.042	-0.004	-0.010			

 N_s = spontaneous track count; P_i = down-pit weighted ²³⁸U/⁴³Ca; Ω_i = track count area

†AFT single-grain ages are calculated using the LA-ICP-MS (ζ -calibration) method with modified $\zeta=8.2727$, standard error (ζ) = 0.1407 and 238 U total decay constant of 1.55125 × 10⁻¹⁰ yr⁻¹. Bottom table row displays the analysis sums, AFT central age \pm 1s error calculated in IsoplotR (Vermeesch, 2018), and the mean values for the tabulated elements/kinetic parameters. Aliquot grains marked with an asterisk experienced analysis failure from blowout during lasing and are omitted from summary age calculations but reported for completeness.

*Average values reported for F, Cl, OH, D_{par} , and effective Cl (eCl) in bottom row, median value shown for r_{mr0} ; Individual grain D_{par} values are the mean of 4 measurements. Aliquot-2 had two EPMA spots, one near the AFT laser ablation pit (A) and another elsewhere on the grain (B) to assess compositional heterogeneity. Elemental data for aliquot-2 (F, Cl, OH, r_{mr0}) are only reported in the table for spot A. Average wt % oxide total for aliquot-2 replicates is $97.4 \pm 1.8\%$; median = 98% (n = 74).

 \ddagger Individual isotopic sums U-Pb dates are common Pb-corrected using the Stacey & Kramers (1975) correction and 238 U/ 206 Pb and 207 Pb/ 206 Pb ratios.

Table 4. Apatite fission-track data for sample CB99-227, Trans-Hudson Orogen (lon/lat: -94.96948441, 56.46946203)

N_s	Area	²³⁸ U/ ⁴³ Ca	1s	$P_i\Omega_i$	$\sigma P_i^2 \Omega_i^2$	AFT age†	1s	Dpar	F⋆	Cl⋆	ОН∗	r_{mr0}	eCl (A)	eCl (B)	U–Pb‡	2s	aliquot
	(cm ²)					(Ma)	(Ma)	(µm)	(apfu)	(apfu)	(apfu)	1999	(apfu)	(apfu)	age (Ma)	(Ma)	grain
461	5.82E-05	1.33E-01	2.97E-03	7.77E-06	2.98E-14	473	26	2.09	1.65	0.01	0.34	0.848	-0.022	-	1526	208	a1-1
175	3.88E-05	4.07E-02	2.14E-03	1.58E-06	6.88E-15	856	80	1.91	1.55	0.01	0.44	0.838	0.008	_	1471	319	a1-2
367	5.82E-05	8.80E-02	1.97E-03	5.12E-06	1.32E-14	567	34	2.16	-	_	_	_	_	_	1581	221	a1-3
131	2.91E-05	7.94E-02	1.85E-03	2.31E-06	2.91E-15	452	42	2.16	1.69	0.01	0.30	0.848	-0.025	-	1559	152	a1-4
257	9.71E-05	3.00E-02	6.97E-04	2.91E-06	4.57E-15	692	48	2.16	1.61	0.01	0.38	0.843	-0.009	-	1621	293	a1-5
241	5.82E-05	6.46E-02	1.74E-03	3.76E-06	1.02E-14	509	37	2.20	1.53	0.01	0.46	0.841	-0.001	-	1572	213	a1-6
72	3.88E-05	2.42E-02	5.89E-04	9.38E-07	5.23E-16	606	74	2.12	1.53	0.01	0.46	0.837	0.011	-	1605	301	a1-7
211	4.85E-05	3.83E-02	8.69E-04	1.86E-06	1.78E-15	878	65	1.59	1.74	0.01	0.25	0.851	-0.033	-	1541	219	a1-8
103	4.85E-05	2.99E-02	7.08E-04	1.45E-06	1.18E-15	562	58	2.10	1.50	0.01	0.49	0.835	0.016	-	1582	323	a1-9
197	5.82E-05	3.77E-02	9.32E-04	2.20E-06	2.95E-15	703	54	2.25	1.67	0.02	0.31	0.838	0.007	-	1528	281	a1-10
71	3.88E-05	1.98E-02	7.41E-04	7.70E-07	8.27E-16	721	91	1.80	1.59	0.01	0.39	0.837	0.011	_	1433	566	a1-11
438	5.82E-05	9.98E-02	3.01E-03	5.81E-06	3.08E-14	595	35	1.89	1.59	0.01	0.39	0.833	0.022	-	1516	261	a1-12
153	4.37E-05	5.64E-02	1.22E-03	2.46E-06	2.83E-15	494	42	2.22	1.64	0.01	0.35	0.846	-0.019	-	1596	219	a1-13
334	6.21E-05	5.62E-02	1.37E-03	3.49E-06	7.22E-15	746	46	2.07	1.73	0.01	0.26	0.851	-0.034	-	1541	234	a1-14
343	7.77E-05	3.51E-02	1.24E-03	2.73E-06	9.29E-15	965	64	2.22	1.64	0.01	0.35	0.847	-0.021		1485	374	a1-15
615	5.82E-05	2.29E-01	4.70E-03	1.34E-05	7.51E-14	370	18	1.64	1.53	0.01	0.47	0.836	0.013	0.026	1722	285	a2-1
714	5.82E-05	2.18E-01	4.38E-03	1.27E-05	6.51E-14	449	21	1.70	1.43	0.01	0.56	0.834	0.018	0.025	1661	219	a2-2
103	3.98E-05	3.87E-02	6.06E-03	1.54E-06	5.82E-14	530	99	2.16	1.60	0.01	0.39	0.837	0.010		_	-	a2-3
218	9.71E-05	8.79E-02	3.06E-03	8.53E-06	8.80E-14	208	16	1.74	1.45	0.01	0.54	0.837	0.010	0.036	-	-	a2-4
114	4.37E-05	4.08E-02	1.90E-03	1.78E-06	6.91E-15	509	54	1.43	1.59	0.01	0.41	0.835	0.015	-0.023	-	-	a2-5
118	9.71E-05	2.15E-02	1.73E-03	2.09E-06	2.82E-14	452	56	1.54	1.51	0.01	0.48	0.839	0.003	0.013	-	-	a2-6
138	5.82E-05	4.77E-02	9.40E-04	2.78E-06	3.00E-15	399	35	1.63	1.60	0.01	0.40	0.835	0.017	-0.021	1626	478	a2-7
80	4.37E-05	3.91E-02	8.71E-03	1.71E-06	1.45E-13	376	94	1.41	-	-	-	-	-	-	-	-	a2-8
145	4.85E-05	2.88E-02	7.38E-04	1.40E-06	1.28E-15	806	71	1.49	1.55	0.00	0.45	0.842	-0.006	0.001	1631	607	a2-9
384	2.91E-05	3.37E-01	6.10E-03	9.81E-06	3.15E-14	316	18	1.68	1.57	0.01	0.42	0.837	0.009	0.025	1593	195	a2-10
472	4.85E-05	1.95E-01	3.91E-03	9.47E-06	3.61E-14	400	21	1.79	1.45	0.01	0.55	0.832	0.024	0.016	1635	232	a2-11
294	6.79E-05	5.78E-02	1.41E-03	3.92E-06	9.20E-15	592	39	2.16	1.52	0.02	0.46	0.833	0.020	0.028	1624	426	a2-12
440	4.85E-05	1.67E-01	3.35E-03	8.11E-06	2.65E-14	434	24	1.89	1.52	0.02	0.46	0.833	0.022	0.017	1615	289	a2-13
128	4.85E-05	4.35E-02	1.25E-03	2.11E-06	3.67E-15	483	46	1.89	1.69	0.01	0.30	0.849	-0.026	0.010	1560	421	a2-14
324	9.71E-05	5.34E-02	1.42E-03	5.19E-06	1.89E-14	497	32	1.87	1.68	0.01	0.31	0.848	-0.022	0.017	1547	661	a2-15
119	4.85E-05	3.60E-02	1.23E-03	1.75E-06	3.57E-15	541	54	1.64	1.40	- 0.01	- 0.50	- 0.941	- 0.001	- 0.022	1548	535	a2-16
404	4.85E-05 5.82E-05	1.25E-01	3.01E-03	6.05E-06	2.14E-14	530	31	1.71	1.49	0.01	0.50	0.841	-0.001	-0.022	1473	324	a2-17
195		6.32E-02	1.57E-03	3.68E-06	8.35E-15	424	33	1.71	1.61	0.01	0.38	0.837	0.011	-0.003	1641	418	a2-18
234 242	4.85E-05 5.82E-05	6.93E-02 7.26E-02	2.43E-03 2.72E-03	3.37E-06 4.23E-06	1.39E-14	551	42 35	1.72 1.65	1.51 1.52	0.02	0.48 0.46	0.831	0.028 0.012	0.018	-	-	a2-19 a2-20
203	2.91E-05	1.50E-02	7.94E-03	4.23E-06 4.37E-06	2.50E-14 5.35E-14	457 373	33	1.77	1.52	0.01		0.834	0.012	0.008	-	-	
140	3.88E-05	5.66E-02	2.68E-03	2.20E-06	1.08E-14	507	50	1.60	1.57	0.01	0.47	0.837	0.018	0.008	-	-	a2-21 a2-22
555	5.82E-05	1.55E-01	4.73E-03	9.05E-06	7.59E-14	488	27	2.03	1.58	0.01	0.43	0.837	-0.011	0.003	-	_	
129	4.85E-05	4.29E-02	1.45E-03	2.08E-06	4.96E-15	493	47	1.56	1.60	0.01	0.42	0.839	0.005	-0.003	-		a2-23 a2-24
84	4.85E-05	1.98E-02	1.45E-03 1.35E-03	9.59E-07	4.30E-15	687	89	1.72	1.57	0.01	0.39	0.838	0.003	0.045	_	_	a2-24 a2-25
300	4.85E-05	1.70E-02	3.69E-03	9.39E-07 8.23E-06	3.21E-14	295	19	1.72	1.56	0.01	0.42	0.843	-0.009	0.043	_	_	a2-25 a2-26
316	4.85E-05	9.24E-02	2.09E-03	4.49E-06	1.03E-14	558	35	1.77	1.46	0.01	0.43	0.839	0.004	-0.009	1637	292	a2-20 a2-27
222	5.82E-05	9.24E-02 1.02E-01	2.09E-03 2.14E-03	5.95E-06	1.03E-14 1.56E-14	301	22	1.73	1.72	0.00	0.33	0.839	0.004	-0.001	1037	-	a2-27 a2-28
238	2.91E-05	2.18E-01	4.37E-03	6.34E-06	1.62E-14	303	21	2.11	1.72	0.00	0.28	0.842	-0.004	0.029	1665	221	a2-26 a2-29
63	3.88E-05	3.33E-02	1.76E-03	1.29E-06	4.69E-15	391	54	1.43	1.71	0.01	0.42	0.843	-0.004	-0.041	-	-	a2-29 a2-30
195	4.85E-05	8.53E-02	2.19E-03	4.14E-06	1.13E-14	378	29	2.17	1.47	0.01	0.28	0.835	0.015	-0.041	1736	430	a2-30
248	4.85E-05	7.39E-02	1.99E-03	3.59E-06	9.34E-15	548	39	1.51	1.47	0.01	0.52	0.836	0.013	0.001	1546	396	a2-31
290	5.82E-05	1.22E-01	3.49E-03	7.09E-06	4.14E-14	330	22	1.72	1.62	0.01	0.32	0.830	-0.001	0.007	1504	250	a2-32
98	2.91E-05	6.77E-02	2.12E-03	1.97E-06	3.80E-15	399	43	1.66	1.95	0.02	0.04	0.856	-0.001	0.030	1614	279	a2-33
328	3.88E-05	2.15E-01	5.78E-03	8.34E-06	5.04E-14	317	20	1.92	1.51	0.01	0.48	0.839	0.003	-0.001	1753	304	a2-34
		2.1312-01	J.10L-03												1133	504	- a2-55
12444	2.63E-03			2.19E-04	1.14E-12	486	22	1.83	1.58	0.01	0.41	0.838	0.001	0.007			

 N_s = spontaneous track count; P_i = down-pit weighted ²³⁸U/⁴³Ca; Ω_i = track count area

†AFT single-grain ages are calculated using the LA-ICP-MS (ζ -calibration) method with modified $\zeta=8.2727$, standard error (ζ) = 0.1407 and 238 U total decay constant of 1.55125 \times 10⁻¹⁰ yr⁻¹. Bottom table row displays the analysis sums, AFT central age \pm 1s error calculated in IsoplotR (Vermeesch, 2018), and the mean values for the tabulated elements/kinetic parameters.

*Average values reported for F, Cl, OH, D_{par} , and effective Cl (eCl) in bottom row, median value shown for r_{mr0} ; Individual grain D_{par} values are the mean of 4 measurements. Aliquot-2 had two EPMA spots, one near the AFT laser ablation pit and another elsewhere on the grain to assess compositional heterogeneity. Elemental data for aliquot-2 (F, Cl, OH, r_{mr0}) are only reported in the table for spot A. Average wt % oxide total for aliquot-2 replicates is $99.6 \pm 1.2\%$; median = 99.7% (n = 65).

 $\ddagger Individual \ isotopic \ sums \ U-Pb \ dates \ are \ common \ Pb-corrected \ using \ the \ Stacey \& \ Kramers \ (1975) \ correction \ and \ ^{238}U/^{206}Pb \ and \ ^{207}Pb/^{206}Pb \ ratios.$

Table 5. Apatite fission-track data for sample 12RM086, western Superior Province (lon/lat: -86.9604038, 52.874674)

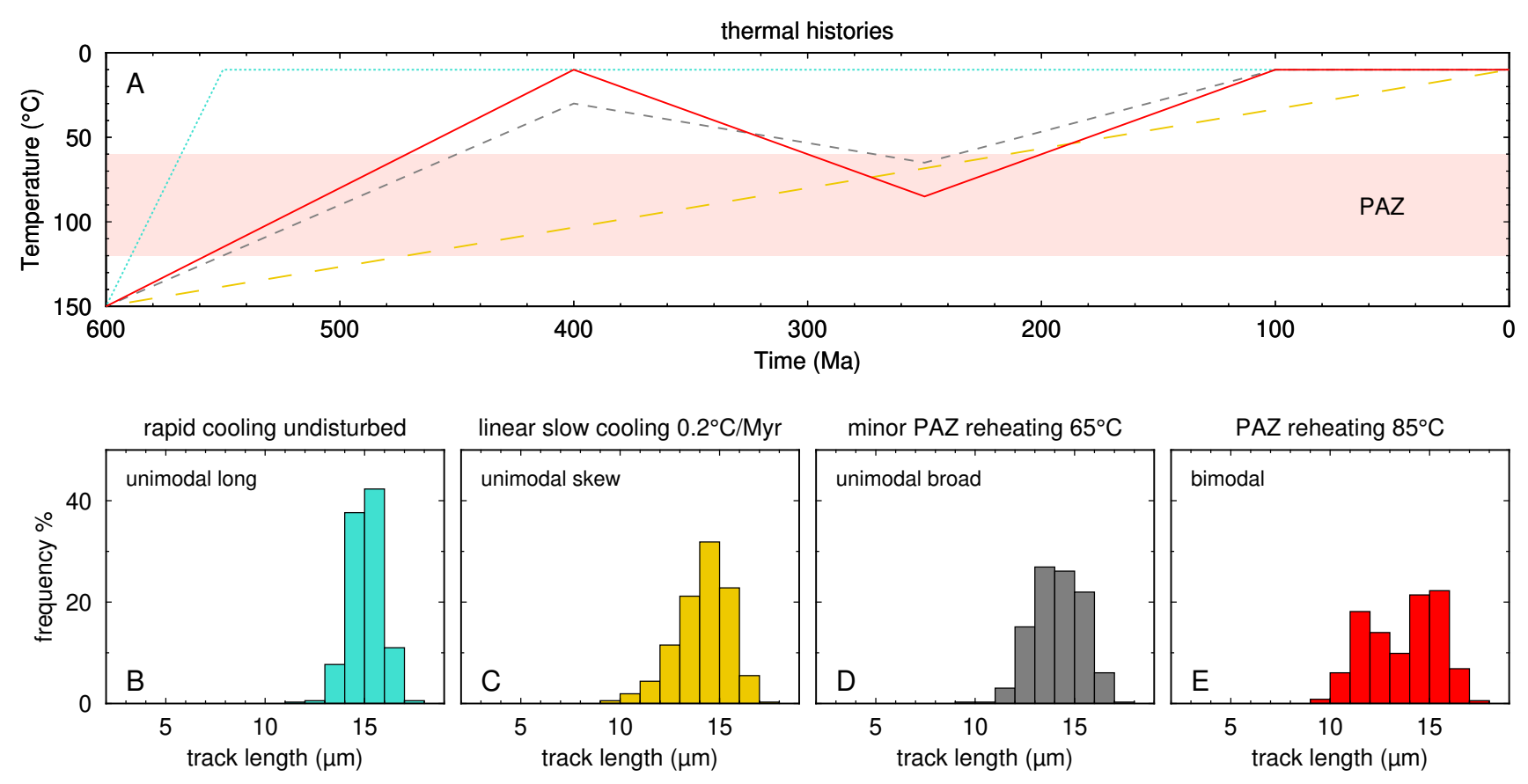
180		Table 3.	Apame	11881011-11	ack uata	ioi samp	TE TEININ	000, 1	VCSICI	n Supc	1101 1 1	OVIIICE	(1011)	iai00	.900403	00, 32.07	+0/+)	
1966 1975	N_s		²³⁸ U/ ⁴³ Ca	1s	$P_i\Omega_i$	$\sigma P_i^2 \Omega_i^2$	AFT age†	1s	D_{par}	F⋆	Cl⋆	OH⋆		eCl (A)	eCl (B)	U-Pb‡	2s	aliquot
As As As As As As As As		(cm ²)					(Ma)	(Ma)	(µm)	(apfu)	(apfu)	(apfu)	1999	(apfu)	(apfu)	age (Ma)	(Ma)	grain
As As As As As As As As	350	6.79E-05	7.41E-02	7 58E-03	5.03E-06	2.65E-13	551	64	2.25	1 66	0.00	0.34	0.846	-0.017	_	_	_	a1-1
171 1.2																_		a1-2
111 291E-05 6.16E-07 7.5E-06 2.86E-14 493 66 1.94 1.83 0.00 0.17 0.877 0.020 al																2288	1013	a1-3
146E-05 AGE-06															_	_	_	a1-4
Color Colo															-	-	-	a1-5
174 6.21E-0.5 7.10E-0.2 5.8E-0.3 4.41E-0.6 1.31E-1.4 416 45 1.95 1.79 0.00 0.01 0.03 0.06 0.063															_	-	_	a1-6
188 3.88E-05 5.86E-02 4.04E-03 2.56E-06 3.11E-14 401 45 198 197 0.00 0.03 0.860 0.0063 1.63 1.38E-05 5.26E-06 2.90E-03 3.74E-07 2.11E-15 570 73 1.88 1.80 0.00 0.22 0.852 0.005 1.63 1.38E-05 5.26E-06 2.90E-03 3.74E-07 2.11E-15 570 3.78 1.88 1.80 0.00 0.00 0.25 0.852 0.005 1.75 0.00 0.25 0.852 0.005 1.75 0.00 0.25 0.852 0.005 1.75 0.00 0.25 0.852 0.005 1.75 0.00 0.25 0.852 0.005 1.75 0.00 0.25 0.852 0.005 1.75 0.00 0.25 0.852 0.005 1.75 0.00 0.25 0.852 0.005 1.75 0.00 0.25 0.852 0.005 1.75 0.00 0.25 0.852 0.005 1.75 0.00 0.25 0.852 0.005 1.75 0.00 0.25 0.852 0.005 1.75 0.00 0.25 0.852 0.005 1.75 0.00 0.25 0.852 0.005 1.75 0.00 0.25 0.852 0.005 1.75 0.00 0.25 0.852 0.005 1.75 0.00 0.25 0.852 0.005 1.75 0.00 0.25 0.852 0.005 1.75 0.00 0.25 0.852 0.005 1.75 0.00 0.25 0.852 0.005 0.00 0.25 0.852 0.005 0.															-	-	-	a1-7
85 3,88E-05 5,63E-02 0,29E-03 1,64E-06 1,30E-14 416 54 1,95 1,78 0,00 0,22 0,85 0,005 1 204 5,82E-05 7,63E-02 0,29E-03 8,78E-07 211E-15 770 78 1,89 1,80 1 205 5,82E-05 7,82E-03 1,82E-03 1,82E-06 3,82E-14 371 30 41,89 1,80 1 207 5,82E-05 7,82E-03 1,82E-03 1,82E-06 3,82E-15 3,003 66 2,82E-15 3,000 0,00 0,00 0,00 0,00 0,00 0,00 0,																-		a1-8
63 1.55E-05 5.65E-02 2.96E-03 8.74E-07 2.11E-15 5.70 78 1.89 1.80 0.0 0.20 8.46 0.017 0.1 0.1 119 3.46E-05 5.78E-02 2.85E-03 1.56E-05 9.5E-15 6.03 6.8 2.14 1.78 0.00 0.20 0.846 0.017 0.1 0.1 12.43E-05 4.39E-02 2.85E-03 1.56E-05 9.5E-15 6.03 6.8 2.14 1.78 0.00 0.20 0.846 0.017 0.1 0.1 179 3.11E-05 5.3E-02 1.95E-03 1.07E-05 0.9E-15 6.03 6.8 2.14 1.78 0.00 0.20 0.840 0.002 0.000 0.20 0.85E-15 0.000 0.20 0.200																-		a1-9
204 5.82E-05 7.88E-02 4.15E-03 4.41E-06 5.85E-14 371 34 1.88 1.70 0.00 0.20 0.846 0.017 1.11 3.40E-05 4.88E-02 4.05E-03 1.07E-06 9.99E-15 0.006 6.8 2.14 1.78 0.00 0.20 0.846 0.007 1.15 2.43E-06 4.45E-03 0.45E-03 1.07E-06 9.99E-15 0.006 6.8 1.77 1.72 0.00 0.22 0.845 0.006 0.15 0.006 0.007 0.											0.00	0.22	0.852	-0.035	-	_		a1-10
19 3.40E-05 4.39E-02 2.88E-03 1.56E-06 9.39E-15 6.03 6.8 2.14 1.78 0.00 0.20 0.849 0.002 1.167 4.88E-05 4.39E-02 4.00E-03 0.37E-06 9.65E-15 6.07 5.3 1.88 1.85 0.01 0.27 0.842 0.006 - 2.251 585 1.167 0.31E-05 5.30E-04 7.38E-07											0.00	0.20	0.846	0.017	_	_		a1-11
51 2.43E-05 4.39E-02 4.05E-03 1.07E-05 0.65E-15 384 65 1.97 1.72 0.00 0.22 0.852 0.006 - - - 0.251 555 al-79 3.11E-05 5.30E-02 1.93E-05 1.65E-06 3.58E-15 3.85 4.6 2.25 1.80 0.00 0.15 0.856 0.008 - - - 2.251 555 al-79 3.11E-05 5.30E-02 1.93E-05 1.65E-06 3.58E-15 3.85 4.6 2.25 1.80 0.00 0.15 0.856 0.008 - - - 2.251 555 al-165 3.85 4.6 2.25 3.85																		a1-12
																_	_	a1-13
79 3.11E-05 5.30E-02 1.93E-03 1.65E-06 3.85E-15 385 46 2.25 1.80 0.00 0.15 0.854 0.018 - - - 1.125 3.85E-05 1.55E-02 5.80E-04 7.53E-05 7.93E-15 506 48 2.16 1.77 0.00 0.29 0.847 0.020 - 2.233 552 3.1125 5.25E-05 5.23E-05 5.25E-05 5.25E-0																2251	585	a1-15
53 4.85E-05 5.86E-02 5.80E-04 7.53E-07 7.93E-16 557 80 2.04 1.71 0.00 0.29 0.844 -0.012 - - - - - - 2.33E-05 5.97E-02 1.72E-06 1.62E-06 1.66E-15 323 41 1.88 1.73 0.00 0.24 0.015 - 2.366 2.33 1.83 9.71E-05 5.97E-00 1.18E-14 1.88 1.73 0.00 0.24 0.015 - 2.266 2.63 1.14E-03 3.88E-05 6.28E-15 4.68 4.18 1.88 1.73 0.00 0.38 8.01 - 2.247 3.13 1.11E-14 1.73 0.00 0.33 0.84 0.001 - 2.040 1.33 3.88E-05 3.74E-02 1.83E-04 1.53E-04 <																	_	a1-16
128 4.85E-05 6.97E-07 1.72E-03 1.02E-06 2.33E-15 5.05 4.05 5.05 4.05 5.															-	_	_	a1-17
1882 1882	128	4.85E-05	4.14E-02		2.01E-06	3.39E-15	506	48	2.16	1.77	0.00	0.29	0.847	-0.020	-	2323	552	a1-18
145 388E-05 6.23E-02 1.32E-03 2.42E-06 2.63E-15 519 53 2.12 1.67 0.00 0.27 0.850 0.031 - 2.347 313 a1- 159 4.85E-05 3.37E-02 8.06E-04 1.64E-06 1.33E-15 7.58 64 2.19 1.67 0.00 0.33 0.848 -0.016 - 2.440 430 a1- 154 4.85E-05 1.79E-02 1.04E-03 2.05E-16 2.56E-15 534 48 1.73 - 0.00 0.33 0.848 -0.016 - 2.440 430 a1- 140 4.85E-05 3.25E-05 1.04E-03 2.05E-06 2.56E-15 534 48 1.73 - 0.00 0.27 0.835 0.015 - 2.150 2.05E-10 1.04E-03 2.05E-06 2.56E-15 534 48 1.73 - 0.00 0.27 0.835 0.015 - 2.150 2.05E-10 1.04E-03 2.05E-06 2.56E-15 534 48 1.73 - 0.00 0.27 0.835 0.016 - 2.150 2.05E-10 1.04E-03 2.05E-06 2.56E-15 534 48 1.73 - 0.00 0.27 0.835 0.016 - 2.150 2.05E-10 2.05E-15 2.05E-15 535 3.75E-05 3.05E-05 3															_			a1-19
1959 4.88E-05 4.14E-02 9.70E-04 1.61E-06 1.42E-15 519 53 2.12 1.67 0.00 0.38 0.841 0.002 - 2308 372 and 53 4.85E-05 3.77E-02 4.65E-04 8.71E-07 5.09E-16 4.85E 68 2.04 1.73 0.00 0.33 0.846 -0.016 - 2.440 430 and 4.85E-05 4.29E-06 1.04E-03 2.08E-06 2.56E-15 534 48 1.73 - 0.00 0.33 0.848 -0.024 - 2.028 410 and 4.85E-05 4.29E-06 2.08E-06 2.56E-15 534 48 1.73 - 0.00 0.27 0.835 0.015 - 2.150 2.95 and 1.20 2.150 2.25 and 1.25															-	2256		a1-20
53 485E05 1.79E06 4.65E04 1.75E07 5.75E 64 2.19 1.67 0.00 0.33 0.848 0.016 2.440 430 al- 140 4.85E05 1.79E06 1.79E06 2.50E15 5.18 3.18 3.18 0.024 2.028 410 al- 140 4.85E05 3.25E06 1.79E06 2.50E15 5.18 3.18 3.18 3.18 0.027 0.838 0.006 0.014 2.17 7.84 al- 108 4.85E05 5.39E06 1.24E03 2.66E16 3.62E15 5.18 3.18 3.18 3.18 0.01 0.19 0.848 0.002 0.018 2.402 5.04 4.85E05 6.73E06 1.34E03 2.66E06 3.62E15 3.53 3.18 3.18 3.18 3.18 3.18 3.18 4.85E05 7.10E06 1.38E03 3.56E06 4.84E15 3.55 3.18 3.18 3.18 3.18 3.18 5.15 4.85E05 7.10E05 1.09E03 3.44E06 2.79E15 3.53 3.18 3.18 3.18 3.18 5.15 4.85E05 7.10E05 1.09E03 3.46E06 2.79E15 3.53 3.18 3.18 3.18 3.18 5.16 4.85E05 8.17E05 1.09E03 3.45E06 5.06E15 4.87 3.18																		a1-21
53 488E-05 4.99E-05 4.96E-04 8.71E-07 5.09E-16 485 68 2.04 1.73 0.00 0.33 0.848 0.004 2028 410 4.18 410 4.85E-05 4.99E-05 4.99E-0															-			a1-22
140															-			a1-23
200 9.71E-05 3.32E-02 2.14E-04 3.22E-06 6.22E-15 518 39 1.63 1.73 0.00 0.27 0.838 0.006 0.014 2217 784 22 144 4.85E-05 5.49E-05 2.14E-03 2.66E-06 6.36E-15 3.27 33 1.80 1.73 0.00 0.27 0.847 0.002 -0.021 -0.021 2.243 516 2.2 1.66 0.9 1.67E-05 1.24E-02 4.07E-04 1.02E-06 1.56E-15 451 57 1.61 1.96 0.01 0.03 0.860 -0.062 -0.029 2.122 1126 4.2 1.2															_			
188E-05 5.49E-02 1.24E-03 2.66E-06 3.62E-15 327 33 1.56 1.81 0.01 0.19 0.840 0.002 -0.018 2402 540 32 43 44 48.5E-05 5.73E-05 1.38E-03 3.26E-06 4.84E-15 3.55 31 1.81 0.01 0.02 0.27 0.847 -0.021 -0.021 2.348 516 3.2 518															0.014			a2-1
144 4,85E-05 6,73E-02 1,35E-03 3,26E-06 4,48E-15 355 31 1,80 1,73 0,00 0,27 0,847 -0,021 -0,021 2,343 516 2,245 516 4,85E-05 7,10E-02 1,00E-03 3,44E-06 2,79E-15 353 30 1,89 1,66 0,01 0,33 0,809 -0,00E -0,002 -0,029 -0,025 -0,029 -0,025																		a2-1
68 9.71E-05 1.24E-02 4.07E-04 1.20E-06 1.56E-15 451 57 1.61 1.96 0.01 0.03 0.860 -0.062 -0.029 2122 1126 a.2 151 4.85E-05 7.10E-02 1.09E-03 3.44E-06 2.79E-15 353 30 1.89 1.66 0.01 0.33 0.843 -0.009 0.008 2.304 369 a.2 268 9.71E-05 4.49E-02 1.06E-03 4.36E-06 1.06E-14 489 33 1.86 1.76 0.00 0.24 0.839 0.003 -0.038 2.594 677 a.2 186 5.82E-05 8.71E-02 1.70E-03 3.09E-06 6.08E-15 441 381 3.8 1.64 1.63 0.01 0.36 0.832 0.024 -0.022 2.378 617 a.2 186 5.82E-05 8.73E-02 1.73E-03 3.09E-06 6.17E-15 481 38 1.64 1.63 0.01 0.36 0.832 0.024 -0.022 2.378 617 a.2 136 4.85E-05 4.95E-02 1.58E-03 5.08E-06 9.09E-15 447 27 1.77 1.66 0.00 0.34 0.845 -0.015 -0.047 2.488 471 a.2 136 4.85E-05 4.95E-02 1.58E-03 5.41E-06 2.55E-14 363 26 1.68 1.59 0.00 0.41 0.841 -0.003 -0.032 2.825 1.85 6.77.E-05 1.07E-01 2.59E-03 8.31E-06 4.05E-14 354 21 1.89 1.79 0.00 0.21 0.848 -0.025 -0.019 2.822 467 a.2 181 4.85E-05 6.93E-02 1.85E-03 3.36E-06 6.25E-15 431 34 1.74 1.85 0.00 0.29 0.29 0.034 0.002 2.457 696 a.2 128 4.37E-05 8.12E-02 1.91E-03 3.55E-06 6.97E-15 292 27 1.69 1.80 0.00 0.20 0.851 -0.034 0.002 0.043 2.875 587 a.2 130 5.82E-05 1.05E-01 0.25E-03 4.39E-06 6.25E-15 391 3.45 1.60 0.00 0.18 0.845 -0.015 0.004 0.005 2.259 897 a.2 131 3.40E-05 5.28E-05 2.15E-03 1.37E-06 2.50E-04 3.99E-06 8.56E-15 4.9 32 1.59 1.81 0.00 0.10 0.18 0.845 -0.015 0.004 0.025 2.534 479 3.2 134 3.89E-05 5.28E-05 1.05E-01 2.27E-03 6.11E-06 1.75E-14 407 2.6 1.60 1.66 0.01 0.13 0.845 0.005 0.004 0.025 2.534 479 3.2 135 5.82E-05 1.05E-01 2.27E-03 6.11E-06 1.75E-14 407 2.6 1.60 1.66 0.01 0.13 0.842 0.004 0.035 2.534 479 3.2 136 4.85E-05 5.28E-05 1.17E-03 3.31E-06 6.33E-15 388 31 1.59 1.81 0.00 0.02 0.88 0.802 0.004 0.035 2.534 479 3.2 137 4.85E-05 5.28E-05 1.17E-03 3.31E-06 6.33E-15 388 31 1.59 1.81 0.00 0.00 0.18 0.845 0.005 0.004 0.005 2.259 897 a.2 138 3.48E-05 5.28E-05 1.05E-01 2.27E-03 6.11E-06 1.35E-15 388 31 1.59 1.81 0.00 0.00 0.18 0.845 0.005 0.004 0.005 2.259 897 a.2 139 4.85E-05 5.08E-05 2.10E-01 2.27E-05 6.18E-15 388 31 1.50 1.79 1.00 0.00 0.00 0.00 0.00																		a2-3
151 4.85E-05 7.10E-02 1.09E-03 3.44E-06 2.79E-15 353 30 1.89 1.66 0.01 0.33 0.83 0.009 0.008 2304 3699 a.2 201 4.85E-05 8.17E-02 1.70E-03 3.96E-06 6.80E-15 407 31 1.87 1.60 0.01 0.40 0.843 0.009 0.027 2.436 551 a.2 258 5.82E-05 5.29E-02 1.35E-03 3.08E-06 6.17E-15 481 38 1.64 1.63 0.01 0.36 0.832 0.024 0.022 2.378 617 a.2 258 5.82E-05 8.73E-02 1.71E-03 5.08E-06 9.90E-15 407 27 1.77 1.66 0.00 0.34 0.845 0.015 0.047 2488 471 a.2 258 5.82E-05 8.73E-02 1.71E-03 5.08E-06 9.90E-15 452 40 1.71 1.76 0.00 0.23 0.851 0.031 0.013 2.885 1185 a.2 244 9.71E-05 5.75E-02 1.58E-03 3.36E-06 6.25E-15 432 40 1.71 1.76 0.00 0.24 0.841 0.003 0.023																		a2-4
201 4.85E-05 8.17E-02 1.70E-03 3.96E-06 6.80E-15 407 31 1.87 1.60 0.01 0.40 0.843 -0.009 -0.027 2436 551 az 258 5.82E-05 5.29E-02 1.55E-03 3.08E-06 6.17E-15 481 38 1.64 1.63 0.01 0.36 0.832 0.0024 -0.022 2378 617 az 258 5.82E-05 8.73E-02 1.71E-03 5.08E-06 9.90E-15 407 27 1.77 1.66 0.00 0.34 0.845 -0.015 -0.047 2488 471 az 244 9.71E-05 5.57E-02 1.58E-03 5.41E-06 2.35E-14 363 26 1.68 1.59 0.00 0.41 0.841 -0.003 -0.029 2320 567 az 2.366 7.77E-05 1.07E-01 2.59E-03 8.31E-06 2.25E-15 431 34 1.74 1.85 0.00 0.15 0.853 -0.038 -0.020 -0.019 2382 467 az 3.388 9.71E-05 8.53E-05 0.93E-02 1.63E-03 3.55E-06 6.97E-15 2.92 2.7 1.69 1.80 0.00 0.25 0.851 -0.034 -0.025 -0.019 2382 467 az 2.244 9.71E-05 8.12E-05 1.17E-05 3.53E-04 3.99E-06 8.56E-15 429 32 1.59 1.81 0.00 0.29 0.839 0.002 -0.043 2875 587 az 2.244 9.71E-05 8.12E-05 1.27E-05 6.11E-06 6.175E-14 407 26 1.60 1.60 0.00 0.18 0.845 -0.015 -0.024 2259 897 az 4.24E-05 0.24E-05 2.27E-05 0.11E-05 3.25E-06 3.22E-15 349 3.5 E-06 0.20E-05 3.25E-05 0.25E-05 3.25E-05 0.25E-05 3.25E-05 0.25E-05 3.25E-05 0.25E-05 3.25E-05								30	1.89					-0.009				a2-5
Segret S		9.71E-05	4.49E-02		4.36E-06	1.06E-14			1.86		0.00	0.24			-0.038		677	a2-6
58.8E.05 8.73E-02 1.71E-03 5.08E-06 9.90E-15 407 27 1.77 1.66 0.00 0.34 0.845 -0.015 -0.047 2488 471 az 244 9.71E-05 5.57E-02 1.58E-03 5.41E-06 2.35E-14 363 26 1.68 1.59 0.00 0.41 0.841 -0.003 -0.001 2.382 667 az-366 7.77E-05 1.07E-01 2.59E-03 8.31E-06 4.05E-14 354 21 1.89 1.79 0.00 0.21 0.848 -0.025 -0.019 2382 467 az-338 9.71E-05 8.53E-02 1.68E-06 6.25E-15 431 34 1.74 1.85 0.00 0.15 0.848 -0.022 2.02 2.71 1.99 1.80 0.00 0.29 0.839 0.002 -0.043 2875 587 az-214 9.71E-05 4.1E-02 9.53E-04 3.99E-06 8.56E-15 429 32 1.59 1.81 0.00 0.20																		a2-7
136 4.85E-05 4.95E-02 9.16E-04 2.40E-06 1.97E-15 452 40 1.71 1.76 0.00 0.23 0.851 -0.031 -0.013 2885 1185 a2-346 7.77E-05 1.07E-01 2.59E-03 8.31E-06 2.35E-14 363 26 1.68 1.59 0.00 0.41 0.841 -0.003 -0.029 2.320 567 a2-366 7.77E-05 1.07E-01 2.59E-03 8.31E-06 2.35E-14 363 26 1.68 1.59 0.00 0.21 0.848 -0.025 -0.019 2.382 467 a2-338 9.71E-05 8.53E-02 1.48E-03 3.36E-06 6.25E-15 431 34 1.74 1.85 0.00 0.15 0.853 -0.038 -0.020 2.457 696 a2-338 9.71E-05 8.12E-02 1.48E-03 8.28E-06 2.07E-14 329 20 1.84 1.70 0.00 0.29 0.839 0.002 -0.043 2.2875 587 a2-322 4.77E-05 4.12E-02 5.35E-06 6.97E-15 2.92 2.77 1.69 1.80 0.00 0.20 0.851 -0.034 -0.024 2.259 897 a2-310 5.82E-05 1.05E-01 2.27E-03 6.11E-06 1.75E-14 407 26 1.60 1.66 0.01 0.34 0.844 -0.012 -0.019 2.522 414 a2-325 4.75E-05 3.26E-02 1.17E-03 2.56E-06 3.22E-15 349 35 1.52 1.83 0.01 0.17 0.848 -0.023 -0.050 2.615 656 a2-32E-05 4.77E-05 4.77E-05 4.77E-05 4.77E-05 4.76E-02 1.23E-03 3.74E-06 9.13E-15 348 31 1.58 1.76 0.00 0.18 0.845 -0.016 -0.016 2.416 667 a2-32E-05 3.48E-05 2.26E-03 3.27E-06 1.84E-15 349 31 1.58 1.76 0.00 0.18 0.845 -0.016 -0.016 2.416 667 a2-32E-05 3.48E-05 3.28E-05 3.																		a2-8
244 9.71E-05 5.57E-02 1.58E-03 5.41E-06 2.35E-14 363 26 1.68 1.59 0.00 0.41 0.841 -0.003 -0.029 2320 567 a2- 181 4.85E-05 6.93E-02 1.63E-03 3.36E-06 4.05E-14 354 21 1.89 1.79 0.00 0.21 0.848 -0.025 -0.019 2382 467 a2- 1838 9.71E-05 8.53E-02 1.48E-03 8.28E-06 2.07E-14 329 20 1.84 1.70 0.00 0.29 0.839 0.002 -0.043 2875 587 a2- 182 4.37E-05 8.12E-02 1.91E-03 3.55E-06 6.97E-15 292 27 1.69 1.80 0.00 0.20 0.851 -0.034 -0.026 2459 515 a2- 184 9.71E-05 4.11E-02 9.53E-04 3.99E-06 8.56E-15 429 32 1.59 1.81 0.00 0.18 0.845 -0.015 -0.024 2259 897 a2- 185 4.85E-05 5.28E-02 1.17E-03 2.56E-06 3.22E-15 349 35 1.52 1.83 0.01 0.17 0.848 -0.023 -0.050 2615 656 a2- 186 4.85E-05 5.28E-02 1.17E-03 2.56E-06 3.22E-15 349 35 1.52 1.83 0.01 0.17 0.848 -0.023 -0.050 2615 656 a2- 187 4.85E-05 6.08E-02 1.26E-03 3.47E-06 9.13E-15 348 31 1.58 1.76 0.00 0.24 0.846 -0.016 -0.016 -0.016 2.416 667 a2- 187 4.85E-05 7.23E-02 1.26E-03 3.51E-06 4.35E-15 319 29 1.79 1.64 0.02 0.34 0.846 -0.016 -0.016 2.217 449 a2- 187 4.85E-05 7.23E-02 1.64E-03 3.51E-06 4.29E-15 353 30 1.71 1.93 0.00 0.70 0.856 -0.049 -0.033 2410 408 a2- 187 4.85E-05 2.78E-02 1.35E-03 3.51E-06 4.29E-15 501 54 1.59 1.81 0.00 0.18 0.845 -0.036 0.006 2322 436 a2- 188 4.85E-05 7.23E-02 1.26E-03 3.51E-06 4.29E-15 501 54 1.85 0.02 0.13 0.842 -0.004 -0.035 2534 797 a2- 189 4.85E-05 7.23E-02 1.26E-03 3.51E-06 1.35E-15 319 29 1.79 1.64 0.02 0.34 0.833 0.022 -0.011 2.377 449 a2- 189 4.85E-05 7.23E-02 1.64E-03 3.51E-06 4.29E-15 501 54 1.53 1.88 0.00 0.11 0.852 -0.036 0.006 2322 436 a2- 185 4.85E-05 2.78E-02 9.36E-04 1.35E-06 2.40E-15 501 54 1.59 1.79 0.00 0.26 0.848 -0.023 -0.030 2.314 1.047 a2- 185 4.85E-05 2.78E-02 9.36E-04 1.35E-06 2.40E-15 501 54 1.59 1.70 0.00 0.26 0.848 -0.023 -0.033 2.377 780 a2- 185 4.85E-05 3.05E-02 9.04E-04 1.48E-06 2.40E-15 501 54 1.59 1.70 0.00 0.29 0.844 -0.002 -0.031 2.457 472 a2- 185 4.85E-05 5.71E-02 1.66E-03 3.45E-06 6.42E-15 501 55 1.75 1.70 0.00 0.29 0.848 -0.023 -0.033 2.314 1.047 a2- 185 4.85E-05 5.71E-02 1.66E-03 2.48E-06 6.42E-15 511 55 1.70 0.00 0.20 0.2		5.82E-05																a2-9
366 7.77E-05 1.07E-01 2.59E-03 8.31E-06 4.05E-14 354 21 1.89 1.79 0.00 0.21 0.848 -0.025 -0.019 2382 467 a2-185 328 4.85E-05 6.93E-02 1.46E-03 8.28E-06 2.07E-14 329 20 1.84 1.70 0.00 0.29 0.839 0.002 -0.043 2875 587 a2-128 4.37E-05 8.12E-02 1.91E-03 3.55E-06 6.97E-15 292 27 1.69 1.80 0.00 0.20 0.851 -0.034 -0.026 2459 515 a2-144 7.71E-05 4.11E-02 5.53E-04 3.99E-06 6.95E-15 429 32 1.59 1.81 0.00 0.18 0.845 -0.015 -0.024 -0.026 2259 897 a2-144 7.71E-05 4.11E-02 5.53E-04 3.99E-06 8.56E-15 429 32 1.59 1.81 0.00 0.18 0.845 -0.015 -0.024 -0.025 2259 897 a2-144 4.85E-05 5.28E-02 1.17E-03 1.97E-06 2.59E-15 349 35 1.52 1.83 0.01 0.17 0.848 -0.012 -0.019 2.522 414 a2-154 4.85E-05 4.07E-02 1.05E-03 1.97E-06 2.59E-15 348 31 1.58 1.76 0.00 0.24 0.846 -0.016 -0.016 -0.016 2416 667 a2-154 4.85E-05 7.23E-02 1.94E-03 3.31E-06 4.35E-15 319 29 1.79 1.64 0.02 0.34 0.833 0.022 -0.011 2377 449 a2-154 4.85E-05 3.14E-02 1.05E-03 2.05E-06 4.29E-15 628 54 1.69 1.74 0.00 0.26 0.841 -0.003 -0.037 -0.053 2410 408 a2-154 4.85E-05 3.14E-02 1.01E-03 3.52E-06 2.20E-15 628 54 1.59 1.79 1.70 0.01 0.29 0.837 0.010 -0.060 2563 650 a2-154 4.85E-05 3.14E-02 1.01E-03 3.25E-06 2.20E-15 628 54 1.59 1.79 1.70 0.01 0.29 0.837 0.010 -0.060 2.563 650 a2-154 4.85E-05 3.14E-02 1.35E-03 3.20E-06 4.29E-15 628 54 1.59 1.79 1.70 0.01 0.29 0.837 0.010 -0.060 2.563 650 a2-154 4.85E-05 3.14E-02 1.35E-03 3.20E-06 2.20E-15 628 54 1.59 1.79 1.70 0.01 0.29 0.837 0.010 0.003 0.033 2.314 4.004 4.002 0.033 0.033 0.034 0.004 0.033 0.033 0.033 0.034 0.004 0.033 0.034 0.004 0.033 0.006 0.00																		a2-10
181																		
338 9.71E-05 8.53E-02 1.48E-03 8.28E-06 2.07E-14 329 20 1.84 1.70 0.00 0.29 0.839 0.002 -0.043 2875 587 a2- 128 4.37E-05 8.12E-02 1.91E-03 3.55E-06 6.97E-15 292 27 1.69 1.80 0.00 0.20 0.851 -0.034 -0.026 2459 515 a2- 1310 5.82E-05 1.05E-01 2.27E-03 6.11E-06 1.75E-14 407 26 1.60 1.60 0.01 0.34 0.845 -0.015 -0.024 2259 897 a2- 1310 5.82E-05 1.05E-01 2.27E-03 6.11E-06 1.75E-14 407 26 1.60 1.66 0.01 0.34 0.844 -0.012 -0.019 2522 414 a2- 1310 5.82E-05 1.05E-01 2.27E-03 6.11E-06 1.75E-14 407 26 1.60 1.66 0.01 0.34 0.844 -0.012 -0.019 2522 414 a2- 1311 4.85E-05 5.28E-02 1.17E-03 2.56E-06 3.22E-15 349 35 1.52 1.83 0.01 0.17 0.848 -0.023 -0.050 2615 656 a2- 131 3.40E-05 4.07E-02 1.05E-03 1.97E-06 2.59E-15 398 42 1.62 1.85 0.02 0.13 0.842 -0.004 -0.035 2534 797 a2- 131 3.40E-05 6.08E-02 1.26E-03 2.07E-06 1.84E-15 478 45 1.60 1.82 0.00 0.18 0.852 -0.036 0.006 2322 436 a2- 131 3.40E-05 9.74E-02 1.94E-03 3.31E-06 4.35E-15 319 29 1.79 1.64 0.02 0.34 0.833 0.022 -0.011 2377 449 a2- 152 4.85E-05 4.19E-02 1.35E-03 2.03E-06 4.29E-15 628 54 1.69 1.74 0.00 0.26 0.841 -0.003 -0.037 2514 865 a2- 162 4.85E-05 3.14E-02 1.01E-03 1.52E-06 2.40E-15 501 54 1.53 1.88 0.00 0.11 0.852 -0.036 -0.034 2877 1152 a2- 185 4.85E-05 5.78E-02 9.36E-04 1.35E-06 2.04E-15 501 54 1.53 1.88 0.00 0.11 0.852 -0.036 -0.033 2737 780 a2- 185 4.85E-05 5.05E-02 1.35E-03 3.29E-06 1.28E-14 449 37 1.79 1.70 0.01 0.29 0.837 0.010 -0.033 2737 780 a2- 185 4.85E-05 5.05E-02 1.35E-03 3.21E-06 4.29E-15 545 58 1.46 1.71 0.00 0.29 0.834 0.003 -0.033 2737 780 a2- 185 4.85E-05 5.05E-02 1.35E-03 3.21E-06 4.29E-15 545 58 1.46 1.71 0.00 0.29 0.834 0.003 -0.033 2737 780 a2- 185 4.85E-05 5.6E-02 1.35E-03 3.21E-06 4.29E-15 545 58 1.46 1.71 0.00 0.29 0.834 0.003 0.031 2457 472 a2- 185 4.85E-05 5.6E-02 1.35E-03 3.21E-06 4.95E-15 545 58 1.46 1.71 0.00 0.29 0.834 0.003 0.031 2457 472 a2- 185 4.85E-05 5.6E-02 1.14E-03 2.73E-06 3.06E-15 422 52 1.60 1.79 0.00 0.21 0.848 0.003 0.031 2457 472 a2- 185 4.85E-05 5.6E-02 1.35E-03 3.21E-06 4.95E-15 545 58 1.46 1.71 0.00 0.29 0.837 0.010 0.000 2																		a2-12
228 4.37E-05 8.12E-02 1.91E-03 3.55E-06 6.97E-15 292 27 1.69 1.80 0.00 0.20 0.851 -0.034 -0.026 2459 515 a2- 2310 5.82E-05 1.05E-01 2.27E-03 6.11E-06 1.75E-14 407 26 1.60 1.66 0.01 0.34 0.844 -0.012 -0.019 2522 414 a2- 111 4.85E-05 5.28E-02 1.17E-03 2.56E-06 3.22E-15 349 35 1.52 1.83 0.01 0.17 0.848 -0.023 -0.050 2615 656 a2- 98 4.85E-05 4.07E-02 1.05E-03 1.97E-06 2.59E-15 349 35 1.52 1.83 0.01 0.17 0.848 -0.023 -0.050 2615 656 a2- 124 3.40E-05 6.08E-02 1.26E-03 2.07E-06 1.84E-15 478 45 1.60 1.82 0.00 0.18 0.852 -0.036 0.006 2322 436 a2- 124 3.40E-05 6.08E-02 1.26E-03 2.07E-06 1.84E-15 478 45 1.60 1.82 0.00 0.18 0.852 -0.036 0.006 2322 436 a2- 131 3.40E-05 7.4E-02 1.23E-03 3.51E-06 6.33E-15 319 29 1.79 1.64 0.02 0.34 0.833 0.022 -0.011 2377 449 a2- 152 4.85E-05 7.23E-02 1.64E-03 3.51E-06 6.33E-15 353 30 1.71 1.93 0.00 0.07 0.856 -0.049 -0.053 2410 408 a2- 162 4.85E-05 4.19E-02 1.35E-03 2.03E-06 4.29E-15 628 54 1.69 1.74 0.00 0.26 0.841 -0.003 -0.037 2514 805 a2- 14 4.85E-05 2.78E-02 9.36E-04 1.35E-06 2.40E-15 501 54 1.53 1.88 0.00 0.11 0.852 -0.036 -0.034 2877 1152 a2- 17 4.85E-05 6.79E-02 2.33E-03 3.29E-06 2.06E-15 501 54 1.53 1.88 0.00 0.11 0.852 -0.036 -0.034 2877 1152 a2- 18 4.85E-05 6.79E-02 2.33E-03 3.29E-06 2.06E-15 542 52 1.60 1.79 0.00 0.26 0.848 -0.023 -0.033 2314 1.047 a2- 185 4.85E-05 6.79E-02 1.35E-03 3.29E-06 2.90E-15 545 58 1.46 1.71 0.00 0.26 0.848 -0.023 -0.033 2314 1.047 a2- 185 4.85E-05 6.79E-02 1.35E-03 3.29E-06 2.90E-15 545 58 1.46 1.71 0.00 0.29 0.844 -0.010 -0.060 2563 650 a2- 198 4.85E-05																		a2-13
214 9.71E.05 4.11E.02 9.53E.04 3.99E.06 8.56E.15 429 32 1.59 1.81 0.00 0.18 0.845 -0.015 -0.024 2259 897 az. 110 5.82E.05 1.05E.01 2.27E.03 6.11E.06 1.75E.14 407 26 1.66 0.01 0.34 0.844 -0.012 -0.019 2522 414 az. 111 4.85E.05 5.28E.02 1.17E.03 2.56E.06 3.22E.15 349 35 1.52 1.83 0.01 0.17 0.848 -0.023 -0.050 2615 656 az. 98 4.85E.05 4.07E.02 1.05E.03 1.97E.06 2.59E.15 349 35 1.52 1.83 0.01 0.17 0.848 -0.023 -0.050 2615 656 az. 150 7.77E.05 4.74F.02 1.23E.03 3.47E.06 9.13E.15 348 31 1.58 1.76 0.00 0.24 0.846 -0.016 -0.016 -0.016 2416 667 az. 124 3.40E.05 6.08E.02 1.26E.03 2.07E.06 1.84E.15 478 45 1.60 1.82 0.00 0.18 0.852 -0.036 0.006 2322 436 az. 131 3.40E.05 9.74E.02 1.94E.03 3.31E.06 4.35E.15 319 29 1.79 1.64 0.02 0.34 0.833 0.022 -0.011 2377 449 az. 152 4.85E.05 7.28E.02 1.35E.03 2.03E.06 4.29E.15 628 54 1.69 1.74 0.00 0.26 0.841 -0.003 -0.037 2514 865 az. 162 4.85E.05 3.14E.02 1.01E.03 1.52E.06 2.40E.15 501 54 1.53 1.88 0.00 0.11 0.852 -0.036 0.004 2877 1152 az. 171 4.85E.05 6.79E.02 2.33E.03 3.29E.06 1.28E.14 449 37 1.79 1.70 0.01 0.29 0.837 0.010 -0.060 2563 650 az. 185 4.85E.05 5.29Fe.02 9.36E.04 1.35E.06 2.32E.15 545 58 1.64 1.71 0.00 0.29 0.837 0.010 -0.060 2563 650 az. 187 4.85E.05 5.05E.02 1.35E.03 3.21E.06 4.29E.15 545 58 1.64 1.71 0.00 0.29 0.837 0.010 -0.060 2563 650 az. 188 4.85E.05 5.05E.02 1.35E.03 3.21E.06 4.29E.15 545 58 1.64 1.71 0.00 0.29 0.844 -0.010 -0.031 2457 472 az. 185 4.85E.05 5.05E.02 1.35E.03 3.21E.06 4.29E.15 511 55 1.74 1.81 0.01 0.18 0.848 -0.023 -0.031 2457 472 az. 185 4.85E.05 5.62E.02 1.35E.03 2.73E.06 6.06E.15 431 37 1.55 1.76 0.00 0.24 0.849 -0.028 -0.039 2334 547 az. 187 4.85E.05 5.62E.02 1.14E.03 2.73E.06 6.06E.15 431 37 1.55 1.76 0.00 0.24 0.849 -0.028 -0.039 2334 547 az. 187 4.85E.05 5.62E.02 1.14E.03 2.73E.06 6.00E.15 431 37 1.55 1.76 0.00 0.24 0.849 -0.028 -0.039 2334 547 az. 188 4.85E.05 5.64E.02 1.31E.03 2.73E.06 6.00E.15 431 37 1.55 1.76 0.00 0.24 0.849 -0.028 -0.039 2334 547 az. 188 4.85E.05 5.64E.02 1.31E.03 2.74E.06 6.10E.15 294 25 1.41 1.60 0.0																		a2-15
310 5.82E-05 1.05E-01 2.27E-03 6.11E-06 1.75E-14 407 26 1.60 1.66 0.01 0.34 0.844 -0.012 -0.019 2.522 414 a2- 111 4.85E-05 5.28E-02 1.17E-03 2.56E-06 3.22E-15 349 35 1.52 1.83 0.01 0.17 0.848 -0.023 -0.050 2.615 656 a2- 98 4.85E-05 4.07E-02 1.05E-03 1.97E-06 2.59E-15 398 42 1.62 1.85 0.02 0.13 0.842 -0.004 -0.035 2.534 797 a2- 150 7.77E-05 4.47E-02 1.23E-03 3.47E-06 9.13E-15 348 31 1.58 1.76 0.00 0.24 0.846 -0.016 -0.016 2416 667 a2- 124 3.40E-05 6.08E-02 1.26E-03 2.07E-06 1.84E-15 478 45 1.60 1.82 0.00 0.18 0.852 -0.036 0.006 2.322 436 a2- 131 3.40E-05 9.74E-02 1.94E-03 3.51E-06 4.35E-15 319 29 1.79 1.64 0.02 0.34 0.833 0.022 -0.011 2.377 449 a2- 154 4.85E-05 7.23E-02 1.64E-03 3.51E-06 6.33E-15 353 30 1.71 1.93 0.00 0.07 0.856 -0.049 -0.053 2410 408 a2- 162 4.85E-05 4.19E-02 1.35E-03 2.03E-06 4.29E-15 628 54 1.69 1.74 0.00 0.26 0.841 -0.003 -0.037 2514 865 a2- 174 4.85E-05 2.78E-02 9.36E-04 1.35E-06 2.60E-15 501 54 1.53 1.88 0.00 0.11 0.852 -0.036 -0.034 2877 1152 a2- 185 4.85E-05 2.97E-02 9.94E-04 1.35E-06 2.06E-15 422 52 1.60 1.79 0.00 0.21 0.848 -0.023 -0.030 2314 1047 a2- 185 4.85E-05 6.62E-02 1.35E-03 3.21E-06 4.29E-15 426 35 1.64 1.74 0.00 0.26 0.848 -0.023 -0.033 2737 780 a2- 171 4.85E-05 6.62E-02 1.35E-03 3.21E-06 4.29E-15 426 35 1.64 1.74 0.00 0.26 0.848 -0.023 -0.033 2737 780 a2- 171 4.85E-05 6.62E-02 1.35E-03 3.21E-06 4.29E-15 426 35 1.64 1.74 0.00 0.29 0.844 -0.010 -0.060 2.563 650 a2- 185 4.85E-05 6.62E-02 1.35E-03 3.21E-06 4.29E-15 426 35 1.64 1.71 0.00 0.29 0.844 -0.010 -0.060 2.563 650 a2- 186 4.85E-05 5.62E-02 1.14E-03 2.30E-06 1.28E-14 499 37 1.79 1.70 0.01 0.18 0.848 -0.023 -0.033 2737 780 a2- 187 4.85E-05 5.62E-02 1.14E-03 2.30E-06 4.99E-15 426 35 1.64 1.71 0.00 0.29 0.844 -0.010 -0.060 2.563 650 a2- 188 4.85E-05 5.62E-02 1.14E-03 2.30E-06 0.20E-15 431 37 1.55 1.76 0.00 0.39 0.841 -0.001 -0.060 2.564 674 2.2- 188 4.85E-05 5.62E-02 1.14E-03 2.30E-06 0.20E-15 431 37 1.55 1.76 0.00 0.39 0.841 -0.001 -0.001 2.2777 933 a2- 186 4.85E-05 5.64E-02 1.31E-03 2.48E-06 6.48E-15 407 39 1.75 1.70 0.00 0.																		a2-16
98	310	5.82E-05	1.05E-01		6.11E-06	1.75E-14	407	26	1.60		0.01	0.34	0.844	-0.012			414	a2-17
150 7,77E-05 4,47E-02 1,23E-03 3,47E-06 9,13E-15 348 31 1,58 1,76 0,00 0,24 0,846 -0,016 -0,016 2416 667 a2-124 3,40E-05 6,08E-02 1,26E-03 2,07E-06 1,84E-15 478 45 1,60 1,82 0,00 0,18 0,852 -0,036 0,006 2322 436 a2-131 3,40E-05 0,74E-02 1,94E-03 3,31E-06 4,35E-15 319 29 1,79 1,64 0,02 0,34 0,833 0,022 -0,011 2377 449 a2-154 4,85E-05 7,23E-02 1,64E-03 3,51E-06 6,33E-15 353 30 1,71 1,93 0,00 0,07 0,856 -0,049 -0,053 2410 408 a2-162 4,85E-05 4,19E-02 1,35E-03 2,03E-06 4,29E-15 628 54 1,69 1,74 0,00 0,26 0,841 -0,003 -0,037 2514 865 a2-96 4,85E-05 2,78E-02 2,36E-04 1,35E-06 2,40E-15 501 54 1,53 1,88 0,00 0,11 0,852 -0,036 -0,034 2877 1152 a2-171 4,85E-05 6,79E-02 2,33E-03 3,29E-06 1,28E-14 449 37 1,79 1,70 0,01 0,29 0,837 0,010 -0,060 2563 650 a2-99 4,85E-05 3,05E-02 9,94E-04 1,44E-06 2,32E-15 545 58 1,46 1,74 0,00 0,26 0,848 -0,023 -0,033 2737 780 a2-171 4,85E-05 6,62E-02 1,35E-03 3,21E-06 4,29E-15 545 58 1,46 1,74 0,00 0,29 0,844 -0,010 -0,060 2563 650 a2-99 4,85E-05 3,05E-02 9,04E-04 1,44E-06 2,32E-15 545 58 1,46 1,74 0,00 0,29 0,844 -0,010 -0,060 2563 650 a2-171 4,85E-05 3,05E-02 9,04E-04 1,44E-06 2,32E-15 545 58 1,46 1,74 0,00 0,29 0,844 -0,010 -0,060 2563 650 a2-171 4,85E-05 3,05E-02 9,04E-04 1,48E-06 1,92E-15 511 55 1,74 1,81 0,01 0,18 0,848 -0,023 -0,041 2,738 9,67 a2-171 4,85E-05 5,62E-02 1,14E-03 2,73E-06 3,06E-15 4,31 3,7 1,55 1,76 0,00 0,24 0,849 -0,023 -0,041 2,738 9,67 a2-171 4,85E-05 5,62E-02 1,14E-03 2,73E-06 4,89E-15 4,96 41 1,75 1,82 0,00 0,18 0,846 -0,018 -0,012 2,797 9,33 a2-126 4,85E-05 5,14E-02 1,33E-06 6,48E-15 4,	111		5.28E-02		2.56E-06	3.22E-15		35	1.52	1.83		0.17			-0.050			a2-18
124 3,40E-05 6,08E-02 1,26E-03 2,07E-06 1,84E-15 478 45 1,60 1,82 0,00 0,18 0,852 -0.036 0,006 2322 436 a2-131 3,40E-05 9,74E-02 1,94E-03 3,31E-06 4,35E-15 319 29 1,79 1,64 0,02 0,34 0,833 0,022 -0.011 2,377 449 a2-154 4,85E-05 7,23E-02 1,64E-03 3,51E-06 6,33E-15 353 30 1,71 1,93 0,00 0,07 0,856 -0.049 -0.053 2,410 408 a2-152 4,85E-05 4,19E-02 1,35E-03 2,03E-06 4,29E-15 628 54 1,69 1,74 0,00 0,26 0,841 -0.003 -0.037 2,514 865 a2-162 4,85E-05 3,14E-02 1,01E-03 1,52E-06 2,40E-15 501 54 1,53 1,88 0,00 0,11 0,852 -0.036 -0.034 2,877 1,52 a2-171 4,85E-05 6,79E-02 2,33E-03 3,29E-06 1,28E-14 449 37 1,79 1,70 0,01 0,29 0,837 0,010 -0.060 2,563 650 a2-198 4,85E-05 2,97E-02 9,94E-04 1,44E-06 2,32E-15 545 58 1,46 1,74 0,00 0,26 0,848 -0.023 -0.033 2,737 780 a2-198 4,85E-05 3,05E-02 9,04E-04 1,48E-06 1,92E-15 511 55 1,74 1,81 0,01 0,18 0,848 -0.023 -0.041 2,738 967 a2-198 4,85E-05 4,74E-02 1,11E-03 2,30E-06 2,90E-15 676 52 1,73 1,65 0,01 0,35 0,847 -0.021 -0.019 2,381 513 a2-147 4,85E-05 5,62E-02 1,14E-03 2,73E-06 3,06E-15 431 37 1,55 1,76 0,00 0,24 0,849 -0.028 -0.039 2,334 547 a2-147 4,85E-05 5,71E-02 1,66E-03 2,48E-06 6,48E-15 496 41 1,75 1,82 0,00 0,12 0,848 -0.023 -0.041 2,738 967 a2-147 4,85E-05 5,51E-02 1,66E-03 2,48E-06 6,48E-15 496 41 1,75 1,82 0,00 0,18 0,848 -0.023 -0.041 2,738 967 a2-147 4,85E-05 5,64E-02 1,14E-03 2,73E-06 6,10E-15 2,94 25 1,41 1,60 0,00 0,29 0,837 0,001 0,001 2,297 9,33 a2-147 4,85E-05 5,64E-02 1,14E-03 2,73E-06 6,10E-15 2,94 25 1,41 1,60 0,00 0,24 0,849 0,028 0,039 2,334 547 a2-147 4,85E-05 5,64E-02 1,14E-03 2,74E-06 4,85E-15 496 41 1,75 1,82 0,00 0,18 0,846 0,018 0,002 0,041 2,445 723 a2-133 4,85E-05 5,64E-02 1,31E-03 2,48E-06 6,48E-15 497 3,91 1,75 1,70 0,00 0,24 0,849 0,002 0,004 2,466 742 a2-147 4,85E-05 5,64E-02 1,31E-03 2,48E-06 6,48E-15 496 41 1,75 1,82 0,00 0,18 0,846 0,018 0,002 0,004 2,466 742 a2-147 4,85E-05 5,64E-02 1,31E-03 2,48E-06 6,48E-15 497 3,33 3,71E-06 6,64E-15 357 2,91 1,43 1,79 0,00 0,21 0,851 0,004 2,004 2,466 742 a2-147 4,85E-05 5,64E-02 1,31E-03 2,48E-06 6,64E-15 357																		a2-19
131 3.40E-05 9.74E-02 1.94E-03 3.31E-06 4.35E-15 319 29 1.79 1.64 0.02 0.34 0.833 0.022 -0.011 2377 449 a2-154 4.85E-05 7.23E-02 1.64E-03 3.51E-06 6.33E-15 353 30 1.71 1.93 0.00 0.07 0.856 -0.049 -0.053 2410 408 a2-156 4.85E-05 4.19E-02 1.35E-03 2.03E-06 4.29E-15 628 54 1.69 1.74 0.00 0.26 0.841 -0.003 -0.037 2514 865 a2-156 4.85E-05 3.14E-02 1.01E-03 1.52E-06 2.40E-15 501 54 1.53 1.88 0.00 0.11 0.852 -0.036 -0.034 2877 1152 a2-171 4.85E-05 2.78E-02 9.36E-04 1.35E-06 2.60E-15 422 52 1.60 1.79 0.00 0.21 0.848 -0.023 -0.030 2314 1047 a2-185 4.85E-05 6.79E-02 2.33E-03 3.29E-06 1.28E-14 449 37 1.79 1.70 0.01 0.29 0.837 0.010 -0.060 2563 650 a2-171 4.85E-05 6.62E-02 1.35E-03 3.21E-06 4.29E-15 545 58 1.46 1.74 0.00 0.26 0.848 -0.023 -0.033 2737 780 a2-171 4.85E-05 6.62E-02 1.35E-03 3.21E-06 4.29E-15 545 58 1.46 1.74 0.00 0.29 0.844 -0.010 -0.031 2457 472 a2-185 4.85E-05 3.05E-02 0.04E-04 1.48E-06 1.92E-15 511 55 1.74 1.81 0.01 0.18 0.848 -0.023 -0.041 2738 967 a2-185 4.85E-05 5.62E-02 1.14E-03 2.33E-06 6.10E-15 543 37 1.55 1.76 0.00 0.24 0.849 -0.023 -0.041 2738 967 a2-185 4.85E-05 5.72E-02 1.14E-03 2.73E-06 3.06E-15 431 37 1.55 1.76 0.00 0.24 0.849 -0.023 -0.041 2738 967 a2-185 4.85E-05 5.72E-02 1.14E-03 2.73E-06 3.06E-15 431 37 1.55 1.76 0.00 0.29 0.837 0.011 0.029 0.039 0.033 0.021 0.029 0.039 0.033 0.021 0.024 0.039 0.033 0.034 0.023 0.041 0.024 0.039 0.033 0.034 0.039 0.034 0.039 0.034 0.039 0.034 0.039 0.034 0.039 0.034 0.039 0.034 0.039 0.039 0.034 0.039 0.034 0.039 0.034 0.039 0.034 0.039 0.034 0.039 0.034 0.039 0.034 0.039																		a2-20
154 4,85E-05 7,23E-02 1,64E-03 3,51E-06 6,33E-15 353 30 1,71 1,93 0,00 0,07 0,856 -0,049 -0,053 2410 408 a2-162 4,85E-05 4,19E-02 1,35E-03 2,03E-06 4,29E-15 628 54 1,69 1,74 0,00 0,26 0,841 -0,003 -0,037 2514 865 a2-96 4,85E-05 3,14E-02 1,01E-03 1,52E-06 2,40E-15 501 54 1,53 1,88 0,00 0,11 0,852 -0,036 -0,034 2877 1152 a2-71 4,85E-05 2,78E-02 9,36E-04 1,35E-06 2,06E-15 422 52 1,60 1,79 0,00 0,21 0,848 -0,023 -0,003 2314 1047 a2-9 9,94E-04 1,48E-06 2,23E-15 545 58 1,46 1,74 0,00 0,26 0,848 -0,023 -0,003 2314 1047 a2-171 4,85E-05 6,62E-02 1,35E-03																		a2-21
162 4,85E-05 4,19E-02 1.35E-03 2,03E-06 4,29E-15 628 54 1.69 1.74 0.00 0.26 0.841 -0.003 -0.037 2514 865 a2-96 4.85E-05 3.14E-02 1.01E-03 1.52E-06 2.40E-15 501 54 1.53 1.88 0.00 0.11 0.848 -0.023 -0.034 2877 1152 a2-7 1 4.85E-05 2.78E-02 9.36E-04 1.35E-06 2.06E-15 422 52 1.60 1.79 0.00 0.21 0.848 -0.023 -0.030 2314 1047 a2-185 4.85E-05 6.79E-02 2.33E-03 3.29E-06 1.28E-14 449 37 1.79 1.70 0.01 0.29 0.837 0.010 -0.060 2563 650 a2-99 4.85E-05 6.66E-02 1.35E-03 3.21E-06 4.29E-15 545 58 1.46 1.71 0.00 0.29 0.844 -0.010 -0.031 2737 780 a2-198																		a2-22
96																		a2-23 a2-24
71																		a2-24 a2-25
185 4.85E-05 6.79E-02 2.33E-03 3.29E-06 1.28E-14 449 37 1.79 1.70 0.01 0.29 0.837 0.010 -0.09 0.837 0.010 -0.09 0.837 0.010 -0.09 0.838 -0.023 -0.033 2737 780 a2- 171 4.85E-05 6.62E-02 1.35E-03 3.21E-06 4.29E-15 545 58 1.64 1.71 0.00 0.29 0.844 -0.010 -0.033 2737 780 a2- 95 4.85E-05 3.05E-02 9.04E-04 1.48E-06 1.92E-15 511 55 1.74 1.81 0.01 0.18 0.848 -0.023 -0.041 2738 967 a2- 198 4.85E-05 5.47E-02 1.11E-03 2.30E-06 2.90E-15 676 52 1.73 1.65 0.01 0.35 0.847 -0.021 -0.019 2381 513 a2- 147 4.85E-05 8.72E-02 1.61E-03																		a2-25
99																		a2-20
171		4.85E-05																a2-28
95																2457		a2-29
198	95	4.85E-05	3.05E-02	9.04E-04			511	55	1.74	1.81	0.01	0.18	0.848	-0.023	-0.041	2738	967	a2-30
154 4.85E-05 8.72E-02 1.61E-03 4.23E-06 6.10E-15 294 25 1.41 1.60 0.00 0.39 0.833 0.021 -0.024 2688 700 a2-172 7.77E-05 3.55E-02 9.00E-04 2.76E-06 4.89E-15 496 41 1.75 1.82 0.00 0.18 0.846 -0.018 -0.012 2797 933 a2-1826 4.85E-05 5.11E-02 1.66E-03 2.48E-06 6.48E-15 407 39 1.75 1.70 0.00 0.30 0.841 -0.002 -0.041 2445 723 a2-183 4.85E-05 7.11E-02 2.08E-03 3.45E-06 1.02E-14 311 29 1.61 1.76 0.00 0.24 0.851 -0.033 -0.002 a2-147 4.85E-05 5.64E-02 1.31E-03 2.74E-06 4.04E-15 430 38 1.72 1.84 0.00 0.16 0.848 -0.024 -0.042 2466 742 a2-90 2.91E-05 7.48E-02 1.93E-03 2.18E-06 3.15E-15 333 37 1.67 1.72 0.00 0.27 0.846 -0.018 -0.006 2436 443 a2-180 4.85E-05 7.72E-02 1.68E-03 3.74E-06 6.64E-15 357 29 1.43 1.79 0.00 0.21 0.851 -0.032 -0.004 2647 630 a2-166 4.85E-05 7.72E-02 1.68E-03 3.74E-06 6.64E-15 357 29 1.43 1.79 0.00 0.21 0.851 -0.032 -0.004 2647 630 a2-166 4.85E-05 7.72E-02 1.68E-03 3.74E-06 6.64E-15 357 29 1.43 1.79 0.00 0.21 0.851 -0.032 -0.004 2647 630 a2-166 4.85E-05 7.72E-02 1.68E-03 3.74E-06 6.64E-15 357 29 1.43 1.79 0.00 0.21 0.851 -0.032 -0.004 2647 630 a2-166 4.85E-05 7.72E-02 1.68E-03 3.74E-06 6.64E-15 357 29 1.43 1.79 0.00 0.21 0.851 -0.032 -0.004 2647 630 a2-166 4.85E-05 7.72E-02 1.68E-03 3.74E-06 6.64E-15 357 29 1.43 1.79 0.00 0.21 0.851 -0.032 -0.004 2647 630 a2-166 4.85E-05 7.72E-02 1.68E-03 3.74E-06 6.64E-15 357 29 1.43 1.79 0.00 0.21 0.851 -0.032 -0.004 2647 630 a2-166 4.85E-05 7.72E-02 1.68E-03 3.74E-06 6.64E-15 357 29 1.43 1.79 0.00 0.21 0.851 -0.032 -0.004 2647 630 a2-166 4.85E-05 7.72E-02 1.68E-03 3.74E-06 6.64E-15 357 29 1.43 1.79 0.00 0.21 0.851 -0.032 -0.004 2647 630 a2-166 4.85E-05 7.72E-02 1.68E-03 3.74E-06 6.64E-15 357 29 1.43 1.79 0.00 0.21 0.851 -0.032 -0.004 2647 630 a2-166 4.85E-05 7.72E-02 1.68E-03 3.74E-06 6.64E-15 357 29 1.43 1.79 0.00 0.21 0.851 -0.032 -0.004 2647 630 a2-166 4.85E-05 7.72E-02 1.68E-03 3.74E-06 6.64E-15 357 29 1.43 1.79 0.00 0.21 0.851 -0.032 -0.004 2647 630 a2-166 4.85E-05 7.72E-02 1.68E-03 3.74E-06 6.64E-15 357 29 1.43 1.79 0.00 0.21 0.851 -0.032 -0.004 2647 630 a															-0.019			a2-31
$\begin{array}{cccccccccccccccccccccccccccccccccccc$																		a2-32
126 4.85E-05 5.11E-02 1.66E-03 2.48E-06 6.48E-15 407 39 1.75 1.70 0.00 0.30 0.841 -0.002 -0.041 2445 723 a2-133 4.85E-05 7.11E-02 2.08E-03 3.45E-06 1.02E-14 311 29 1.61 1.76 0.00 0.24 0.851 -0.033 -0.002 - - - a2-147 4.85E-05 5.64E-02 1.31E-03 2.74E-06 4.04E-15 430 38 1.72 1.84 0.00 0.16 0.848 -0.024 -0.042 2466 742 a2-9 2.91E-05 7.48E-02 1.93E-03 2.18E-06 3.15E-15 333 37 1.67 1.72 0.00 0.27 0.846 -0.04 2436 443 a2-9 208 4.85E-05 9.69E-02 2.85E-03 4.70E-06 1.91E-14 356 27 1.47 1.72 0.01 0.28 0.847 -0.019 -0.048 2517 592 a2-166																		a2-33
133 4.85E-05 7.11E-02 2.08E-03 3.45E-06 1.02E-14 311 29 1.61 1.76 0.00 0.24 0.851 -0.033 -0.002 - - - - - -2 -1 -4 -4 -4 -4 -4 -																		a2-34
147 4,85E-05 5,64E-02 1.31E-03 2.74E-06 4,04E-15 430 38 1.72 1.84 0.00 0.16 0.848 -0.024 -0.042 2466 742 a2- 90 2.91E-05 7.48E-02 1.93E-03 2.18E-05 3.5 37 1.67 1.72 0.00 0.27 0.846 -0.018 -0.006 2436 443 a2- 208 4.85E-05 9.69E-02 2.85E-03 4.70E-06 1.91E-14 356 27 1.47 1.72 0.01 0.28 0.847 -0.019 -0.048 2517 592 a2- 166 4.85E-05 7.72E-02 1.68E-03 3.74E-06 6.64E-15 357 29 1.43 1.79 0.00 0.21 0.851 -0.032 -0.004 2647 630 a2-																2445		a2-35
90 2.91E-05 7.48E-02 1.93E-03 2.18E-06 3.15E-15 333 37 1.67 1.72 0.00 0.27 0.846 -0.018 -0.006 2436 443 a2- 208 4.85E-05 9.69E-02 2.85E-03 4.70E-06 1.91E-14 356 27 1.47 1.72 0.01 0.28 0.847 -0.019 -0.048 2517 592 a2- 166 4.85E-05 7.72E-02 1.68E-03 3.74E-06 6.64E-15 357 29 1.43 1.79 0.00 0.21 0.851 -0.032 -0.004 2647 630 a2-																2/66		a2-36 a2-37
208 4.85E-05 9.69E-02 2.85E-03 4.70E-06 1.91E-14 356 27 1.47 1.72 0.01 0.28 0.847 -0.019 -0.048 2517 592 a2-166 4.85E-05 7.72E-02 1.68E-03 3.74E-06 6.64E-15 357 29 1.43 1.79 0.00 0.21 0.851 -0.032 -0.004 2647 630 a2-165 (2.10 -0.004) -0.004 2.004																		a2-37 a2-38
166 4.85E-05 7.72E-02 1.68E-03 3.74E-06 6.64E-15 357 29 1.43 1.79 0.00 0.21 0.851 -0.032 -0.004 2647 630 a2-																		a2-36
																		a2-40
1.71E-04 4.10E-12 4.53 12 1.80 1.73 0.00 0.24 0.840 -0.018 -0.020																		
	10142	3.44E-03			1.91E-04	4.10E-12	433	12	1.80	1./3	0.00	0.24	0.840	-0.018	-0.020			

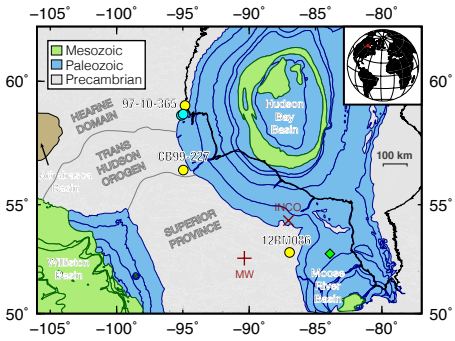
 N_s = spontaneous track count; P_i = down-pit weighted 238 U/ 43 Ca; Ω_i = track count area

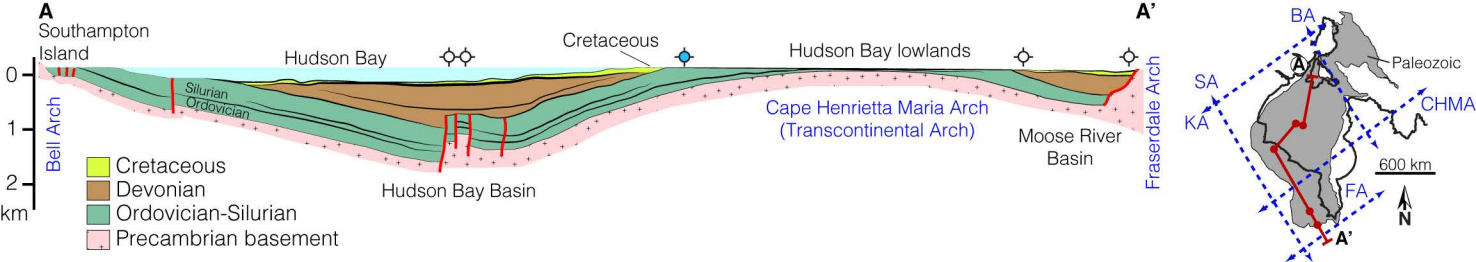
†AFT single-grain ages are calculated using the LA-ICP-MS (ζ -calibration) method with modified $\zeta=8.2727$, standard error (ζ) = 0.1407 and ^{2.38}U total decay constant of 1.55125 \times 10⁻¹⁰ yr⁻¹. Bottom table row displays the analysis sums, AFT central age \pm 1s error calculated in IsoplotR (Vermeesch, 2018), and the mean values for the tabulated elements/kinetic parameters.

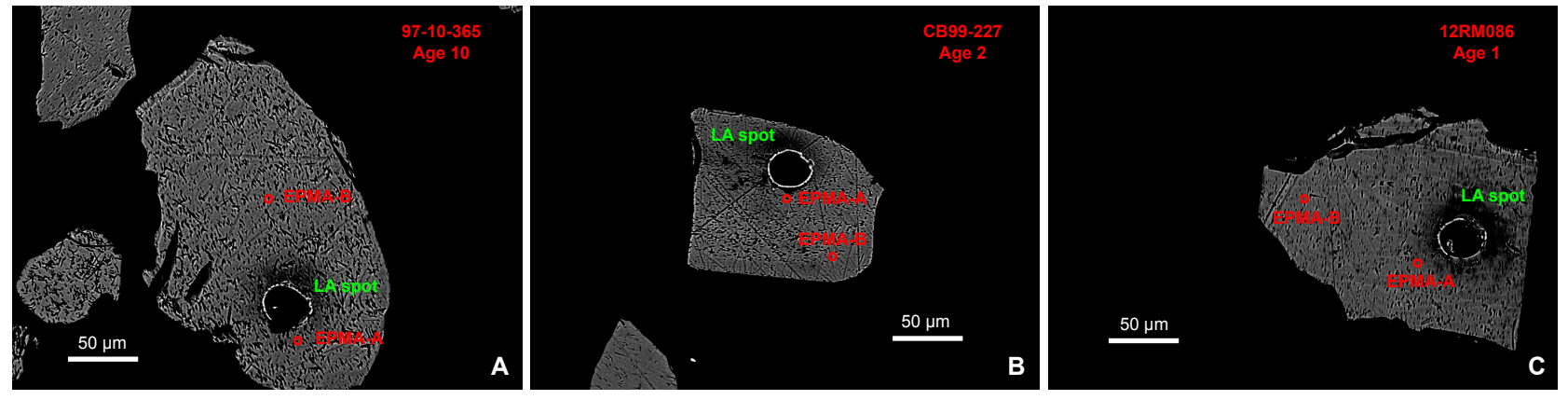
*Average values reported for F, Cl, OH, D_{par} , and effective Cl (eCl) in bottom row, median value shown for r_{mr0} ; Individual grain D_{par} values are the mean of 4 measurements. Aliquot-2 had two EPMA spots, one near the AFT laser ablation pit (A) and another elsewhere on the grain (B) to assess compositional heterogeneity. Elemental data for aliquot-2 (F, Cl, OH, r_{mr0}) are only reported in the table for spot A. Average wt % oxide total for aliquot-2 replicates is $99.2 \pm 1.2\%$; median = 99% (n = 80).

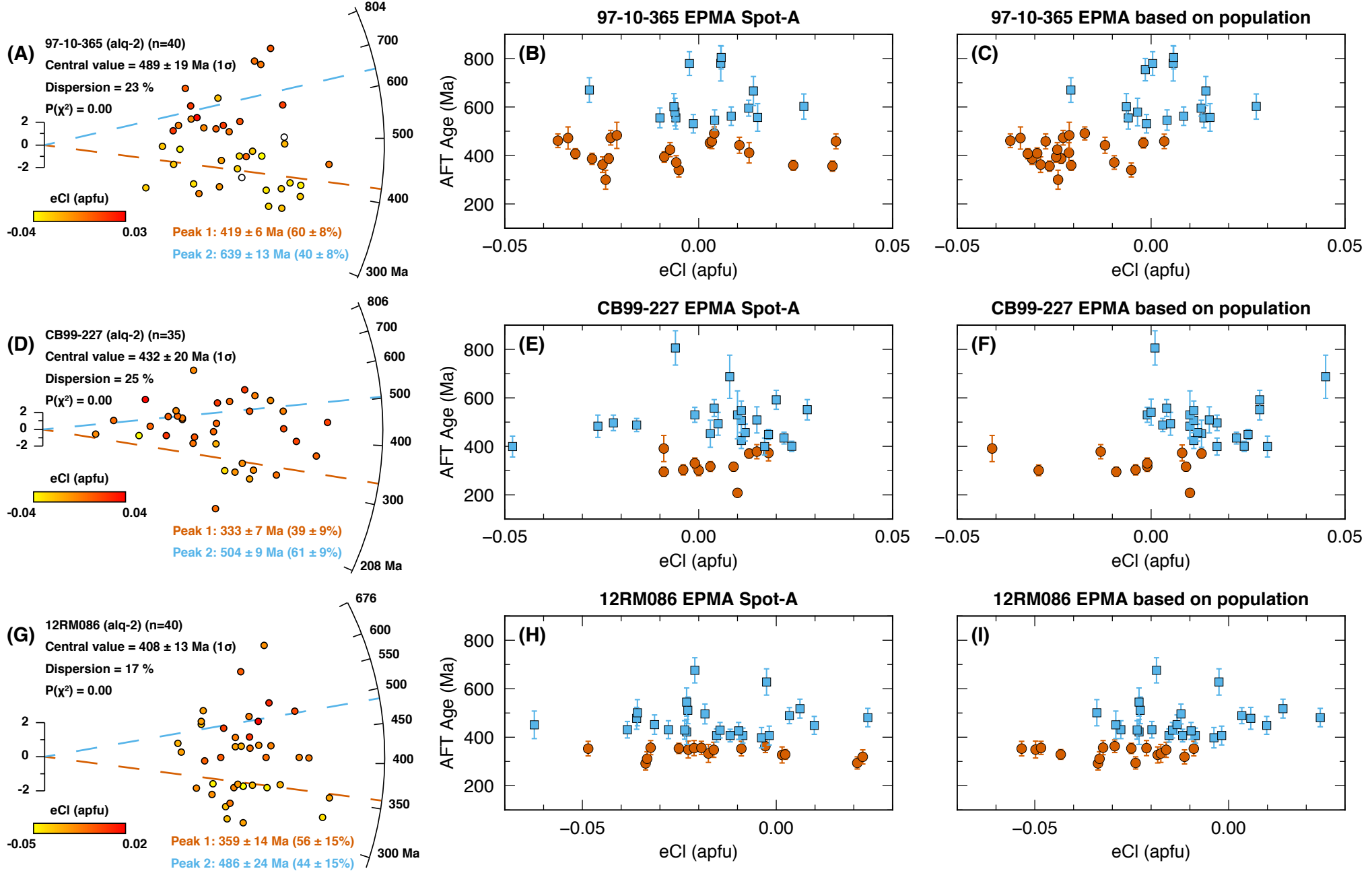
 \ddagger Individual isotopic sums U-Pb dates are common Pb-corrected using the Stacey & Kramers (1975) correction and 238 U/ 206 Pb and 207 Pb/ 206 Pb ratios.

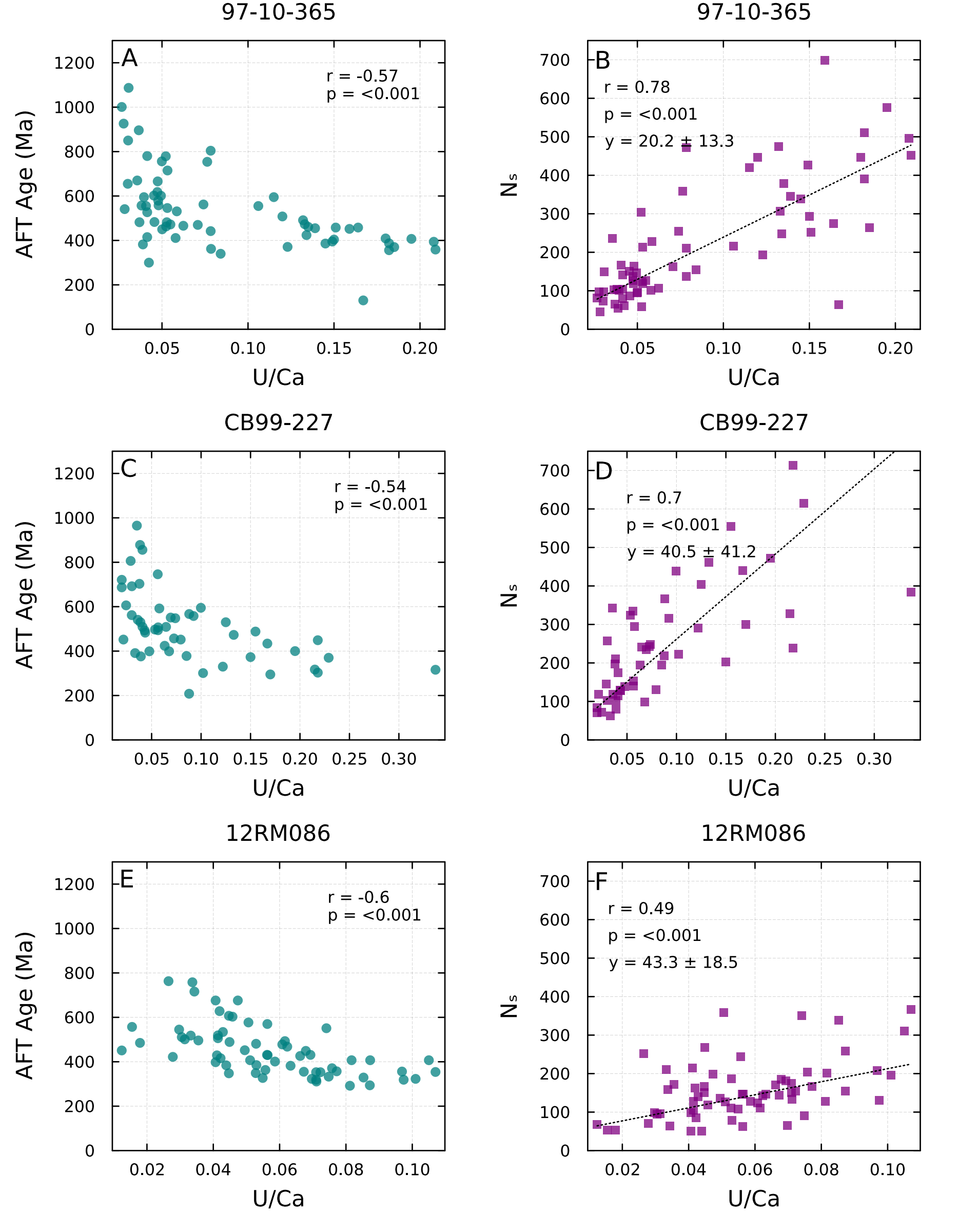


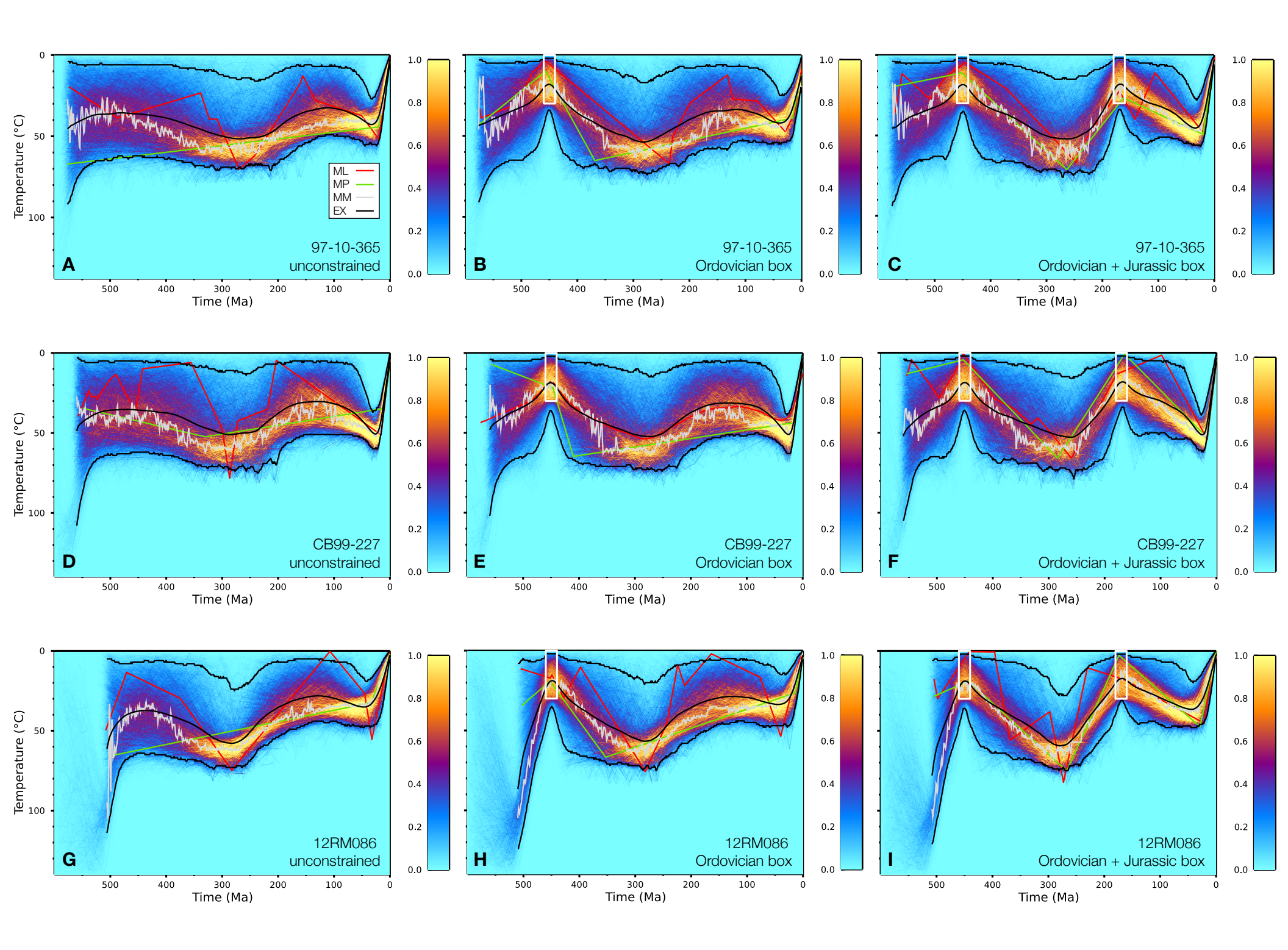


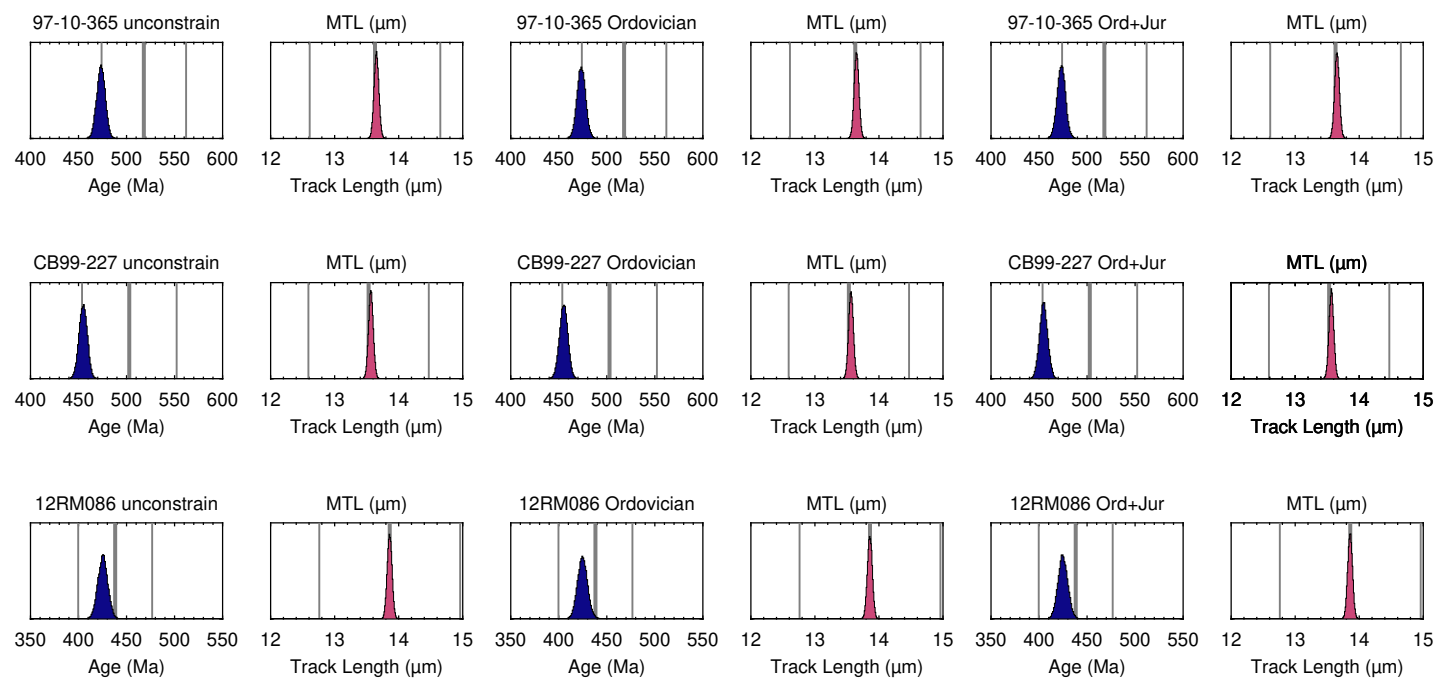


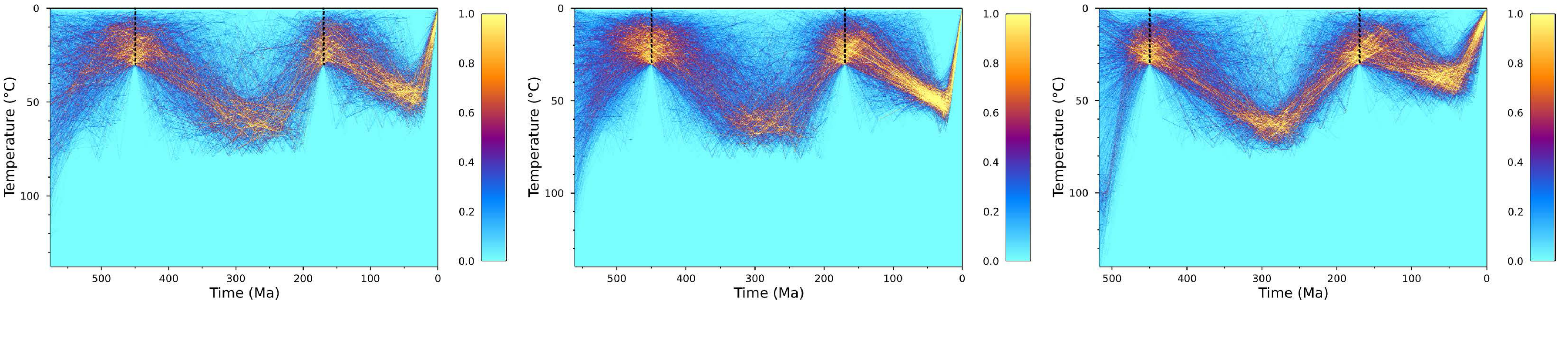




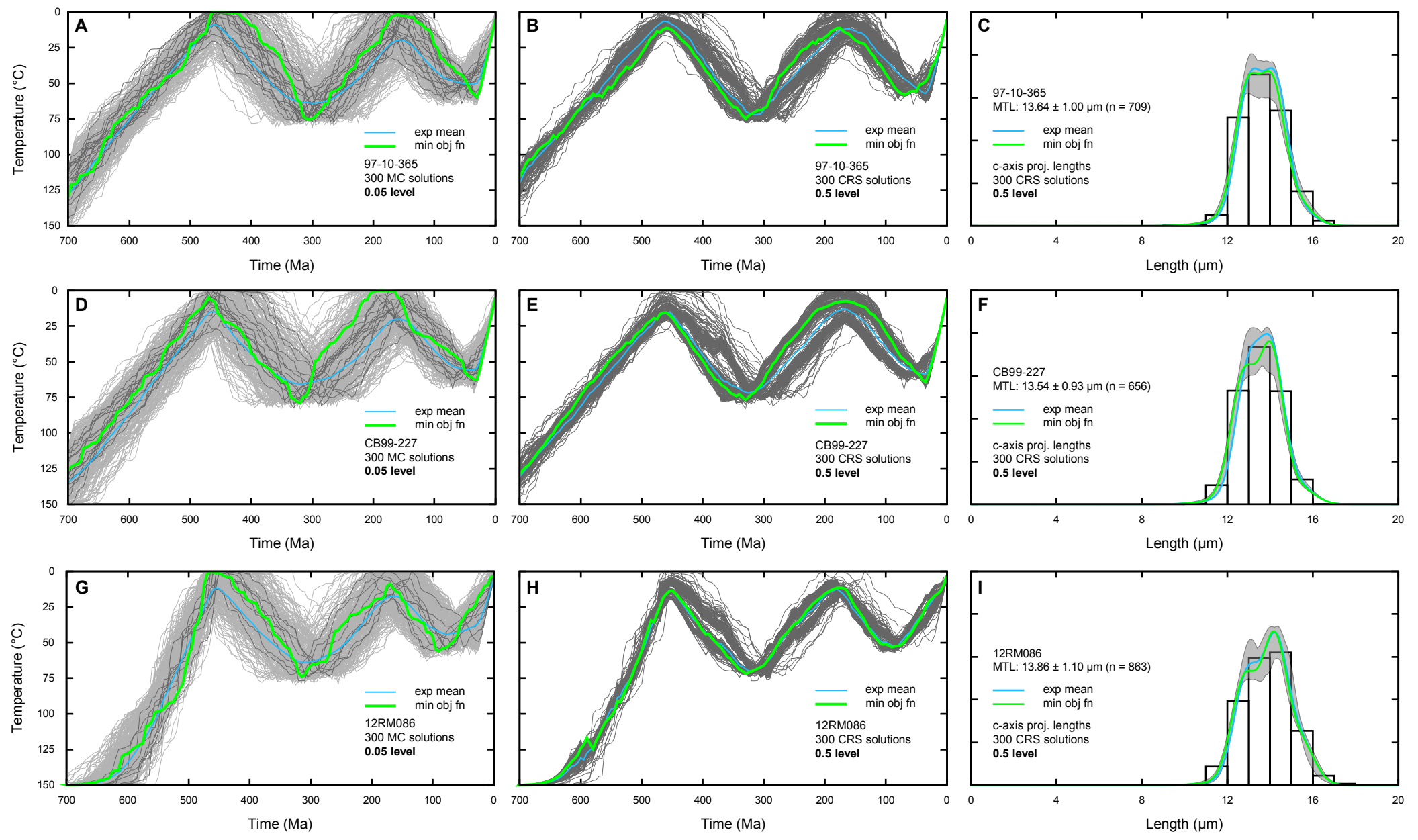


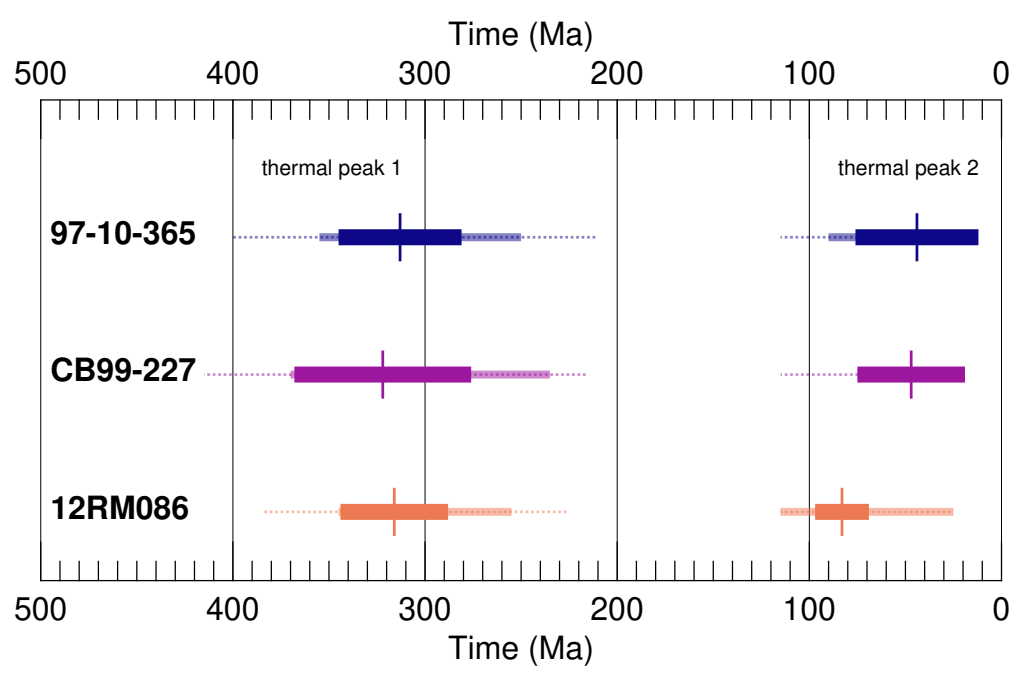


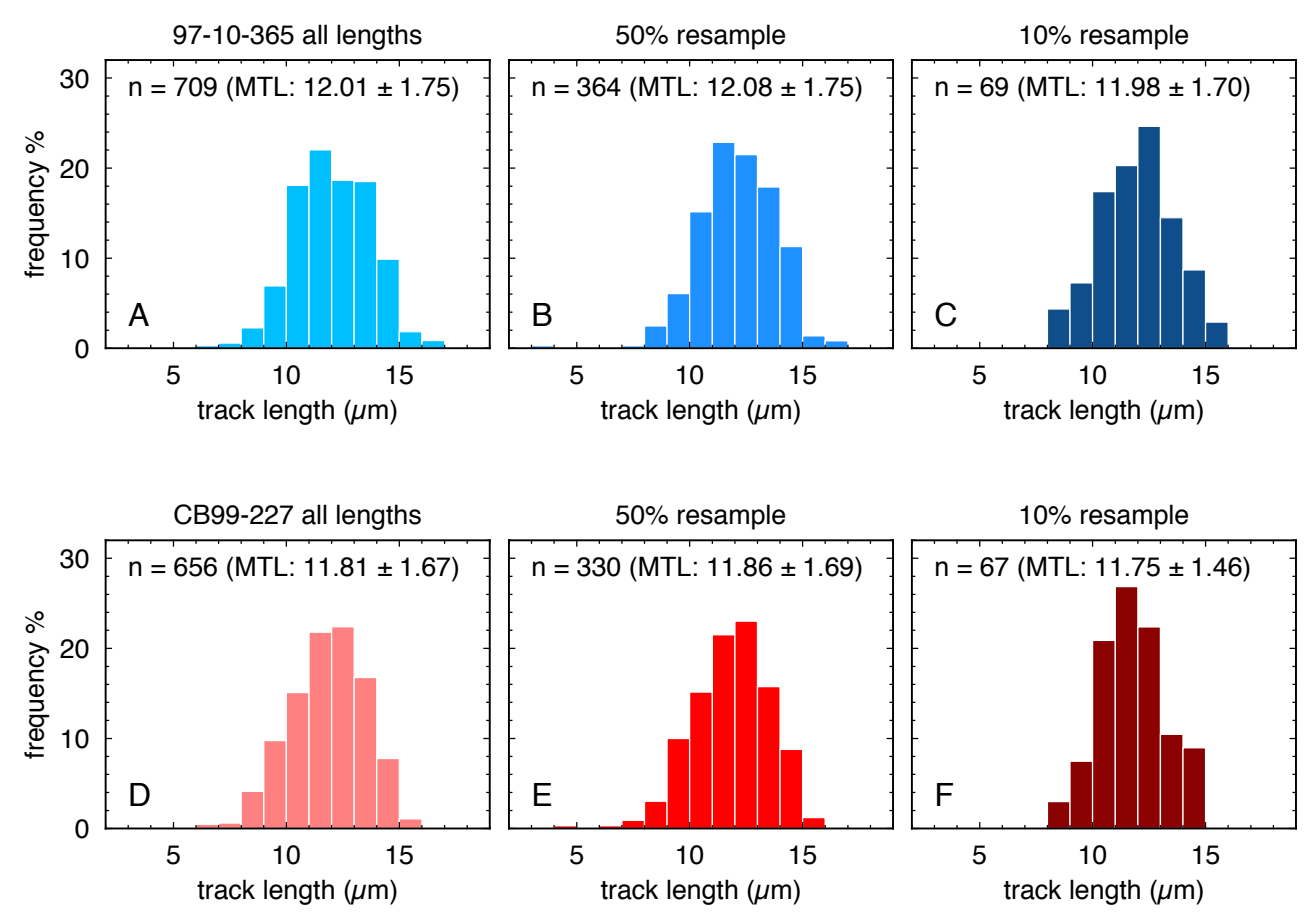




(a) sample 97-10-365 (b) sample CB99-227 (c) sample 12RM086







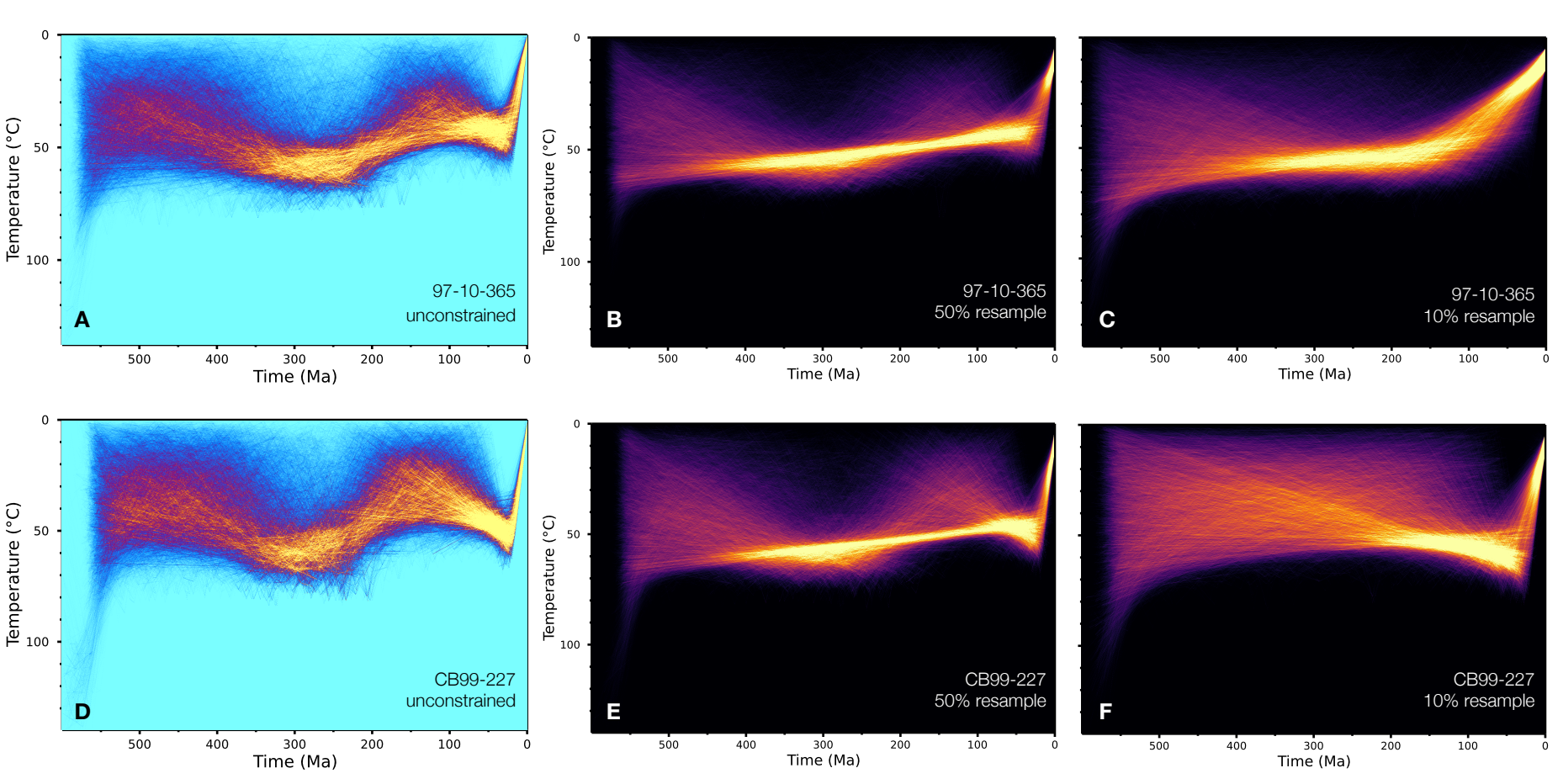


Table 1. Hudson Platform basement LA-ICP-MS AFT data summary

Sampl e	Lithol ogy	∑Ns	Age (Ma)	±1s	N	MSW D	Ρ(χ²)	Disp (%)	D _{par} (μm)	Cl (apfu)	r _{mr} o	eCl (apfu)	MTL	±1s	MTLc	±1s	N
97-10- 365	Grano diorite	14511	512	20	63/65	13	0.0	26	1.77	0.008	0.842	-0.007	12.01	1.75	13.64	1.02	709
CB99- 227	Tonali te	12444	486	23	50	19	0.0	30	1.83	0.003	0.838	0.001	11.81	1.67	13.54	0.93	656
12RM 086	Monz onite	10142	433	14	65	6	0.0	21	1.80	0.000	0.846	-0.021	12.4	1.8	13.86	1.1	863

 \sum Ns is the sample total spontaneous track count. Age is the LAFT central age from IsoplotR (Vermeesch, 2018). MSWD = Mean Square Weighted Deviation; Disp = dispersion. D_{par}, Cl, and eCl are mean values; r_{mr0} is the median value for the sample. MTL = mean track length; MTLc = c-axis projected.

Table 2. AFTINV v. 6.17 model results for single kinetic population Hudson Platform AFT samples

	97-10	D-365	CB99	9-227	12RM086			
	0.05 LEVEL	0.5 LEVEL	0.05 LEVEL	0.5 LEVEL	0.05 LEVEL	0.5 LEVEL		
search algorithm	MC	CRS	MC	CRS	MC	CRS		
model results	300 solutions	300 solutions	300 solutions	300 solutions	300 solutions	300 solutions		
	BEST MO	DEL FITS*	BEST MO	DEL FITS	BEST MODEL FITS			
AFT Age (± 2s)	512 ± 36 Ma	512 ± 36 Ma	487 ± 44 Ma	487 ± 44 Ma	433 ± 24 Ma	433 ± 24 Ma		
Model AFT Age	505.3 Ma	511.4 Ma	490.6 Ma	491.4 Ma	429.4 Ma	433.8 Ma		
Age GOF	0.70	0.96	0.85	0.82	0.75	0.97		
Length GOF	0.93	0.98	0.84	0.88	0.74	0.93		
Retention Age	653 Ma	673 Ma	648 Ma	650 Ma	538 Ma	545 Ma		
	THERMA	L PEAK 1	THERMA	L PEAK 1	THERMAL PEAK 1			
temp. minimum	69 °C	71 °C	72 °C	72 °C	68 °C	69 °C		
temp. maximum	81 °C	77 °C	83 °C	82 °C	80 °C	77 °C		
mean ± 1s	75 ± 2 °C	75 ± 1 °C	77 ± 2 °C	75 ± 1 °C	73 ± 2 °C	72 ± 1 °C		
time minimum	210 Ma	250 Ma	215 Ma	235 Ma	225 Ma	255 Ma		
time maximum	400 Ma	355 Ma	415 Ma	370 Ma	385 Ma	345 Ma		
mean ± 1s	298 ± 36 Ma	313 ± 16 Ma	308 ± 40 Ma	322 ± 23 Ma	302 ± 32 Ma	316 ± 14 Ma		
	THERMA	L PEAK 2	THERMA	L PEAK 2	THERMAL PEAK 2			
temp. minimum	51 °C	51 °C	52 °C	57 °C	43 °C	46 °C		
temp. maximum	66 °C	64 °C	72 °C	69 °C	63 °C	57 °C		
mean ± 1s	59 ± 3 °C	58 ± 2 °C	62 ± 2 °C	62 ± 2 °C	53 ± 3 °C	53 ± 2 °C		
time minimum	25 Ma	30 Ma	25 Ma	30 Ma	25 Ma	25 Ma		
time maximum	115 Ma	90 Ma	115 Ma	75 Ma	115 Ma	115 Ma		
mean ± 1s	55 ± 24 Ma	44 ± 16 Ma	52 ± 20 Ma	47 ± 14 Ma	66 ± 27 Ma	83 ± 7 Ma		
	BEST FIT PA	TH MINIMA**	BEST FIT PA	ATH MINIMA	BEST FIT PATH MINIMA			
min time 1	465 Ma	460 Ma	470 Ma	460 Ma	465 Ma	450 Ma		
min time 2	160 Ma	175 Ma	190 Ma	170 Ma	170 Ma	175 Ma		
	INFORM	MATION	INFORM	MATION	INFORMATION			
modeled rmr0	0.840 (0.0	apfu eCl)	0.837 (0.0	1 apfu eCl)	0.848 (-0.025 apfu eCI)			
min. obj. sol.	lowest comb	oined obj. fn.	lowest ma	ax. obj. fn.	lowest combined obj. fn.			
c-axis MTL	13.64 ±	1.00 µm	13.54 ±	0.93 µm	13.86 ± 1.10 μm			
lengths (n)	70)9	65	56	863			

^{*}Model fits are shown only for the minimum objective function solution. Information about the thermal peaks is for all 300 solutions at the corresponding significance level. Retention age is the hypothetical oldest preserved fission track and approximates the upper limit of t-T sensitivity.

**Minima were randomly selected between 470 Ma and 450 Ma (followed by thermal peak 1) and 200 Ma and 120 Ma (followed by thermal peak 2).